Remote Sensing of Tropical Cyclones: Applications from Microwave Radiometry and Global Navigation Satellite System Reflectometry

by

Mary Morris

A dissertation submitted in partial fulfillment
of the requirements for the degree of
Doctor of Philosophy
(Atmospheric, Oceanic and Space Sciences)
in the University of Michigan
2017

Doctoral Committee:

Professor Christopher S. Ruf, Chair
Associate Professor Mark G. Flanner
Professor Brian E. Gilchrist
Associate Research Scientist Darren S. McKague
Dr. Derek J. Posselt, NASA JPL, California Institute of Technology

© Mary Morris

All Rights Reserved

2017

Acknowledgements

I am indebted to …

my research advisor, Prof. Ruf for his patience, empathy, and generosity;

my committee members, Drs. Flanner, Gilchrist, McKague, and Posselt, for their advice and support;

Prof. Judge, for her encouragement and mentorship during my first research internship;

my colleagues that have supported my HIRAD research projects, most notably, Drs. Biswas and Cecil, as well as the HIRAD instrument team members that came before me, developing the initial HIRAD instrument, models, and algorithms which made HIRAD possible;

my colleagues that have supported my CYGNSS research projects, most notably, Drs. Baker, Clarizia, O'Brien, Ridley, Said, and Soisuvarn, as well as the entire CYGNSS science team for their encouragement;

the staff of the Climate and Space Sciences and Engineering Department at the University of Michigan who always make my life easier;

my friends for their kindness and encouragement;

my parents and family for their generosity and love;

my sisters, Jill and Patrice, for their love and loyalty;

and Martin, for everything.

Table of Contents

Acknowledgements ii

Table of Contents iii

List of Tables vii

List of Figures ix

Abstract xviii

Chapter 1. Introduction 1

1.1 Introduction to Tropical Cyclones 1

1.2 Remote Sensing of Oceanic Surface Wind Speed 9

1.2.1 Spaceborne Passive Microwave vs. Conventional Radar 9

1.2.2 Monostatic Radar vs. Bistatic Radar 17

1.2.3 Observations from Shorter vs. Longer Wavelengths 18

1.3 Sensitivity of Remote Sensing to Precipitation 19

1.4 Remote Sensing of Tropical Cyclones 25

1.4.1 Importance of Tropical Cyclone Remote Sensing 25

1.4.2 Remote Sensing Applications to Tropical Cyclone Intensity and Wind Structure Estimation 26

1.5 Organization of thesis 28

Chapter 2. A Coupled-Pixel Model (CPM) Atmospheric Retrieval Algorithm for the Hurricane Imaging Radiometer (HIRAD) 30

2.1 Summary 30

2.2 Introduction 31

2.3 Decoupled and Coupled Forward Radiative Transfer Models 35

2.4 Simulated Observations as Test Cases 39
2.5 Inversion Algorithm 43
2.5.1 Procedure 43
2.5.2 Regularization Issues 44
2.6 Results 47
2.6.1 Algorithm Performance for Simulated Test Cases 47
2.6.2 Algorithm Performance for High Variability Wind Speed Scenes 50
2.6.3 Hurricane Earl (2010) HIRAD Rain Rate Retrievals 51
2.7 Discussion 53
2.7.1 Weighted Antenna Beam Issues 53
2.7.2 Comparison of Coupled and Decoupled Performance 54
2.7.3 Other Applications 56
2.8 Conclusions 56
Appendix 2.I: Derivation of Inter-Pixel Coupling Weights in the CPM 57
Chapter 3. Estimating Tropical Cyclone Integrated Kinetic Energy with the CYGNSS Satellite Constellation 62
3.1 Summary 62
3.2 Introduction 62
3.2.1 Tropical Cyclone Intensity Classifications and Complications 62
3.2.2 Previous IKE studies 64
3.2.3 Existing Sensors for Surface Wind Speed Estimation 65
3.2.4 CYGNSS 65
3.2.5 Objectives and Overview 66
3.3 Datasets 67
3.4 Methodology 69

3.5 Results 73
3.5.1 CYGNSS-IKE Performance 73
3.5.2 Quality Control Threshold Determination 76
3.5.3 Error Decomposition 79
3.5.4 Storm Center Sensitivity 80
3.6 Discussion 82
3.7 Conclusions 85
Chapter 4. Determining Tropical Cyclone Surface Wind Speed Structure and Intensity with the CYGNSS Satellite Constellation 86
4.1 Summary 86
4.2. Introduction 86
4.2.1 Motivation 86
4.2.2 Examples of Previous Efforts 87
4.2.3 CYGNSS 89
4.2.4 Outline 90
4.3 Datasets 91
4.4 Methodology 92
4.4.1 Parametric Wind Model 92
4.4.2 Parametric Retrieval Algorithm 94
4.4.3 Three- versus Two-parameter Model Impacts 97
4.4.4 Parametric Scaling 97
4.5 Initial Results 100
4.5.1 Performance without Quality Control 100
4.5.2 Sensitivity to Storm Center Location Error 102
4.5.3 Sensitivity to CYGNSS Coverage 105

4.5.4 Quality Control Test Procedures 108
4.6 Final Results 109
4.7 Discussion 111
4.8 Conclusions 114
Appendix 4.I 115
Chapter 5. Summary and Future Work 117
5.1 Summary of Original Contributions 117
5.1.1 Brief Review of Thesis 117
5.1.2 Original Work 118
5.2 Future Work 119
5.2.1 General Applicability of the Parametric Wind Model Algorithm 119
5.2.2 Science Applications from CYGNSS L4 Products 121
5.2.3 Orbit Configuration Optimization for CYGNSS TC Product Performance 122
References 123

List of Tables

Table 2.1: Summary of simulated test case identification numbers, and descriptions of the true surface wind speed (m s^{-1}) and rain rate (mm h^{-1}) for each case. The parameters of WS, RR, X_{RRi1}, X_{RRi2}, and X_{PEAK} are labeled in Figure 2.4 for a visualization of the types of cases simulated. X_{RRi1} is the horizontal distance to the point in the cross-track swath where the first (or only) rain band begins, from 0° EIA. X_{RRi2} is the distance to the point in the cross-track swath, from 0° EIA, where the second rain band begins (double rain band cases only). X_{PEAK} is the distance to the point in the cross-track swath, from 0° EIA, where wind speed and the outer rain band peaks. The identification numbers provide information about the particular test case. In the constant cases, the number before the 'w' gives the true wind speed and the number before the 'r' gives the true rain rate. In the rain band cases, the number before the letter 's' or 'd' gives the EIA location of X_{PEAK}..... 41

Table 2.2: RMS difference (RMSD) between the true and CPM-retrieved parameters (averaged over the swath) for each test case simulation. Noise-free performance is listed under the 0 K noise columns. Noisy simulations were also tested with 25 realizations of observations with random Gaussian noise with standard deviation of 1 K added. The RMSD for 1 K noise cases is an average value from the 25 realizations..... 48

Table 2.I.1: The number of rain pixels that are considered when calculating the effective rain rate in the field of view at Earth incidence angles (EIA) of the subset of observations used in the simulated test case set up. 61

Table 3.1: A summary of all of the storms used in this study, with the storm name, the number of cases for that particular storm, the maximum wind speed (V_{MAX}) of the cases considered, the storm center latitude and longitude of the storm at the point in time corresponding to the V_{MAX} case, and the year for each storm. 69

Table 3.2: Percent unexplained variance for experiments which used different input wind fields into the CYGNSS-IKE algorithm, where percent unexplained variance is $(1 - R^2) \times 100\%$. 80

Table 4.1: Coefficients used for translation from the parametric metrics to the scaled-parametric metrics, assuming the form of eqn.3. 100

Table 4.2: Mean and standard deviation of the error plotted in Figure 4.5 for each parametric and scaled-parametric metric. 101

Table 4.3: Mean and standard deviation of the error plotted in Figure 4.10 for each parametric and scaled-parametric metric, as well as the quality controlled scaled-parametric metrics. 109

Table 4.I.1: A summary of all of the storms used in this study, with the storm name, the number of cases for that particular storm, the maximum wind speed (V_{MAX}), the storm center latitude and longitude at the point in time corresponding to the V_{MAX} case, and the year for each storm. 115

List of Figures

Figure 1.1: Cause of death in the United States directly attributable to Atlantic tropical cyclones, 1963-2012. Credit: (Rappaport 2014) 2

Figure 1.2: Global distribution of observed tropical cyclone tracks from 1851-2006 (where available) and the corresponding intensity according to the Saffir-Simpson Hurricane Intensity Scale. Credit: The COMET Program..... 3

Figure 1.3: A mosaic of visible and infrared imagery over the lifecycle of Hurricane Earl (2012), with strength and track denoted for additional clarity. Courtesy of Cooperative Institute for Meteorological Satellite Studies/University of Wisconsin-Madison Tropical Cyclones Atlantic Storm Product Archive..... 6

Figure 1.4: Conceptual model of the main structural elements of tropical cyclones: boundary layer inflow, clear central eye, eyewall and rain bands surrounding the eye, cirrus cloud shield and the upper tropospheric outflow. Credit: (Lang and Evans, 2016)..... 7

Figure 1.5: L-band model azimuth patterns for TB for v-polarization (TB^{v}) and horizontal polarization (TB^{h}) from (Yueh and Chaubell, 2012). Figure adopted from Ulaby et al. (2014). 11

Figure 1.6: The backscattering coefficient versus wind –speed and azimuth angle at 13.9 GHz and 40 degree incidence angle. Note that the upwind backscatter is always larger than downwind and cross wind and that the backscattering

coefficient always rises with wind speed. Measured data is from Schroeder et al. (1985). Figure from Ulaby and Long (2014) 14

Figure 1.7: The Ku-band Seasat scatterometer (SASS-1) SASS-1 model (Schroeder et al., 1982) geophysical model function relating ocean surface σ^0 to the near-surface wind speed: σ^0 versus incidence angle for when the wind is blowing toward the radar (downwind). Adopted from Ulaby et al. (2014). 15

Figure 1.8: Calculated Mie extinction (κ_e) and absorption (κ_a) coefficients of rain characterized by a precipitation rate of 12 mm h^{-1}. [from Ulaby and Long, 2014; Tsang et al., 1977]..... 24

Figure 2.1: Typical observing geometry of: (a) a spaceborne microwave radiometer; and (b) the airborne stepped frequency microwave radiometer (SFMR) (not to scale). FL stands for freezing level, SFC stands for Earth surface. The yellow shaded region on the left represents the relatively small portion of the rain column below the freezing level that is not common to both the upwelling and downwelling emission sensed by the radiometer. The horizontal extent of individual pixels in the image is indicated by black vertical tick marks..... 31

Figure 2.2: Diagram showing the assumptions made about the below-freezing-level atmosphere in a decoupled-pixel (DPM) (a) vs. coupled-pixel (CPM) (b) forward model. The horizontal extent of individual pixels in the image is indicated by black vertical tick marks. Regions 1 and 5 are modeled as a gaseous atmosphere without rain. Region 2 is the downwelling-only portion of the observing path for a particular field of view. Region 3 is the overlapping area of upwelling and downwelling portions of the path. Region 4 is the upwelling only portion of the path. (a): In the DPM model, regions 2-4 are modeled assuming the upwelling and downwelling paths have the same rain. (b): In the CPM model,

there is no longer an assumption that the same rain is seen along the upwelling and downwelling paths. While there is a small portion of overlap in the paths (region 3), regions 2 and 4 are not assumed to have the same rain as region 3.36

Figure 2.3: The relationship between HIRAD's beamwidth and synthetic antenna pattern with earth incidence angle (EIA). Portions of synthetic antenna beam patterns are shown in grayscale for EIA of 7°, 36°, and 62°, and are labeled in the figure. Plotted in blue is the half power beam width (HPBW). HPBW is the angle between points in the antenna pattern where the power is half of the maximum. 38

Figure 2.4 Portrayals of the true surface wind speed (m s^{-1}) and rain rate (mm h^{-1}) used to simulate observations for each case type. The X parameters are labeled on the x axis to provide reference to Table 2.1 and are quantified in Table 2.1 for each test case ID number. X_{RRi1} is the horizontal distance to the point in the cross-track swath where the first (or only) rain band begins, from 0 ° EIA. X_{RRi2} is the distance to the point in the cross-track swath, from 0 ° EIA, where the second rain band begins (double rain band cases only). X_{PEAK} is the distance to the point in the cross-track swath, from 0 ° EIA, where wind speed and the outer rain band peaks. 40

Figure 2.5: The relationship between the amount of regularization and the corresponding errors in the retrieved surface wind speed (top) and rain rate (bottom). The amount of error for each regularization amount represents an average across all simulated cases. For simulated cases with rain bands, errors were focused and averaged +/- 5° earth incidence angle around the rain bands. Errors in 1 K noise cases were averaged over 25 realizations of each simulated case for a representative idea of how random noise affects the retrieval performance at different levels of regularization. 45

Figure 2.6: Comparison of noise free retrieval performance for simulated case 40s (left) and 40d (right) over a range of values. EIA is the Earth incidence angle. A γ value of 10^{-1} was chosen as a compromise value between a solution that is highly noise sensitive and a solution that cannot differentiate between two neighboring rain bands. 46

Figure 2.7: Correlation between retrieval of rain rate and surface wind speed at one cross-track position with that at all other cross-track positions, composited over all simulated cases with 1 K noise. EIA is Earth incidence angle. 49

Figure 2.8: An example of wind speed (top) and rain rate (bottom) CPM retrieval performance as compared to the simulation truth for a complicated and unusual double wind speed maxima and rain band scene. 51

Figure 2.9: HIRAD observations of Hurricane Earl (2010) during GRIP (color) and the closest 85h satellite imagery (grayscale) from SSM/I. The satellite imagery is shown alone in Fig.2.9.a. HIRAD observations are expressed as excess TB (K), which is (HIRAD observed TB – background TB), leaving only the relationships in TB due to strong winds and rain. Figure 2.9.b shows the approximate flight track of SFMR in addition to the excess TB at 4 GHz. Figure 2.9.c shows excess TB for 5 GHz. Figure 2.9.d shows excess TB for 6.6 GHz. The satellite imagery is courtesy of the Naval Research Laboratory. 52

Figure 2.10: (a) 85h satellite imagery from SSM/I. This satellite imagery is courtesy of the Naval Research Laboratory. (b) A composite of HIRAD CPM rain rate retrievals (mm h^{-1}) of Hurricane Earl (2010) (color) and the closest 85h satellite imagery (grayscale) from SSM/I. The dashed arrow shows the approximate flight track of SFMR. 53

Figure 2.11: Wind speed (top) and rain rate (bottom) CPM retrieval performance as compared to the simulation truth and beam averaged truth for Case 30d. 54

Figure 2.12: (a): SFMR and HIRAD/CPM retrieved rain rate, plotted along the latitude and longitude coordinates for reference. Flying on different aircraft, SFMR and HIRAD observations differ in time by ~15 minutes. (b): Plotted only with respect to longitude, a comparison of HIRAD rain rate retrievals (using the decoupled and coupled-pixel algorithms), as compared to nearly co-located SMFR observations of Hurricane Earl (2010). 55

Figure 2.A1: This diagram shows a simple example, where three atmospheric columns contribute towards a single field of view, each having potentially different rain amounts, designated by the red, blue, and yellow values. The upwelling propagation path, signified by the green line, intersects through the blue and yellow columns of atmosphere. The downwelling propagation path, signified by the purple line, intersects through the red and blue columns of atmosphere. FL stands for freezing level. SFC stands for the ocean surface.....58

Figure 2.A2: This figure illustrates that the weighted upwelling rain rate would be a weight of the blue and yellow columns of atmosphere. $A_{Y_{UP}}$ and $A_{B_{UP}}$ are labeled for reference to eqn.2.A1.....59

Figure 2.A3: This figure illustrates that the weighted downwelling rain rate would be a weight of the blue and red columns of atmosphere. $A_{R_{DN}}$ and $A_{B_{DN}}$ are labeled for reference to eqn.2.A2.....60

Figure 3.1: (Top) An example of an HWRF wind analysis for Hurricane Igor, 1200 UTC, 13 September 2010. (Bottom) Simulated CYGNSS observations that

correspond to the HWRF wind analysis, within 200 km of the storm center, for the time period 1200 UTC – 1500 UTC, 13 September 2010. 68

Figure 3.2: A visualization of the parametric wind profile embedded within the CYGNSS-IKE algorithm. This model is described by eqn. (3.2), based on the work of Emanuel (2011) and recommended by Lin and Chavas (2012). 71

Figure 3.3: A flow chart describing the steps within the CYGNSS-IKE algorithm. 72

Figure 3.4: An example of the cost function to be minimized, RMSD, is shown as a function of the parametric model free-variables, $R_{m.p}$ and $V_{m.p}$ from eqn. .. (3.2), for Test Case: Hurricane Igor, 1200 UTC, 13 September 2010. For further reference and connection, Figure 3.1 shows the HWRF wind field and corresponding CYGNSS observations that were input into the CYGNSS-IKE estimation process for this test case. 72

Figure 3.5: A comparison of the IKE estimated from HWRF wind fields (truth) and simulated CYGNSS observations (retrieved) over the life cycle of Hurricane Igor (2010) as a function of the elapsed time since tropical depression formation at 0600 UTC 8 September 2010 (Pasch and Kimberlain 2011). For further reference and connection, Figure 3.1 shows the HWRF wind field and corresponding CYGNSS observations that were initially input into the CYGNSS-IKE estimation process at elapsed time 126 hours. 75

Figure 3.6: A comparison of CYGNSS-IKE with the IKE estimated from HWRF for test cases defined from a set of simulated CYGNSS observations of Atlantic and Pacific-basin storms occurring during 2010 – 2011. Out of 201 storm test cases,

IKE is estimated for a particular quadrant 412 times. Red dots denote cases where Q/C is flagged. 76

Figure 3.7: Top: IKE RMS normalized difference between HWRF-IKE and CYGNSS-IKE with respect to two Q/C flags operated in combination. Each line represents the minimum number of observations allowed for a test case. Each line is plotted against a second Q/C flag, which controls for the ratio of the number of observations per the 34-kt wind radius in the parametric model ($R_{34.P}$). Bottom: Fraction of data left for all combinations of Q/C applied. The Q/C choice of more than 10 samples and more than 0.1 samples/km leaves 88% of the test cases. 77

Figure 3.8: The average relative difference in CYGNSS and HWRF derived IKE estimates for experiments where the given storm center location was perturbed degrees north and south of its original location, shown along the x-axis. 81

Figure 3.9: The relative, quadrant specific, IKE error of cases post-QC, with respect to the maximum wind speed found in the HWRF wind field. Quadrant Normalized IKE Error = (truth – estimated)/truth where the truth here is derived from HWRF..... 84

Figure 3.10: The relative IKE error of cases post-QC, with respect to the maximum wind speed found in the HWRF wind field. Normalized IKE Error = (truth – estimated)/truth where the truth here is derived from HWRF. IKE is summed over all quadrants for cases where there were estimates of IKE for all quadrants available. 84

Figure 4.1: An example of the wind speed relationship from the parametric model in eqn.(4.2) with three different 'b' parameters used. $V_{m.p}$ = 50 m s^{-1}. $R_{m.p}$ = 75 km, and the center position latitude is 15°. 94

Figure 4.2: A flow diagram which outlines the steps of the CYGNSS tropical cyclone surface wind speed structure and intensity product algorithms. 95

Figure 4.3: (a) HWRF wind speed field for Vongfong on 09 October 2014, 03:00 UTC; (b) Simulated CYGNSS wind speed observations for (a); and (c) the parametric model algorithm fit for this test case. 96

Figure 4.4: (a) HWRF wind speed field for Soulik on 11 July 2013, 03:00 UTC; (b) Simulated CYGNSS wind speed observations for (a) with the NE quadrant (cornered off by red lines) currently being considered; and (c) the parametric model algorithm fit for this NE quadrant test case, from which the NE quadrant wind radii are solved for..... 99

Figure 4.5: Histograms of error before quality control is applied in all parametric and scaled-parametric metrics. Error is defined here as true – estimated. 102

Figure 4.6: The additional error on average to expect from storm center offsets (here, only in latitude) for (a) V_{MAX} and (b) R_{MAX}. 104

Figure 4.7: The additional error on average to expect from storm center offsets (here, only in latitude) for wind radii. This analysis is based on the cases available in the NE quadrant..... 105

Figure 4.8: (a) The RMSD between the HWRF and CYGNSS derived V_{MAX} depending on the quality control filter threshold used. The quality control keeps test cases that have a number of observations within 100-km from the storm center above the sample number threshold plotted on the x-axis. (b) The same as (a), but for R_{MAX}. (c) The fraction of the original test case estimates left that are used to derive the RMSD in (a) and (b). 106

Figure 4.9: (a) The RMSD between the HWRF and CYGNSS derived wind radii depending on the quality control applied. The quality control keeps test cases that have a number of observations outside 100-km from the storm center (but within the estimate of R_{34}) above the sample number threshold plotted on the x-axis. (b) The fraction of the original test case estimates left that are used to derive the RMSD in (a). 107

Figure 4.10: Histograms of error in all parametric, scaled-parametric, and quality controlled scaled-parametric metrics. Error is defined here as true – estimated. 110

Figure 4.11: Histograms of the quality controlled scaled-parametric V_{MAX} and R_{MAX} depending on the HWRF V_{MAX} threshold attained. Weaker storms (V_{MAX} < 33 m s^{-1}) are plotted in solid light blue. Stronger storms (V_{MAX} >= 33 m s^{-1}) are plotted in dashed dark red. 112

Figure 4.12: Histograms of the quality controlled scaled-parametric metrics depending on the test case basin. Storms from the Atlantic and East Pacific basins are plotted in solid light green. Storms from the Western Pacific basin are plotted in dashed dark blue. 113

Abstract

Tropical cyclones (TCs) are important to observe, especially over the course of their lifetimes, most of which is spent over the ocean. Very few in situ observations are available. Remote sensing has afforded researchers and forecasters the ability to observe and understand TCs better. Every remote sensing platform used to observe TCs has benefits and disadvantages. Some remote sensing instruments are more sensitive to clouds, precipitation, and other atmospheric constituents. Some remote sensing instruments are insensitive to the atmosphere, which allows for unobstructed observations of the ocean surface. Observations of the ocean surface, either of surface roughness or emission can be used to estimate ocean surface wind speed. Estimates of surface wind speed can help determine the intensity, structure, and destructive potential of TCs. While there are many methods by which TCs are observed, this thesis focuses on two main types of remote sensing techniques: passive microwave radiometry and Global Navigation Satellite System reflectometry (GNSS-R).

First, we develop and apply a rain rate and ocean surface wind speed retrieval algorithm for the Hurricane Imaging Radiometer (HIRAD). HIRAD, an airborne passive microwave radiometer, operates at C-band frequencies, and is sensitive to rain absorption and emission, as well as ocean surface emission. Motivated by the unique observing geometry and high gradient rain scenes that HIRAD typically observes, a more robust rain rate and wind speed retrieval algorithm is developed. HIRAD's observing geometry must be accounted for in the forward model and retrieval algorithm, if high rain gradients are to be estimated from HIRAD's observations, with the ultimate goal of improving surface wind speed estimation.

Lastly, TC science data products are developed for the Cyclone Global Navigation Satellite System (CYGNSS). The CYGNSS constellation employs GNSS-R techniques to estimate ocean surface wind speed in all precipitating conditions. From inputs of CYGNSS level-2 wind speed observations and the storm center location, a variety of products are created: integrated kinetic energy, wind radii, radius of maximum wind speed, and maximum wind speed. These products provide wind structure and intensity information—valuable for situational awareness and science applications.

Chapter 1. Introduction

1.1 Introduction to Tropical Cyclones

Tropical cyclones (TCs) are strong low-pressure systems that form in the tropics. TCs are similar to their mid-latitude counterparts in that they are low-pressure systems, and dissimilar in that they are warm-core systems without fronts. Tropical cyclone is the general term used throughout the world, but other terms are used to refer to TCs developing in specific ocean basins. In the Eastern Pacific and Atlantic Ocean basins, TCs are referred to as hurricanes. In the western Pacific, the term typhoon is used. For TCs forming near Australia and in the Indian Ocean basin, the term cyclone is used.

Regardless of the term used to describe this type of storm, the destructive nature of TCs motivates their study. Extreme winds and precipitation are just some of the characteristics that make TCs destructive and potentially deadly—unless proper warnings and subsequent evacuations occur. For example, Figure 1.1 shows the percentages of deaths in the United States during 1963-2012 that were caused by different hurricane attributes. One of the most important findings from (Rappaport 2014) is that around 90% of fatalities are water related, most due to drowning. Storm surge, an abnormal rise in water pushed ashore by the strong winds of storms, is a significant source of loss of life for hurricanes. More detailed statistics and discussion can be found in (Rappaport 2014).

The destructive nature of TCs is often dependent on geography. For example, landslides—erosions in mountainous slopes from heavy rainfall—are concerns for those who live in mountainous regions in the path of tropical storms. Cyclone

Roanu (2016) caused dangerous landslides in Sri Lanka while still a weak tropical depression, leading to many fatalities and destruction.

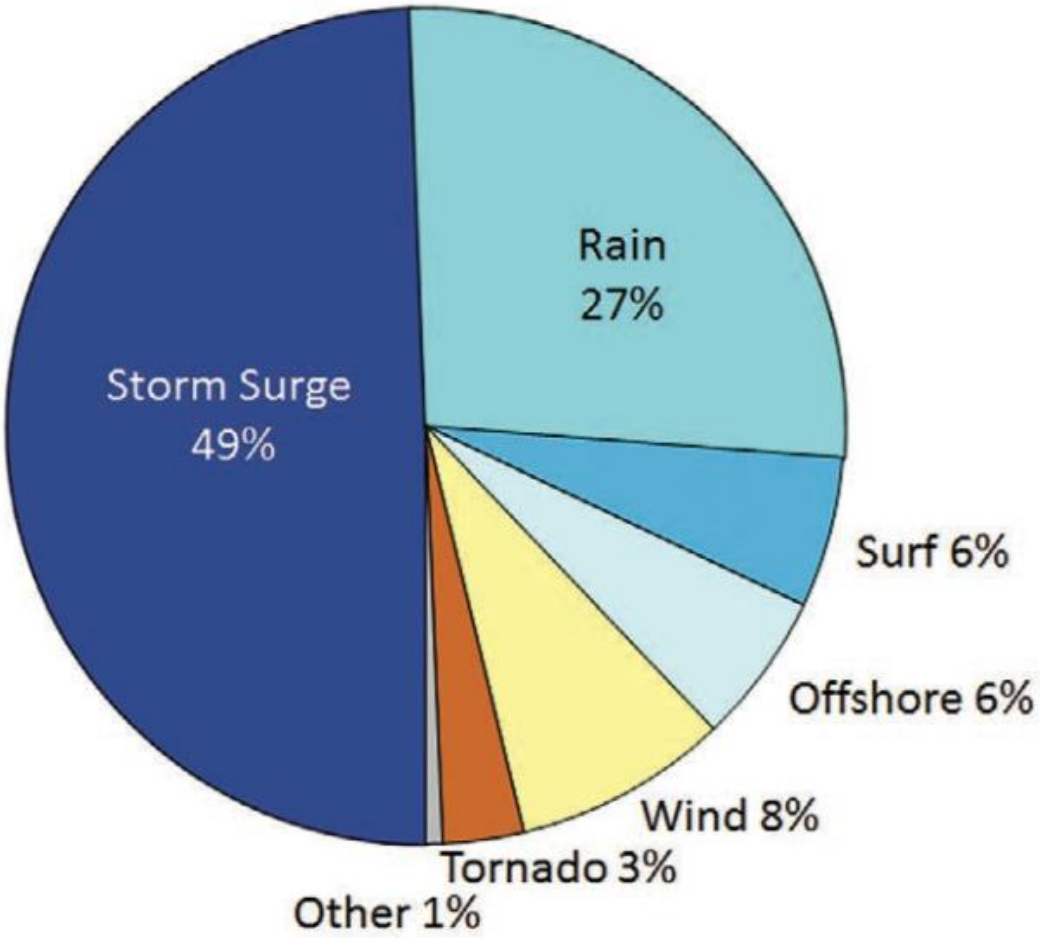

Figure 1.1: Cause of death in the United States directly attributable to Atlantic tropical cyclones, 1963-2012. Credit: (Rappaport 2014)

Before a hurricane can form, certain ingredients must be available. The first ingredient is warm sea surface temperature (SST)—typically above 26.5 °C. Warm SSTs fuel storms by enabling strong evaporation from the ocean surface. Sensible and latent heat fluxes warm and moisten the boundary layer air; this warm, moist air fuels the thunderstorms in the TC. Second, developing storms need to be in a region with a noticeable Coriolis force—generally thought to be locations at least 5 degrees away from the equator in latitude. Converging winds in the lowest level of the atmosphere are forced to flow around the center (or

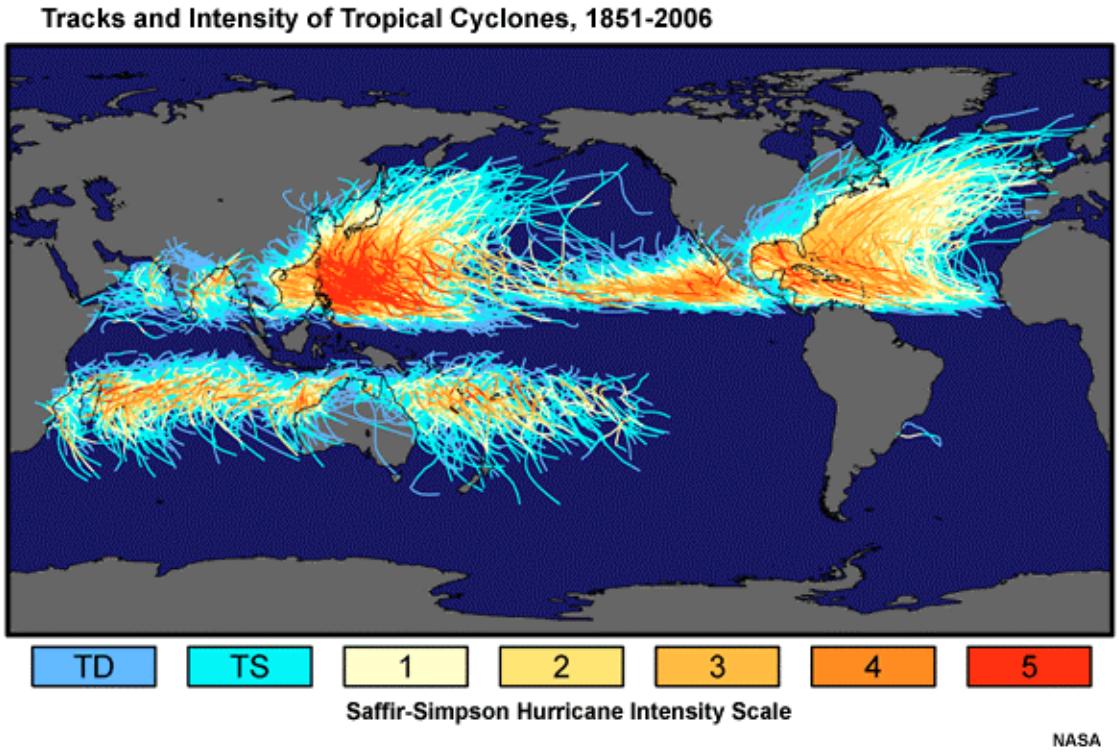

Figure 1.2: Global distribution of observed tropical cyclone tracks from 1851-2006 (where available) and the corresponding intensity according to the Saffir-Simpson Hurricane Intensity Scale. Credit: The COMET Program.

eye) of the storm through the Coriolis force, which helps to sustain and strengthen the low pressure in the eye of the storm. For intense convection to be supported, a few other ingredients must be in place. Convection is important since the latent heat that is produced from convective storms will fuel the TC. Low vertical wind shear helps to keep storms from tilting with increasing height; latent heat release is more concentrated in low wind shear conditions. Additionally, high humidity in the low-and mid-troposphere and conditional instability—when the environmental temperature lapse rate is less than the dry-adiabatic lapse rate, but greater than the moist-adiabatic lapse rate—helps to fuel convection. Finally, enhanced relative vorticity, or local rotation, in the lower troposphere helps to organize convective storms and potentially produce TCs. (Gray 1979, 1998)

The necessary conditions for TCs are generally present in the tropics, which explains why most TCs develop there. Figure 1.2 shows the track and intensity of

TCs observed from 1851 – 2006. The dearth of TCs forming in the South Atlantic and Southeastern Pacific result from a lack of some of the critical ingredients of TC formation. In the South Atlantic, vertical wind shear is generally too strong and there are no African easterly waves, or waves generated from the African easterly jet (Burpee 1972), to initiate storms south of the equator. In the Southeast Pacific, the sea surface temperatures are too cold and the vertical wind shear is too strong. The existence of the ingredients discussed previously is not enough to initiate a TC. Even if all ingredients discussed previously are in place, there also needs to be convergence within the boundary layer to fuel the thunderstorms that start the TC formation process. Synoptic scale horizontal convergence in the boundary layer is needed so that upward motion above this convergence zone can be initiated and supported. Examples of sources of convergence include, but are not limited to: monsoon troughs, the intertropical convergence zone (ITCZ), and easterly waves. Monsoon troughs are locations of relatively low sea level pressure in monsoon regions. The ITCZ consists of lines of deep convective clouds and heavy precipitation extending across the Atlantic and Pacific Ocean basins from around 5˚ to 10˚ north. Easterly waves are waves which move from east to west within the broad easterly current in the tropics. With upward motion, comes convective storm formation. (Holton 2004)

As highlighted in Figure 1.2, before reaching TC strength, TCs progress through categorizations of weaker strength: tropical depressions and tropical storms. Even before those categorizations apply, the first stage of the TC formation process is the tropical disturbance stage. In this stage, clusters of thunderstorms move collectively across the ocean. No eye or rotation will have developed at this stage. Condensation in the thunderstorms leads to latent heat release, which makes these disturbances warmer than the surrounding environment. Through the hypsometric relationship,

$$z_2 - z_1 = \frac{R_d \overline{T}_v}{g} \ln\left(\frac{p_1}{p_2}\right) \tag{1.1}$$

warming (an increase in the mean virtual temperature $\overline{T_v}$) in this disturbance will cause high pressure to develop above the storm and at the top of the troposphere. Here, the thickness ($z_2 - z_1$) of a layer of the atmosphere for a particular pair of pressure surfaces (p_1, p_2) is related to $\overline{T_v}$, where R_d is the dry air constant, and g is gravity. Development of high pressure above the storm is important since it will drive further enhancement at the next stages of development. (Stull 2015)

From tropical disturbances, tropical depressions can form. In this stage, the high pressure that has developed aloft leads to divergence aloft, which then leads to low pressure at the surface. Air flows into the disturbance within the boundary layer, up through the storm and out at the top of the troposphere. This inflow helps to supply warm moist air from the surrounding environment to build and sustain the convection. The inflow and outflow will be deflected slightly due to Coriolis forces, and rotation of the winds starts to appear visually as rain bands begin to align with these rotating winds. This stage is typically also identified by how strong the rotating surface winds are; for storms monitored by the National Hurricane Center (NHC) and Central Pacific Hurricane Center (CPHC), 1-minute sustained maximum surface winds must be less than 17 m s^{-1} in order to be categorized as a depression. During this phase of development, if low pressure continues to deepen through the balance of inflow and outflow, the system will continue to organize and strengthen towards the next phase. (Stull 2015)

Tropical depressions lead to tropical storms. The most noticeable difference between tropical storms and depressions is that the surface winds are now stronger. According to classifications employed by the NHC/CPHC, for a tropical storm to be identified, the 1-minute maximum sustained surface winds must be above 17 m s^{-1} but less than 33 m s^{-1}. Generally, convection will be concentrated in the center of the storm, so no eye is present yet, and the storm can now sustain itself without external forcing from the environment. Figure 1.3 shows the strength and track of Hurricane Earl, starting at tropical depression stage and

then intensifying to tropical storm strength at points 1 through 5. The same thermodynamics that fueled the depression continue to drive and strengthen the storm at this stage.

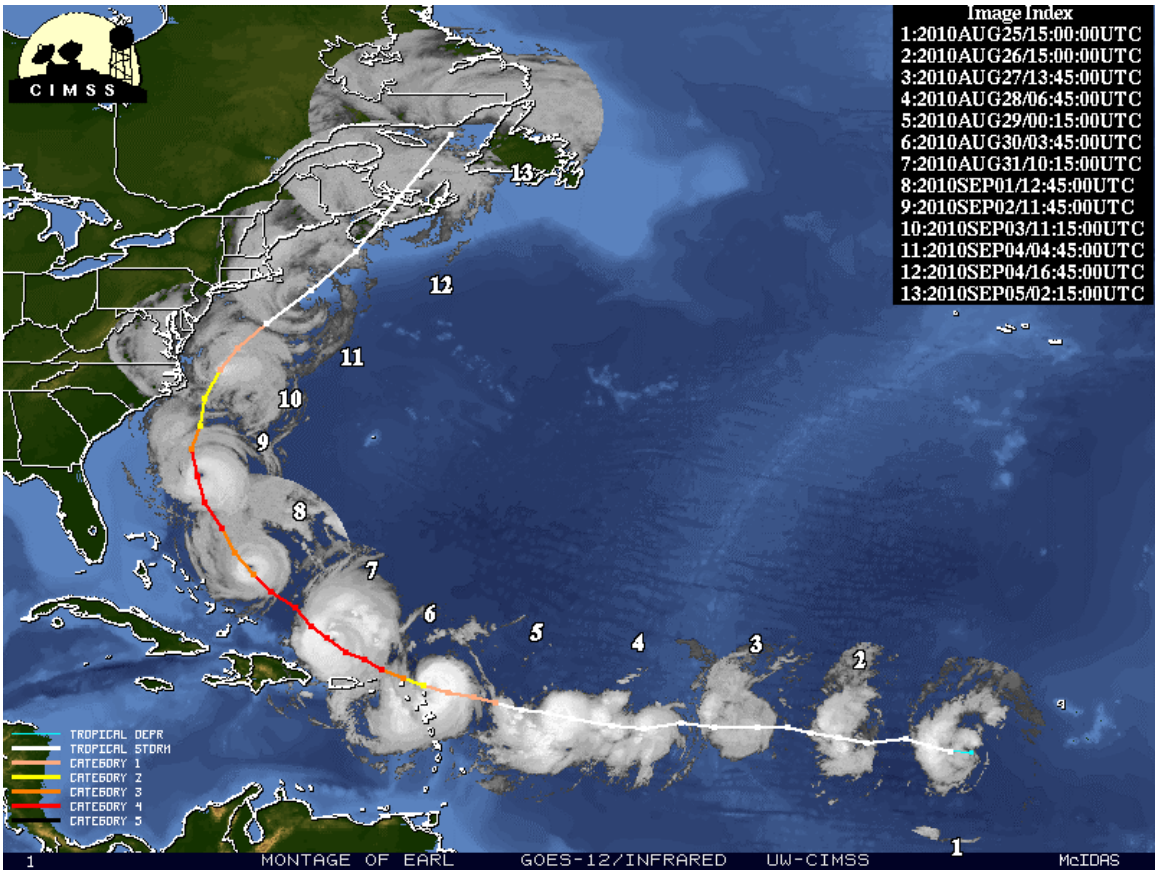

Figure 1.3: A mosaic of visible and infrared imagery over the lifecycle of Hurricane Earl (2012), with strength and track denoted for additional clarity. Courtesy of Cooperative Institute for Meteorological Satellite Studies/University of Wisconsin-Madison Tropical Cyclones Atlantic Storm Product Archive.

Once the maximum 1-minute sustained surface wind speed is above 33 m s^{-1}, a storm is classified as a TC—according to the classifications employed by the NHC/CPHC. At the TC stage, there are many unique visual characteristics that set this type of storm apart from the weaker stages. Figure 1.4 visualizes the key elements of TCs with a cross-sectional view.

As shown in Figure 1.3, Hurricane Earl—at TC strength from approximately time points 6 through 10—looks more symmetric and often has a visually clear eye; this matches what Figure 1.4 suggests. The most intense surface winds and rain are found in the eyewall, labeled in Figure 1.4.

It is useful to characterize the wind field of TCs with two main idealized circulations—the primary and secondary circulations. The primary circulation is composed of the approximately axisymmetric rotating winds around the eye. The winds in the primary circulation can be idealized and explained by the gradient wind balance (Willoughby 1990). In cylindrical coordinates, gradient wind balance is defined as

$$\frac{v_T^2}{r} + fv_T = \frac{1}{\rho}\frac{\partial p}{\partial r} \tag{1.2}$$

where v_T is tangential velocity, r is the radial distance from the axis of rotation, f is the coriolis parameter, ρ is air density, and p is air pressure. As the boundary layer winds flow inward towards the low pressure of the eye, the air begins to rotate cyclonically in order to conserve angular momentum. In the end, a three-way gradient wind balance exists between the horizontal pressure gradient force (term 3 in eqn. (1.2), the centrifugal force (term 1 in eqn. (1.2)), and Coriolis force (term 2 in eqn. (1.2)). All other things being equal, an increase in the horizontal pressure gradient across the storm will lead to stronger tangential winds. In Figure 1.3, the rotating winds of the primary circulation surrounding Earl's eye are evident in clouds embedded in the upper level outflow and lower level inflow. While the lower level outflow will flow cyclonically, an anti-cyclonic circulation eventually wins out at the top of the troposphere, as shown in Figure 1.4. (Frank 1977a; 1977b; Holton 2004)

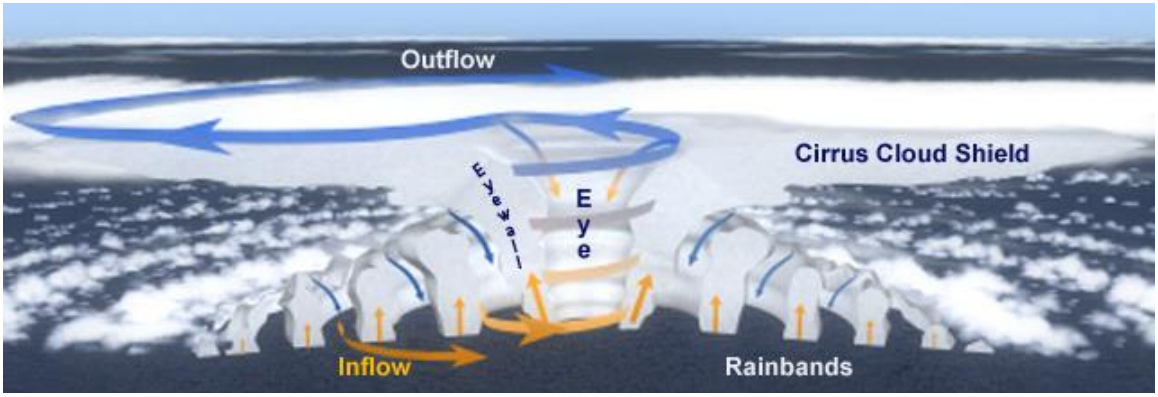

Figure 1.4: Conceptual model of the main structural elements of tropical cyclones: boundary layer inflow, clear central eye, eyewall and rain bands surrounding the eye, cirrus cloud shield and the upper tropospheric outflow. Credit: (Lang and Evans, 2016).

A TC's secondary circulation governs the energetics of a storm; it consists of the winds flowing inward radially and then vertically within the storm, as illustrated in Figure 1.4. The first leg of this circulation consists of the winds that flow inward within the boundary layer, picking up latent and sensible heat from the sea surface for fuel. On the second leg of this secondary circulation, winds turn upwards vertically through the eyewall, forming condensation that releases latent heat. At the tropopause, air flows outward to a large radius where air subsides toward the surface to complete the secondary circulation. This secondary circulation acts like an idealized Carnot heat engine; conversion of heat to mechanical energy makes TCs powerful and destructive. (Emanuel 1988; Willoughby 1988)

After reaching maximum intensity as a TC, there usually comes a dissipation phase. There are many reasons why TCs weaken. Usually, TCs either run into a harsh environment or they run out of fuel. For example, if TCs go over land or cooler SSTs, their main source of energy is cut off. After landfall, TCs not only have to deal with a lost energy source, they also have to deal with increased friction. For example, as Figure 1.3 shows, Hurricane Earl started to dissipate as it moved further north; here, it encountered cooler SSTs, a drier environment, and an increase in shear (Cangialosi 2011). At the very end of a TC life cycle, TCs sometimes evolve into extratropical cyclones. By the last time point in Figure 1.3, Hurricane Earl was extratropical.

As highlighted in the discussion above, many of the categorizations of different stages of a TC life cycle can be diagnosed based on the strength of surface winds and/or convection in the inner-core of the storm. Therefore, observations of these features are highly valued for situational awareness within the operational community. In order to advance the state of our understanding of TC processes, the TC research community also values observations of precipitation, clouds, and wind structure throughout the storm life-cycle. Observing TCs and their precursors have led to many advances in the science and forecasting of TCs. The next sections will give an overview of remote

sensing methods typically used to estimate important variables of interest for TCs: surface wind speed, precipitation, and intensity.

1.2 Remote Sensing of Oceanic Surface Wind Speed

1.2.1 Spaceborne Passive Microwave vs. Conventional Radar

1.2.1.1 Passive Microwave

As wind blows across the sea surface, it becomes rougher and more foam covered with increasing wind speed. Foam coverage increases surface emissivity because foam has an intermediate dielectric constant as compared with the highly mismatched dielectric values for sea water and air: sea foam acts as an impedance match at the surface interface and allows for the signal to couple through better (Williams 1969; Droppleman 1970). Surface roughness also increases brightness temperature (TB). Small, cm-scale roughness effects are important to consider below wind speeds of 7 m s^{-1}, before foam starts to cover the surface. As surface roughness increases, the local incidence angle changes and reflects downwelling atmosphere TB contributions back toward the sensor from higher slant paths (Wentz 1975). Overall, emissivity increases with increasing wind speed. Therefore, TB increases with increasing wind speed—a relationship exploited in surface wind speed retrievals (Meissner and Wentz 2012).

Some spaceborne passive microwave radiometers have a 10.7 GHz channel; this channel is considered useful for estimating wind speed since the atmosphere is somewhat transparent here (Ulaby et al. 2014). However, practical considerations including horizontal resolution and antenna size have to be taken into account in radiometer design. Half-power beamwidth β is related to the length of the antenna aperture l and the wavelength λ with

$$\beta = k \frac{\lambda}{l} \tag{1.3}$$

where k is some constant that is dependent on antenna design, and is usually between 0.88 and 1.5. Since, for a given antenna size, and with decreasing frequency (increasing wavelength), beamwidth increases and spatial resolution degrades, spaceborne passive microwave wind sensing missions typically do not use channels lower than 10 GHz. Higher frequency channels are used to increase spatial resolution. Using multiple channels, the parameters that make the atmosphere more opaque with increasing frequency can also be retrieved, in addition to correcting the surface wind speed retrieval for atmospheric effects.

One example of a microwave radiometer with channels below 10 GHz is WindSat—the first fully polarimetric microwave radiometer in space (Gaiser et al. 2004). While the 6.8 GHz channel is not fully polarimetric, most of the higher frequency channels—10.7, 18.7, and 37 GHz—are. Fully polarimetric—TB at H, V, slant linear (+/- 45 degrees), as well as right and left hand circular polarizations—observations can be used to retrieve not only wind speed but wind direction as well. The relationships between TB and wind speed and direction is summarized in Figure 1.5. The 6.8 GHz channel can be used in conjunction with the higher frequency wind channels to retrieve wind speed in all weather (Meissner and Wentz 2009), but with a degradation in spatial resolution since the 6.8 GHz channel provides observations over an effective spatial resolution of 39 km x 71 km. If the lowest frequency used in the retrieval is the 10.7 GHz channel, the spatial resolution becomes 25 km x 38 km, but then performance in heavy precipitation becomes more problematic.

Aircraft-based microwave radiometers take advantage of flying closer to the surface, and use lower frequencies than are typically found on spaceborne instruments without a performance loss in horizontal resolution. Now regarded as the gold standard measurement for TC surface winds, the Stepped Frequency Microwave Radiometer (SFMR) is routinely used in aircraft reconnaissance missions. SFMR works similarly to other microwave radiometers, but is more sensitive to high wind speeds and less impaired by the copious rain typical in TCs (Jones et al, 1981; Uhlhorn et al. 2007; Klotz and Uhlhorn 2014). SFMR is limited by the range of the aircraft it flies on and unfortunately only observes the

surface along a narrow track beneath the aircraft. A next generation instrument, the Hurricane Imaging Radiometer (HIRAD), looks to improve upon the limitations of the SFMR nadir-only swath by using a synthetic aperture radiometer to view a larger swath of the wind field (Amarin 2010).

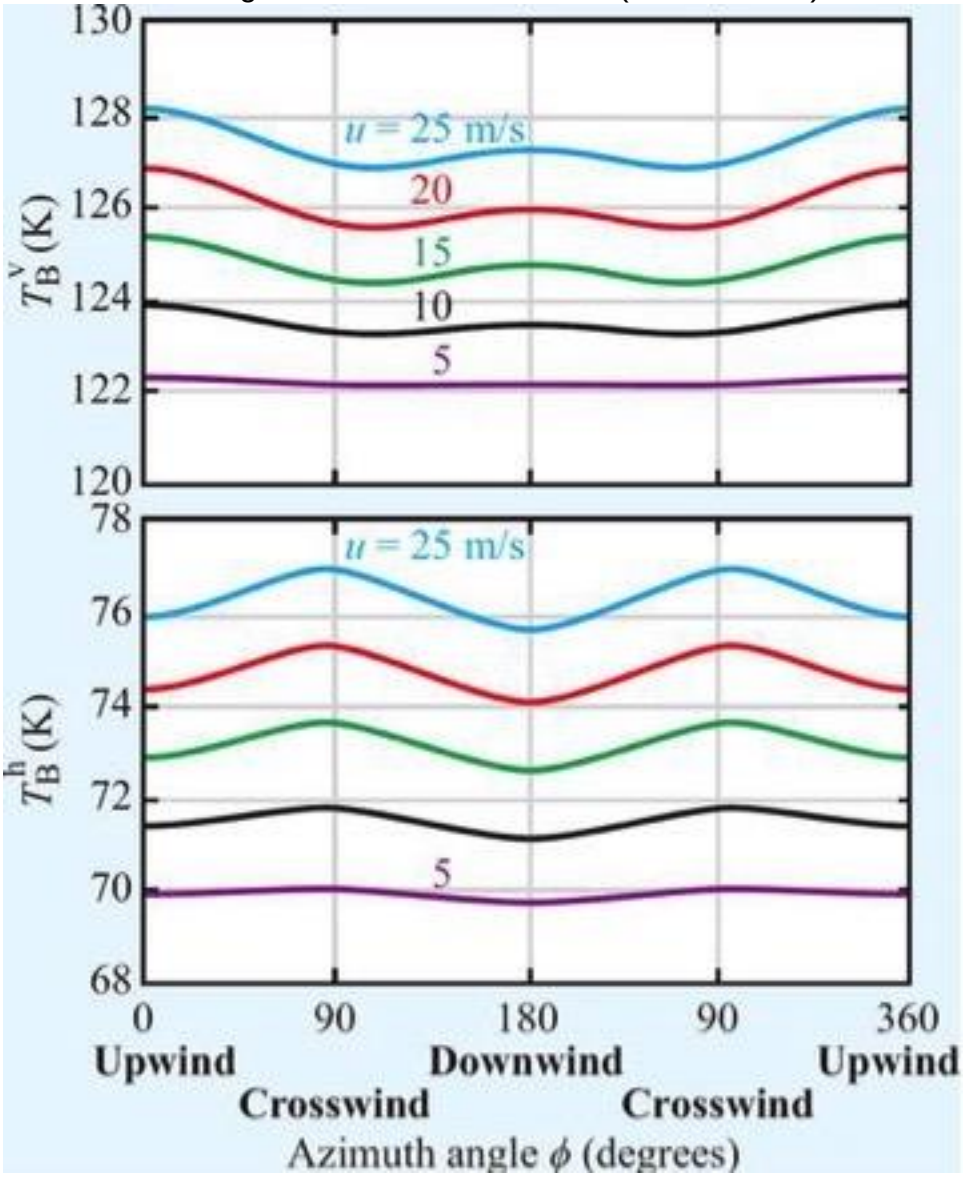

Figure 1.5: L-band model azimuth patterns for TB for v-polarization (TB^v) and horizontal polarization (TB^h) from (Yueh and Chaubell, 2012). Figure adopted from Ulaby et al. (2014).

1.2.1.2 Conventional Radar

Oceanic surface wind retrievals are possible through observations made by conventional radar type instruments: scatterometers, synthetic aperture radar

(SAR), altimeters. Scatterometers are active microwave sensors (radars) which observe the backscattered signal reflected off of the surface below them. From observations of the normalized radar cross section (σ_0) estimates of both oceanic surface wind speed and direction are possible. Scatterometers are some of the most established spaceborne instruments used to measure ocean vector winds, and some examples of spaceborne scatterometers include the Ku-band (around 14 GHz) NASA Quick Scatterometer (QuikScat) (Ebuchi et al. 2002), its replacement RapidScat (Madsen and Long, 2016) which was put onboard the international space station, and the ESA/EUMETSAT series of C-Band (around 5 GHz) Advanced Scatterometers (ASCAT) (Figa-Saldana et al, 2002).

Scatterometer measurements are sensitive to the roughness of the surface. Between incidence angles of 20 °-70 °, the return signal is proportional to the roughness of the surface on the scale of the radar wavelength. The wavelengths used by scatterometers match well to the scale of capillary waves on the ocean surface which are driven by local winds. The physical process forming the basis for scatterometer measurements—Bragg resonant scattering—results in a useful relationship between the backscattering coefficient, σ_0 , and surface wind speed. With increasing wind speed, ocean surface roughness increases, and σ_0 increases. Therefore, relationships between σ_0 and oceanic surface wind speed can be developed in the geophysical model functions which support the ocean vector wind retrievals from scatterometer observations. Wind direction also affects the σ_0 measurement and must be accounted for in the retrieval algorithms. In particular, σ_0 is dependent on the relative azimuth angle between the radar look direction and the wind direction. The relationships between σ_0 and wind speed and direction are summarized in Figure 1.6 for a single incidence angle and polarization. However, incidence angle and polarization both play a role here as well. The same functional form would be shown if hh-polarization had been plotted instead, but different empirical coefficients would change the

magnitude of the function plotted. The relationship of σ_0 with wind speed and incidence angle is explored in Figure 1.7. With multiple measurements of σ_0 at different geometric views, both wind speed and direction can be determined for a single location.

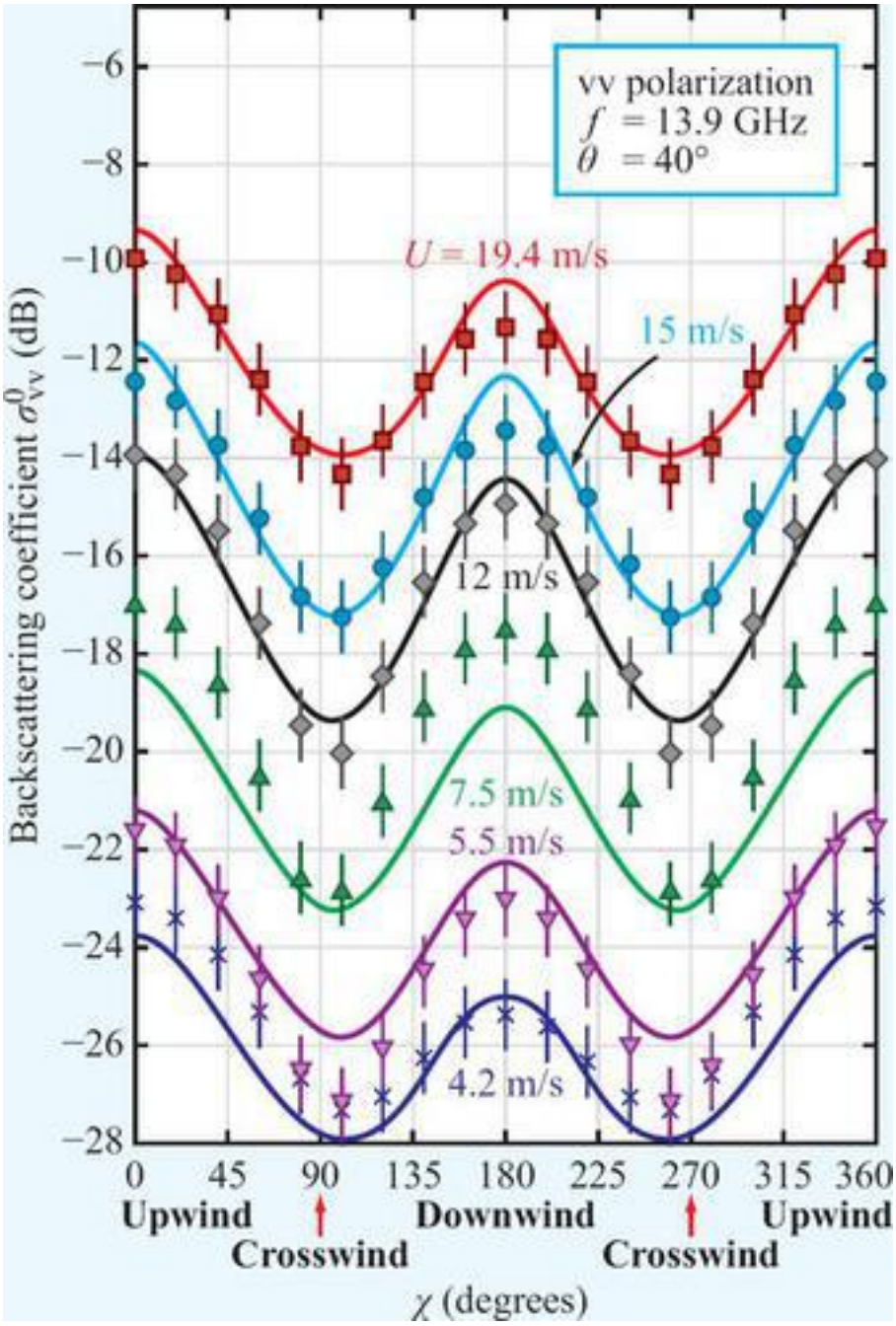

Figure 1.6: The backscattering coefficient versus wind –speed and azimuth angle at 13.9 GHz and 40 degree incidence angle. Note that the upwind backscatter is always larger than downwind and cross wind and that the backscattering coefficient always rises with wind speed. Measured data is from Schroeder et al. (1985). Figure from Ulaby and Long (2014)

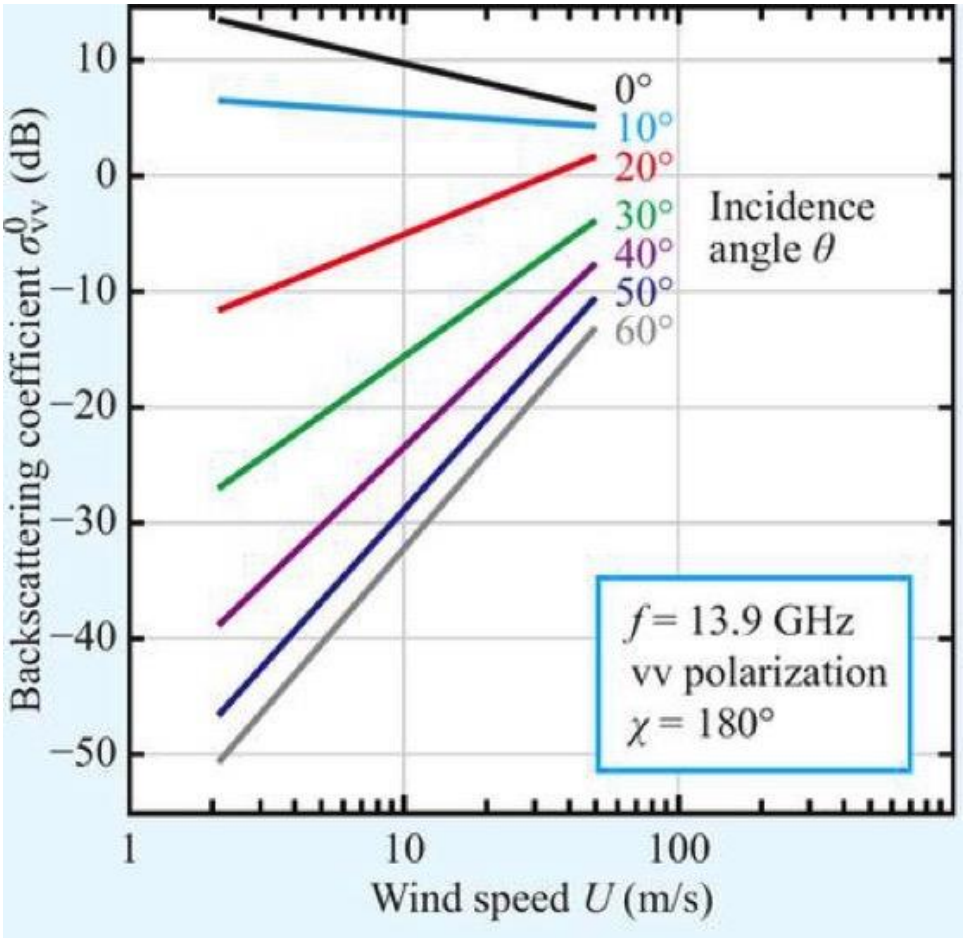

Figure 1.7: The Ku-band Seasat scatterometer (SASS-1) SASS-1 model (Schroeder et al., 1982) geophysical model function relating ocean surface σ^0 to the near-surface wind speed: σ^0 versus incidence angle for when the wind is blowing toward the radar (downwind). Adopted from Ulaby et al. (2014).

SAR observations also contain information about the ocean surface wind speed. Examples of operational SARs include the C-band RADARSAT-2 (Morena et al. 2014) and TerraSAR-X which operates at 9.65 GHz (Werninghaus and Buckreuss 2010). Like scatterometers, SARs measure σ_0, but unlike scatterometers, SARs measure σ_0 along single geometric looks for each pixel across a 2D image. Without multiple looks at a single location, the ambiguity, also seen in Figure 1.6, in the wind direction dependence remains in the SAR σ_0 measurements. Wind direction can be inferred from other sources (e.g. scatterometers, model data, or expected dynamic relationships for a given weather phenomenon). After wind direction is accounted for, wind speed is

estimated from the SAR σ_0 measurements. In comparison with scatterometers, SAR is also limited by swath size. Narrow SAR swaths have large gaps between them, making global coverage challenging on the weather time scales. Another major limitation is cost; SAR missions are much more expensive. If SAR were less expensive, it could be relied upon for ocean surface wind speed estimation.

Measurements made by another type of radar, altimeters, can also be used to estimate oceanic surface wind speed. Unlike scatterometers, altimeters consist of a nadir-looking radar, rather than an off-nadir-looking radar. An example of a currently operating spaceborne altimeter is the Poseidon-3 altimeter on the Jason-3 satellite, which operates at C- and Ku- bands (Vaze et al. 2016). While primarily used for determining surface topography and ocean surface height, the reflected altimeter waveform can be used to estimate near-surface wind speed. As with other radars, the measured σ_0 is used to estimate near-surface wind speed. However, since the altimetry measurements are from a nadir-looking sensor, σ_0 decreases with increasing wind speed. From the nadir point of view, as wind speed increases, the surface roughness increases, and more signal will be scattered away from the sensor. The utility of altimetry-based measurements for ocean surface wind speed applications is limited. As with SAR, altimeters also have low fractional Earth coverage since there are large gaps between the swaths.

1.2.1.3 Radar vs. Radiometer Summary

Radiometers—passive instruments—and radars—active instruments—measure different properties of the ocean surface. Oceanic surface wind speed estimation is possible from radiometer measurements as the emission from the surface is dependent on wind speed. Radars measure the backscattered signal, which depends on roughness, which is also related to near-surface wind speed. Rain affects both of these measurements. If the attenuation due to rain can be accounted for—for example, in SFMR's retrieval algorithm—it is possible to

estimate oceanic surface wind speed as long as the surface signal isn't too strongly attenuated. As frequency increases, attenuation from rain increases.

1.2.2 Monostatic Radar vs. Bistatic Radar

The conventional radar systems discussed in the previous section are all monostatic radars; the transmitter and receiver are in the same place and share a common antenna. If the transmitter and receiver are not in the same place, the instrument is a bistatic radar. Like their monostatic counterparts, bistatic radars are also used to estimate oceanic surface wind speed. Global Navigation Satellite System reflectometry (GNSS-R) techniques rely on a bistatic measurement geometry.

GNSS-R takes advantage of signals of opportunity from the existing network of GNSS satellites. The GNSS spacecraft act as the transmitting part of a bi-static radar, with the GNSS-R receiver receiving the forward signals that scatter from the Earth's surface. The GNSS satellites operate at low L-band frequencies which are insensitive to atmosphere and precipitation attenuation. Unlike scatterometers, which receive the backscattered signal, the GNSS-R receiver receives the forward-scattered signal from the Earth's surface, which is related to surface roughness and dielectric properties. In the forward scattering measurement, with increasing wind speed, surface roughness increases, and forward-scatter decreases (Garrison et al. 1998): this relationship is exploited in GNSS-R surface wind speed retrievals. The forward scattering measurement is more amenable to observations at low wind speeds, since this is when the signal will be strongest. Conversely, improved performance in scatterometry is expected for higher winds, since the backscattered signal is stronger in higher winds.

The history of GNSS-R is a bit shorter than that of scatterometry. Over the past 20 years, numerous aircraft and ground-based GNSS-R experiments have been performed (e.g. Garrison et al. 1998; 2002; Komjathy et al. 2004; Germain et al. 2004; Thompson et al. 2005; Katzberg et al. 2006; Rodriguez-Alvarez et al.

2013). The first spaceborne satellite with a dedicated GNSS-R sensor was UK-DMC in 2003 (Unwin et al. 2013). Since then, the UK TechDemoSat-1 satellite (TDS-1) launched in July 2014 (Foti et al. 2015) with the Space GNSS Receiver Remote Sensing Instrument (SGR-ReSI) on board. SGR-ReSI is a precursor to the instrument that will be used on the Cyclone Global Navigation Satellite System (CYGNSS) constellation, a NASA spaceborne GNSS-R mission (Ruf et al. 2016). The motivation for the CYGNSS mission is to measure oceanic surface wind speeds in all precipitating conditions—which will enable surface wind speed estimation even in the inner-core of TCs. GNSS-R performance has been tested in TC scenes through aircraft campaigns (Katzberg et al. 2001; 2006; 2013), but has yet to be demonstrated from a spaceborne platform, as UK-DMC-1 and TDS-1 never reported observations of TC strength winds.

There are many benefits to the applications of GNSS-R as compared with other methods. First, GNSS-R is not limited in regions of high precipitation. Second, GNSS-R takes advantage of the existing architecture of GNSS spacecraft such as the GPS constellation, making these spacecraft small, low power, and low cost. Third, since the locations of the receiver and transmitter determine the location of the specular point on the surface where the measurement is made, and since those locations are known quite well due to the GNSS position tracking capabilities, accurate antenna pointing and knowledge is not needed for this application (Ulaby et al. 2014). A disadvantage of the observations possible through this method include the fact that instead of a wide swath of observations—like scatterometer observations—GNSS-R observations resemble collections of tracks through an area. For gridded observations, GNSS-R observations need to be combined and interpolated intelligently based on the application.

1.2.3 Observations from Shorter vs. Longer Wavelengths

A persistent theme throughout this introduction is the fact that with increasing frequency, regardless of whether an active or passive sensor is used, the

observations will be increasingly affected by rain. Ocean surface wind measurements made at C-band and above (e.g. WindSat, QuikScat) will be affected by rain attenuation. In radiometer-based retrievals, C-band measurements can be used in tandem with multiple higher frequency observations to distinguish the wind and rain signals in the TB measurements. Measurements above 10 GHz will experience large enough attenuation in high precipitation scenes to significantly compromise their ability to make useful measurements of the surface.

In order to propagate to the surface in all precipitating conditions, L-band (or lower) sensors must be used. Observations from the Soil Moisture Active Passive mission (SMAP) (Fore et al. 2016) are useful for all-weather wind speed retrievals because the low frequency observations are uncontaminated by rain. However, observations by SMAP are limited to a relatively coarse spatial resolution of ~65 km, which can wash out much of the small spatial scale size, highest wind speed portions of TCs. Observations from the recently launched CYGNSS constellation will give more L-band observations in all precipitating conditions, but at 25 x 25 km^2 resolution (Ruf et al. 2016). Hopefully, GNSS-R receiver development will advance to give even higher spatial resolution measurements in the future.

1.3 Sensitivity of Remote Sensing to Precipitation

At certain frequencies, estimates of surface wind speed from passive microwave radiometers are possible—even in the presence of rain. Sensitivity to surface emission—ideal if estimates of surface wind speed are sought after—requires that transmissivity in the atmosphere be high at the frequency of observation. A transparent atmosphere allows for higher sensitivity to changes in surface emission, which allows for estimates of surface wind speed.

Remote sensing systems are designed to be sensitive to certain aspects of the environment, allowing for indirect estimation of the quantities in question. Sometimes, precipitation is part of the signal of interest. Sometimes, it is the

noise. And sometimes, it makes no impact. In this section, a comparison of examples from each of these situations is presented.

Passive microwave measurements have varying levels of rain sensitivity depending on frequency choice. Spaceborne passive microwave radiometers with channels above 10 GHz are sensitive to precipitation. Since the 1970's, passive microwave radiometers have been available to observe the emission from the atmosphere (Wilheit 1976; Weinman and Guetter 1977; Prabhakara et al. 1992). Initial examples of these microwave instruments include the Electrically Scanning Microwave Radiometer (ESMR) (Wilheit 1971; 1975) and the Scanning Multichannel Microwave Radiometer (SMMR) (Njoku at al. 1980). More recently, the series of passive microwave sensors on the Special Sensor Microwave/Imager (SSM/I) and Special Sensor Microwave Imager/Sounder (SSMIS), the Tropical Rainfall Measuring Mission (TRMM), the Advanced Microwave Scanning Radiometer (AMSR-E), the Advanced Microwave Scanning Radiometer-2 (AMSR-2), and Global Precipitation Measurement (GPM) core observatory are used for precipitation estimates (Hollinger et al. 1990; Kawanishi et al. 2003; Imaoka et al. 2010; Kummerow et al. 1998; Hou et al. 2014). Retrievals of precipitation are possible from observations by these types of instruments. Radiometer channel selection is determined based on the sensitivity of TB to the environmental parameter to be estimated, and on the orthogonality of sensitivity to the same parameter by different channels. Ideally, the sensitivity across channels will be independent and non-overlapping. In general, higher, but differentiatable sensitivity results in better retrieval performance.

Before discussing the physical basis of passive microwave radiometer retrieval algorithms, it is useful to consider the thermal radiation components in a brightness temperature (TB) measurement from a downward looking passive microwave radiometer. Brightness temperature represents the intensity of radiation emitted by a scene under observation and is defined by

$$TB = \frac{P}{kB} \tag{1.4}$$

where P is the power measured by the radiometer across a spectral bandwidth B , k is the Boltzmann constant. Considering an nadir earth scene from space,

$$TB = \varepsilon T_{SFC} e^{-\tau} + T_{UP} + (1-\varepsilon) T_{DN} e^{-\tau} + (1-\varepsilon) T_{COS} e^{-2\tau} \qquad (1.5)$$

where ε is the emissivity of the surface, T_{SFC} is the physical surface temperature, τ is the path-integrated atmospheric optical depth, $e^{-\tau}$ is the atmospheric transmissivity, T_{UP} and T_{DN} are respectively, the upwelling and downwelling atmospheric TBs, and T_{COS} is the cosmic microwave background TB. On the right hand side of eqn.(1.6), term one represents a scene's surface emission that propagates through the atmosphere, term two represents the upwelling atmosphere radiation, term three represents the reflected and transmitted downwelling atmosphere radiation, and the last term represents the reflected portion of the cosmic microwave background radiation. The path-integrated optical depth is defined for an integration through the entire atmosphere as

$$\tau(z_1 = 0, z_2 = \infty) = \int_{z_1}^{z_2} (\kappa_g + \kappa_e) dz \qquad (1.6)$$

where κ_g is the gaseous absorption coefficient with units of Np m^{-1}, κ_e is the extinction coefficient due to hydrometeors and clouds with units of Np m^{-1}, θ is the incidence angle of the propagation path calculated over the height z of the atmosphere. κ_e accounts for scattering and absorption with

$$\kappa_e = \kappa_a + \kappa_s . \qquad (1.7)$$

where κ_s is the scattering coefficient. The upwelling TB (T_{UP}) is given by

$$T_{UP} = \int_0^{\infty} \kappa_a(z) T(z) e^{-\tau(z,\infty)} dz \qquad (1.8)$$

where T is atmosphere temperature at height z. The downwelling TB (T_{DN}) has a similar form and is given by

$$T_{DN} = \int_0^{\infty} \kappa_a(z) T(z) e^{-\tau(0,z)} dz \tag{1.9}$$

where the key difference between T_{UP} and T_{DN} is in the integration limits for calculating the optical depth. The extinction and absorption from the atmosphere along the propagation path must be accounted for. However, the dominance of the atmosphere vs. the surface contributions towards TB depends on the frequency in question, as well as the scene in question. (Ulaby et al. 2014)

Signatures of rain exist in low-frequency microwave observations after rain absorbs and reemits radiation (Wilheit 1986). Over the ocean, rain-rate can be estimated with physically-based retrieval algorithms. The ocean has a low emissivity at microwave frequencies. Rain absorption and reemission will warm the TB over the cool background of the ocean surface. Missions like TRMM and GPM take advantage of this emission relationship and employ Bayesian type retrieval algorithms to instantaneously retrieve rain rate from low frequency observations and databases built offline (Kummerow et al. 1996; 2001).

It is also possible to estimate rain rate with higher frequency channels, where scattering signatures start to come into play. Sometimes, these high frequency channels were originally chosen for use in temperature and humidity sounding. Temperature sounding channels near the strong oxygen absorption lines (50-60 GHz or 118 GHz) and moisture sounding channels near the water vapor line (183 GHz) are used for indirect estimates of precipitation. Scattering-based rain rate retrievals that use these sounding channels are more empirically based (e.g. Staelin and Chen 2000, Chen and Staelin 2003, Surussavadee and Staelin 2008). While these estimates are empirical, they allow for estimates of precipitation over land.

Since land not only has a high emissivity, but also has highly varying and less well known emissivity values (Weng et al. 2001), emission-based rain rate retrieval methods are not useful for rain rate retrieval over land. The warm signal from rain absorption and reemission is not distinguishable from a warm land background. However, the scattering signatures from the ice particles within upper-levels of clouds are strong against the land background at high frequencies. In particular, the reflected upper atmosphere downwelling and cosmic microwave background radiation scatters back towards the sensor, causing a radiance depression, compared to its environment (Spencer et al. 1989; Kidd et al. 2013). There are empirical relationships between the scattering signatures and rain rate; these relationships support the retrieval algorithms that use high frequency channels to estimate rain rate.

At the frequencies used in spaceborne microwave radiometers—about 10 GHz to 183 GHz—precipitation will block the surface emission from the ocean. This can be explained by considering the typical range of sizes of rain drops vs. the wavelengths used on spaceborne passive microwave radiometers. Raindrops are typically around 0.5 - 3 mm (Rogers and Yau 1989) and the wavelengths of the 183 - 10 GHz channels range from roughly 2 - 30 mm. At the lowest frequencies, the wavelengths here are only about 10 times greater than the largest rain drops, and thus these observations are still sensitive to rain absorption and re-emission processes. In order to be insensitive to rain, the wavelengths used must be much greater than the size of the rain drops.

Passive microwave radiometers with frequencies below 10 GHz exist on aircraft. For example, the Stepped Frequency Microwave Radiometer (SFMR) works at the range of frequencies from roughly 4 - 7 GHz (Uhlhorn et al. 2007). At these frequencies, the observations are attenuated by rain, but not so much that the surface emission is attenuated completely. The 4 - 7 GHz channels correspond to wavelengths of roughly 40 - 70 mm. With wavelengths roughly 10 times greater than the largest rain drops, these channels are able to partially see through rain to the surface. SFMR was designed with TC surface wind speed

estimation in mind; here, rain is a source of noise which must be accounted for in retrieval algorithms. Rain only partially blocks the surface signal which is used to estimate oceanic surface wind speed, as described in section 1.3.

With increasing wavelength (and decreasing frequency) passive microwave observations are decreasingly sensitive to rain. Figure 1.8 summarizes the frequency dependence of the Mie extinction and absorption coefficients of rain, for a precipitation rate of 12 mm h^{-1}. Generally, as frequency increases, extinction increases. Below 10 GHz, extinction from scattering—the difference between the extinction and absorption coefficients—is insignificant.

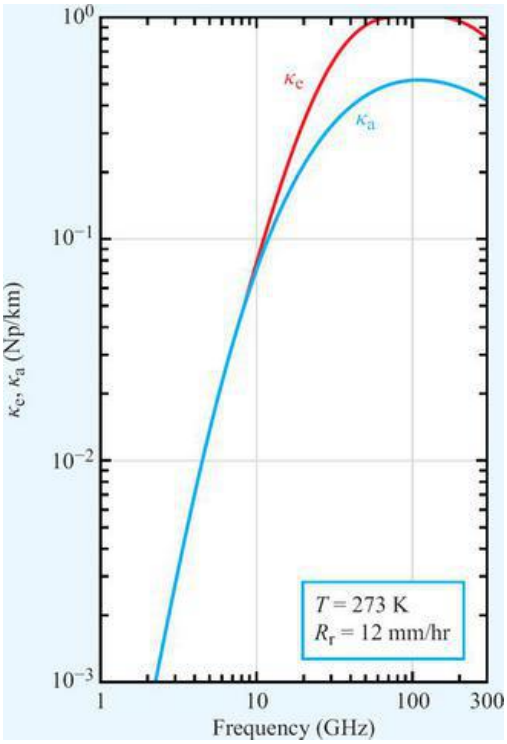

Figure 1.8: Calculated Mie extinction (κ_e) and absorption (κ_a) coefficients of rain characterized by a precipitation rate of 12 mm h^{-1}. [from Ulaby and Long, 2014; Tsang et al., 1977].

Approaching 1 GHz (L-band), both scattering and absorption due to rain become negligible. At L-band frequencies, the atmosphere is transparent in all weather, and the sensitivity to the surface is large. High surface sensitivity is

ideal for oceanic surface wind speed retrievals in all-weather conditions, as was discussed in section 1.2.

1.4 Remote Sensing of Tropical Cyclones

1.4.1 Importance of Tropical Cyclone Remote Sensing

TCs and their precursor storms spend most—if not all—of their lifetime over the ocean, which makes them harder to observe in situ. Since the advent of remote sensing, fewer TCs go unobserved, and our increased observation of these storms has led to improved understanding of TC processes. Additionally, the observations that are collected through remote sensing support the TC situational awareness and forecasting efforts at warning centers like the National Hurricane Center (NHC) (Rappaport et al. 2009).

TC forecasters are required to estimate the present and predict the future intensities of TCs, typically defined by a maximum 1- or 10-minute sustained wind speed at the 10-m observing level associated with the system (Harper et al. 2010; Office of the Federal Coordinator for Meteorological Services and Supporting Research 2012). Only 30% of the 6-hourly intensity estimates in the North Atlantic are guided by aircraft reconnaissance, and next to no aircraft reconnaissance is performed elsewhere (Rappaport et al. 2009). Unfortunately, intensity estimation is challenging without aircraft reconnaissance. Intensity estimates in the post-season reanalysis records have uncertainties of approximately 5 m s^{-1} (Landsea and Franklin 2013; Torn and Synder 2012). In addition to intensity, forecasters use information about precipitation and convective structure, the environmental conditions, and wind field size to guide their forecasts of TC track and intensity. Often, the observational guidance that TC forecasters use is based entirely upon remote sensing observations.

In recent years, hurricane intensity forecasts have started to improve, but, previously, forecasts in intensity lagged behind the skill improvement in track forecasts (Rogers et al. 2006). With further innovations in TC remote sensing,

particularly with regards to inner-core observations, TC forecasting will continue to improve and our understanding of the physical processes that underlie TC development will advance. While there are many types of remote sensing observations that support TC forecasts and process studies, this thesis will focus on the following three inner-core-related observations: precipitation, surface wind speed, and intensity.

Using observations of precipitation structure, TC forecasters can locate the center of a storm, determine the radius of the eye, and estimate the direction in which system intensity change is headed. A high interest observation is surface wind speed, which can inform estimates of the intensity of a system—a prioritized parameter in the operational forecasting environment.

1.4.2 Remote Sensing Applications to Tropical Cyclone Intensity and Wind Structure Estimation

Since TC intensity is a parameter that is prioritized in the operational TC forecasting environment, remote sensing-based methods have been developed to estimate intensity in situations where aircraft reconnaissance is not available. Currently, there are two main competing methods: the Dvorak and sounding-based techniques.

The Dvorak technique, a method of estimating TC intensity through subjective image pattern recognition, was first developed based on visible-sensors onboard geostationary meteorological satellites (Dvorak 1975). As Figure 1.3 suggests, it is possible to estimate TC intensity based on cloud patterns. Since the initial method was published, refinements and advancements have been made to the Dvorak technique (Velden et al. 2006; Velden et al. 1998). Infrared imagery is now included in the guidance (Dvorak 1984) and an automated version, called the Advanced Dvorak Technique (ADT) is a part of the suite of satellite-based guidance available to TC forecasters (Olander and Velden 2007). One disadvantage of the Dvorak technique is that it is an indirect and sometimes subjective approach. Brown and Franklin (2004) analyzed the performance of

Dvorak-based intensity estimates and found errors to be 2.5 m s^{-1} in roughly half the cases and over 6 m s^{-1} in a quarter of all cases. However, since the Dvorak technique relies on geostationary satellites, it is not plagued by data gaps typically seen if relying on polar-orbiting satellites alone.

Due to the ready availability of geostationary data, a variety of other methods for TC characterization—both intensity and wind structure estimation—have been developed for geostationary data (e.g. Mueller et al. 2006; Kossin et al 2007; Piñeros et al. 2008, 2011; Fetanat et al. 2013; Knaff et al. 2015; Dolling et al. 2016). A number of studies have developed methods which require an estimate of storm intensity in order to estimate wind structure from infrared data (Mueller et al. 2006; Kossin et al 2007; Knaff et al. 2011, 2015). The deviation angle variance (DAV) technique developed by Piñeros et al. (2008, 2011) correlates intensity and structure with the gradient in infrared brightness temperature; the DAV-based wind radii methods presented in Dolling et al. (2016) use a multiple linear regression technique. Fetanat et al. (2013) take advantage of historical hurricane satellite data (HURSAT) to estimate intensity from feature analogs—or brightness temperature patterns—in satellite imagery and analogous storms. In addition to infrared data inputs, the methods developed in Knaff et al. (2011, 2015) take advantage of multiple satellite inputs (i.e. a combination of more direct wind speed estimates from scatterometers and indirect flight-level wind speed estimates from geostationary and microwave sounder data) to estimate the TC wind field, from which wind radii are estimated.

TC intensity estimation is also possible using passive microwave sounders, like AMSU. This method takes advantage of the correlation between a TC's warm core structure and its intensity. Warm-core anomalies are greatest during peak intensity. Using the retrieved vertical temperature structure from AMSU, estimates of the minimum surface level pressure and maximum sustained wind speed are possible through the hydrostatic approximation and assumptions of gradient wind balance (Kidder et al. 2000). Care must be taken to account for the effect of clouds and precipitation on the AMSU radiances. The mean absolute

errors for AMSU-based maximum wind estimates developed in Demuth et al. (2006) are roughly 6 m s^{-1}. Although performance is comparable to the Dvorak technique, sampling of the TC inner core is limited since this method relies on polar-orbiting sounders.

In addition to intensity estimation, surface wind speed observations can also guide forecasters who analyze the extent of 34-, 50-, and 64- kt surface winds out from the center of a storm—commonly collectively referred to as wind radii. While AMSU does not have adequate horizontal resolution to estimate realistic wind structure alone, estimates of the 34-, 50-, and 64-kt wind radii and maximum wind speed can be made using statistically-based algorithms (Demuth et al. 2006).

Knaff et al. (2016) developed methods for estimating wind radii using routinely available estimates of TC intensity, motion, and location. These inputs, together with estimates of TC size from IR imagery or model analyses, are used to create a modified Rankine vortex—a vortex which follows a linear increase in wind speed from the center of the storm to the radius of maximum wind speed and an exponential decrease from the radius of maximum wind speed outwards—from which the wind radii are estimated.

1.5 Organization of thesis

While there are many aspects of TCs to observe and many tools from which to observe them, this thesis focuses on two main fields of remote sensing: passive microwave radiometry and GNSS-R. The work for this thesis was performed to support the algorithm and product development of two missions: HIRAD and CYGNSS. While these instruments operate on different scales, both have been developed with one main goal in mind: to measure ocean surface wind speed in tropical cyclones.

HIRAD is an airborne microwave radiometer operating at C-band frequencies. HIRAD is sensitive to rain emission and absorption, so algorithm development

revolved around properly modeling rain in HIRAD's forward model, as well as inverting the model to properly estimate rain rate. While the main aspect of the HIRAD algorithm project developed around better modeling the rainy atmosphere, ultimately, the goal is to improve surface wind speed estimation by properly accounting for the rain in the field of view. Chapter 2 outlines the algorithm work that is a part of this project, also published in Morris and Ruf (2015a).

Chapters 3 and 4 are both related to the CYGNSS mission. The objective of these projects is to determine how to take advantage of the unique observations from CYGNSS to estimate parameters of interest to the TC forecasting and research communities. Since this work was done before launch, an extensive set of simulated CYGNSS observations is used to develop algorithms and data products. Chapter 3 outlines how CYGNSS surface wind speed estimates can be used to estimate a measure of a TC's destructive potential, integrated kinetic energy (IKE). Chapter 3 is related to the work found in Morris and Ruf (2016a). Chapter 4 takes some of the methods developed in chapter 3, and adopts them to estimates of TC wind structure and intensity. The results and methods outlined in chapter 4 are currently in peer review (Morris and Ruf 2016b).

All of these projects are incremental steps in development for their respective missions. Future work and personal contributions are outlined in detail in chapter 5.

Chapter 2. A Coupled-Pixel Model (CPM) Atmospheric Retrieval Algorithm for the Hurricane Imaging Radiometer (HIRAD)

2.1 Summary

Low frequency, passive microwave observations allow for oceanic remote sensing of surface wind speed and rain rate from spaceborne and airborne platforms. For most instruments, the modeling of contributions of rain absorption and re-emission in a particular field of view is simplified by the observing geometry. However, the simplifying assumptions that can be applied in most applications are not always valid for the scenes that the airborne Hurricane Imaging Radiometer (HIRAD) regularly observes. Co-located Stepped Frequency Microwave Radiometer (SFMR) and HIRAD observations of Hurricane Earl (2010) indicate that retrieval algorithms based on the usual simplified model, referred to here as the Decoupled-Pixel Model (DPM), are not able to resolve two neighboring rain bands at the edge of HIRAD's swath. The DPM does not allow for the possibility that a single column of atmosphere can affect the observations at multiple cross-track positions. This motivates the development of a Coupled-Pixel Model (CPM), which is developed and tested in this chapter. Simulated observations as well as HIRAD's observations of Hurricane Earl (2010) are used to test the CPM algorithm. Key to the performance of the CPM algorithm is its ability to deconvolve the cross-track scene, as well as unscramble the signatures of surface wind speed and rain rate in HIRAD's observations. While the CPM approach was developed specifically for HIRAD, other sensors could employ this method in similar complicated observing scenarios.

2.2 Introduction

Most airborne and spaceborne sensors have observing geometries that allow for simplifying assumptions when modeling the rain that is present in their fields of view (Uhlhorn et al. 2007; Kummerow et al. 1996). The rain is assumed to exist only below the freezing level of the atmosphere. Figure 2.1.a shows the observing geometry of a typical spaceborne imaging radiometer. Note, this geometry works well in the emission and specular reflection regime, but would be more complicated if in the scattering regime.

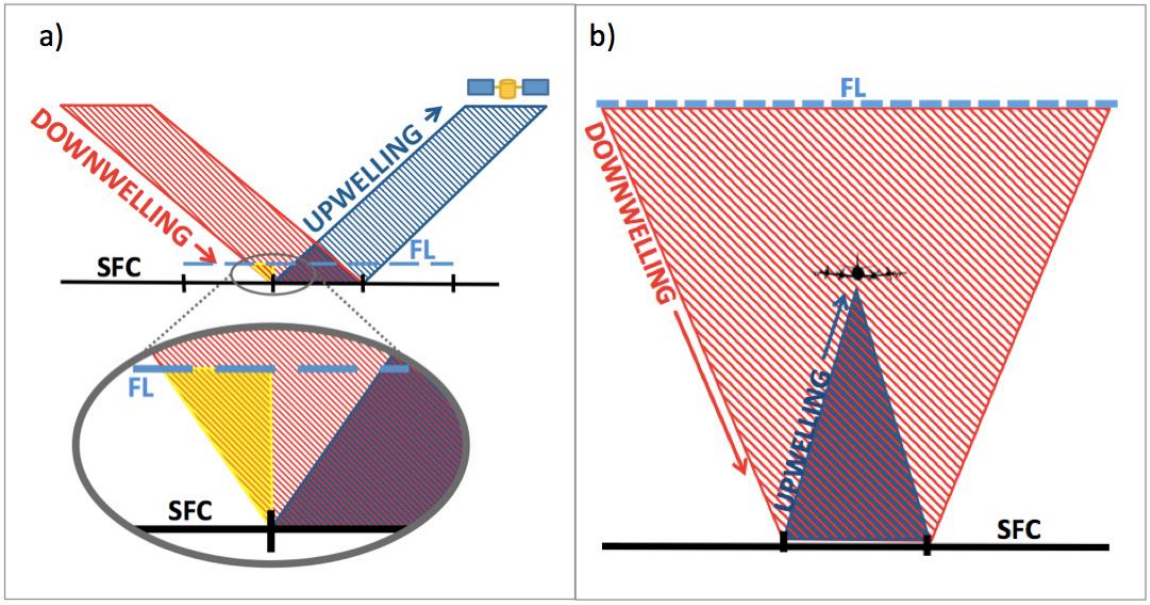

Figure 2.1: Typical observing geometry of: (a) a spaceborne microwave radiometer; and (b) the airborne stepped frequency microwave radiometer (SFMR) (not to scale). FL stands for freezing level, SFC stands for Earth surface. The yellow shaded region on the left represents the relatively small portion of the rain column below the freezing level that is not common to both the upwelling and downwelling emission sensed by the radiometer. The horizontal extent of individual pixels in the image is indicated by black vertical tick marks.

The horizontal extent of individual pixels in the image is indicated by vertical tick marks along the black surface boundary. The region of the atmosphere that contributes to a measurement at a particular pixel is indicated by the expanding conic boundary away from the sensor, denoted in Figure 2.1 by striped polygons. The dispersion of the cone is determined by the angular resolution of the sensor. Highlighted in yellow in Figure 2.1.a is the part of the rain column that contributes to the downwelling and not the upwelling thermal emission measured at a particular pixel, but would however contribute to the upwelling thermal emission in the neighboring pixel. The adjacent portion of the rain column that contributes

to both the upwelling and downwelling emission can be seen to be much greater. This is a direct result of the fact that the horizontal resolution of the imager's pixels is significantly greater than height of the freezing level. This condition is common with spaceborne radiometer imagers and is the reason why the radiative transfer models typically used in these applications assume that the upwelling and downwelling atmospheric emission originates from the same atmospheric column (Stephens and Kummerow 2007; Wilheit et al. 1994).

With varying degrees of validity, there are a variety of assumptions made when modeling radiative transfer. The work in this chapter can be put into better context by looking at the approaches used for cloudy atmosphere radiative transfer, ranging from the plane parallel assumptions, or 1-D modeling, to full 3-D radiative modeling (Cahalan et al. 2005). Other commonly used approximations, which are just steps above plane-parallel in complexity, include the independent pixel approximation (IPA) and the tilted IPA (TIPA). For IPA, the radiative properties of a given horizontal region are considered to be isolated from neighboring pixels (Cahalan et al. 1994), and the plane-parallel treatment is applied to particular columns. However, the IPA doesn't account for horizontal transport of radiative effects (Marshak et al. 1995; Zuidema and Evans 1998). In the IPA, each pixel is assumed to be radiatively independent of the others, and each column or horizontal region is assumed horizontally infinite. The IPA fails in certain situations because it doesn't account for the horizontal transport of radiation between pixels. A step up in geometry-complexity, TIPA takes into account the slant path of solar radiation, but is not a full 3-D treatment (Varnai and Davies 1999). The slanted-columns being modeled are still treated independently of one another.

Simplifying assumptions about radiative transfer can also be made for an airborne radiometer like SFMR, but for different reasons. SFMR is a nadir-looking radiometer with horizontal resolution on the order of typical convective rain cell features, and smaller than most stratiform rain distributions (Uhlhorn and Black 2003). Figure 2.1.b illustrates the relative contributions of the atmosphere below

the freezing level for this airborne observing geometry. In this case, a larger portion of the downwelling propagation path spills over into the next surface pixel. However, since large gradients in rain—on the order of 10 (mm h^{-1}) · km^{-1}—are unlikely at this horizontal scale, rain in the spillover region can be assumed to be similar to the rain in the main pixel of observation.

There are certain conditions under which the simplifying assumptions mentioned above are no longer valid. While developing a physically-based retrieval algorithm for the Hurricane Imaging Radiometer (HIRAD), these assumptions failed often. HIRAD was developed with the goal of achieving SFMR observing capabilities over a wider cross-track swath; therefore, initial retrieval algorithm development for HIRAD was based on established SFMR algorithms (Amarin et al. 2012). However, approximations, similar to IPA, that are reasonable given SFMR's nadir viewing geometry become much less valid for HIRAD's non-nadir pixels, especially at the higher incidence angle portions of its swath edge and in a tropical cyclone environment.

Co-located HIRAD/SFMR observations of Hurricane Earl (2010) during GRIP (Braun et al. 2013) exposed the flaws in using SFMR-like assumptions in the forward radiative transfer model on which HIRAD's retrieval algorithm is based. HIRAD and SFMR were on separate aircraft, flying perpendicular to one another. HIRAD was flying north on a WB-57 at roughly 20 km in altitude, with Hurricane Earl's western eyewall to its right. SFMR was observing from a NOAA P-3 at roughly 3 km and flew directly over the same western eyewall going from east to west. In this instance, SFMR's nadir observations were able to identify two neighboring, but distinct, rain bands as it flew directly over them. HIRAD, on the other hand, was not able to distinguish between the two when they were imaged at the outer edge of its field of view.

The simplified radiative transfer model used by SFMR and by typical spaceborne radiometer retrieval algorithms, in which each surface pixel has associated with it a single atmospheric column that is directly above it and is responsible for both upwelling and downwelling emission and absorption, will be

referred to here as the Decoupled Pixel Model (DPM), and is similar to the IPA. It is decoupled in the sense that the atmosphere observed at each pixel is assumed to be independent of that at any other pixel, so that retrieval algorithms can independently solve for surface and atmospheric state variables at each pixel. A Coupled Pixel Model (CPM) is developed here, which explicitly accounts for the possibility that upwelling and downwelling emission and absorption at a single pixel can result from different portions of the atmosphere, and that a given portion of the atmosphere can affect measurements at multiple pixels in the image. In this case, a corresponding retrieval algorithm will need to couple its geophysical state estimates across multiple pixels in the image. The CPM method combines ideas from TIPA and 2-D radiative transfer modeling.

Since HIRAD regularly observes tropical cyclone conditions in the outer-most incidence angles of its large cross-track swath, a new retrieval algorithm was developed based on the CPM. A key feature of the CPM algorithm is that it is able to deconvolve the cross-track scene, as well as unscramble the signatures of surface wind speed and rain rate in HIRAD's observations. While HIRAD will benefit directly from this method, the CPM algorithm approach could potentially be used in other applications and with other sensors, in cases where the horizontal resolution of the imager is comparable to or less than the depth of the atmospheric column within which a significant portion of the atmospheric attenuation and emission originates.

The objectives of this chapter are to present the CPM algorithm and compare its performance to that of the DPM. We hypothesize that the performance will be comparable in conditions without significant horizontal variability in the rain at the scale size of the HIRAD spatial resolution, and better in highly variable conditions such as a double rain band. To begin, section 2.3 highlights key differences in the forward radiative transfer models used in DPM and CPM methods. Section 2.4 outlines the set of simulated observations used to test the CPM algorithm. Section 2.5 describes the CPM algorithm. Results of the CPM performance tests

are reported in Section 2.6. Finally, a discussion of these results is summarized in section 2.7 and concluded upon in section 2.8.

2.3 Decoupled and Coupled Forward Radiative Transfer Models

The appropriate radiative transfer forward model to use given HIRAD's observing geometry depends on assumptions about the atmosphere along the propagation path. A typical situation for off-nadir pixels in the HIRAD image is shown in Figure 2.2. Regions 1 and 5 in the figure are modeled as a rain-free gaseous atmosphere above the freezing level. Below the freezing level, where rain may be present, region 2 is the downwelling-only portion of the propagation path, region 3 is the overlapping area of both upwelling and downwelling portions of the path, and region 4 is the upwelling only portion of the path.

Figure 2.2.a illustrates how the Forward Radiative Transfer Model (FRTM) considers the atmosphere under the DPM assumption. The rain in the downwelling path is assumed to be the same as that in the upwelling path. In cases of significant horizontal non-uniformity in the rainfall, such as near the TC eyewall, this assumption may not be valid.

Figure 2.2.b highlights the differences in the FRTM under a CPM assumption. The downwelling and upwelling atmospheres are considered separately, without, for example, assuming that the rain in region 3 is the same as that in region 2 or 4. Note also that the atmosphere along the upwelling and downwelling paths that are associated with a particular surface pixel also pass over other surface pixels. For example, the downwelling path in Fig.2.b passes over three surface pixels,

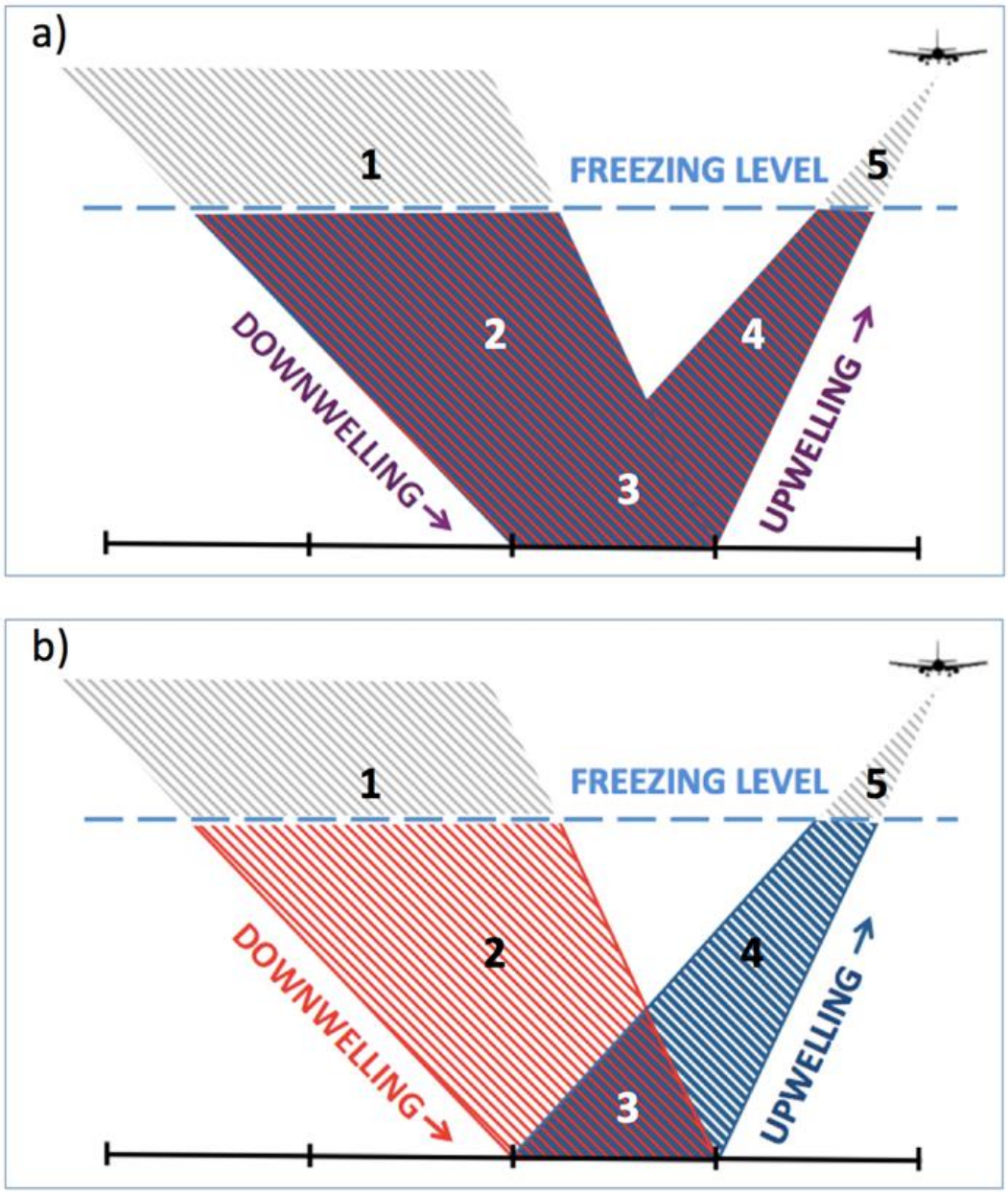

Figure 2.2: Diagram showing the assumptions made about the below-freezing-level atmosphere in a decoupled-pixel (DPM) (a) vs. coupled-pixel (CPM) (b) forward model. The horizontal extent of individual pixels in the image is indicated by black vertical tick marks. Regions 1 and 5 are modeled as a gaseous atmosphere without rain. Region 2 is the downwelling-only portion of the observing path for a particular field of view. Region 3 is the overlapping area of upwelling and downwelling portions of the path. Region 4 is the upwelling only portion of the path. (a): In the DPM model, regions 2-4 are modeled assuming the upwelling and downwelling paths have the same rain. (b): In the CPM model, there is no longer an assumption that the same rain is seen along the upwelling and downwelling paths. While there is a small portion of overlap in the paths (region 3), regions 2 and 4 are not assumed to have the same rain as region 3.

while the upwelling path passes over two. The footprint of these pixels is dependent on the horizontal resolution of the sensor, which is detailed in Amarin (2010). The appropriate FRTM in this case first requires that the total optical

depth along the upwelling and downwelling paths, τ_{UP} and τ_{DN}, be calculated from the total rain column that is present along each propagation path. The total is calculated by weighting and summing the rain rate above each pixel according to the cross-sectional volume of atmosphere that the path cuts through below the freezing level (see Appendix for details). Once the two optical depths are calculated, the corresponding upwelling and downwelling TBs are determined similar to (Amarin 2010) with (1) and (2) respectively:

$$T_{UP} = \int_0^{TOA} \kappa_a(z) T(z) \sec(\theta) e^{-\int_z^{TOA} \kappa_a(z') \sec(\theta) dz'} dz \quad (2.1)$$

$$T_{DN} = \int_0^{TOA} \kappa_a(z) T(z) \sec(\theta) e^{-\int_0^{z} \kappa_a(z') \sec(\theta) dz'} dz \quad (2.2)$$

where κ_a is the absorption coefficient, T is the physical temperature (K), z is the height in the atmosphere, TOA is the top of the atmosphere, which is assumed to be 20 km in this application, and θ is the Earth incident angle. The observed TB, including atmospheric emission and attenuation as well as surface emission and reflection, is modeled as

$$T_B = T_{UP} + e^{-\tau_{UP}} \left(\varepsilon T_{SFC} + (1-\varepsilon) \left(e^{-\tau_{DN}} T_{COS} + T_{DN} \right) \right) \quad (2.3)$$

where T_{SFC} is the physical sea surface temperature, ε is the emissivity of the sea surface, and T_{COS} is the cosmic microwave background TB. The total, path integrated, transmissivity is represented in eqn. (2.3) for the individual upwelling and downwelling propagation paths as $e^{-\tau_{UP}}$ and $e^{-\tau_{DN}}$, respectively. The emissivity of the surface is modeled based on earth incidence angle (EIA), sea surface temperature, and wind speed with an emissivity model developed for HIRAD (El-Nimri et al. 2010). With this FRTM, TBs are modeled for the entire cross-track scene in increments of $\sin^{-1}(\theta)$ in EIA. Those TBs are then weighted with HIRAD's antenna pattern to determine the observed TBs. Observed TB is calculated as

$$T_{B_{weighted_j}} = \sum_{i=1}^{m} T_{B_i} W_{ij} \qquad (2.4)$$

where $T_{B_{weighted_j}}$ is the observed TB value at a particular cross-track location j, T_{B_i} is the unweighted TB at a particular cross-track location i, and W_{ij} is the normalized weight of the antenna pattern for the field of view at cross-track location j, at the same cross-track location of T_{B_i}. The number of cross-track positions is m. Examples of the antenna pattern at EIA = 7°, 36°, and 62° are shown in Figure 2.3. Also plotted in Figure 2.3 is the half power beam width (HPBW). HPBW is the angle between points in the antenna pattern where the power is half of the maximum. With increasing EIA, HPBW increases.

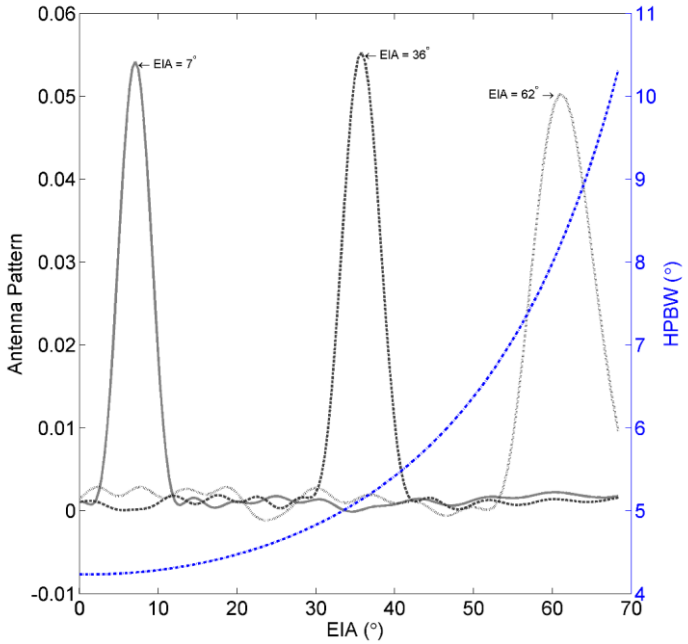

Figure 2.3: The relationship between HIRAD's beamwidth and synthetic antenna pattern with earth incidence angle (EIA). Portions of synthetic antenna beam patterns are shown in grayscale for EIA of 7°, 36°, and 62°, and are labeled in the figure. Plotted in blue is the half power beam width (HPBW). HPBW is the angle between points in the antenna pattern where the power is half of the maximum.

2.4 Simulated Observations as Test Cases

A set of simulated HIRAD observations was developed using the CPM FRTM in order to test the CPM algorithm. There are three main test case categories: horizontally uniform (or constant) conditions, a single rain band, and a double rain band. The test cases are summarized in Figure 2.4 and Table 2.1. Figure 2.4 gives a visual glimpse of the cross-track scene in each case, while Table 2.1 outlines the case identification numbers and quantifies some of the parameters illustrated in Figure 2.4.

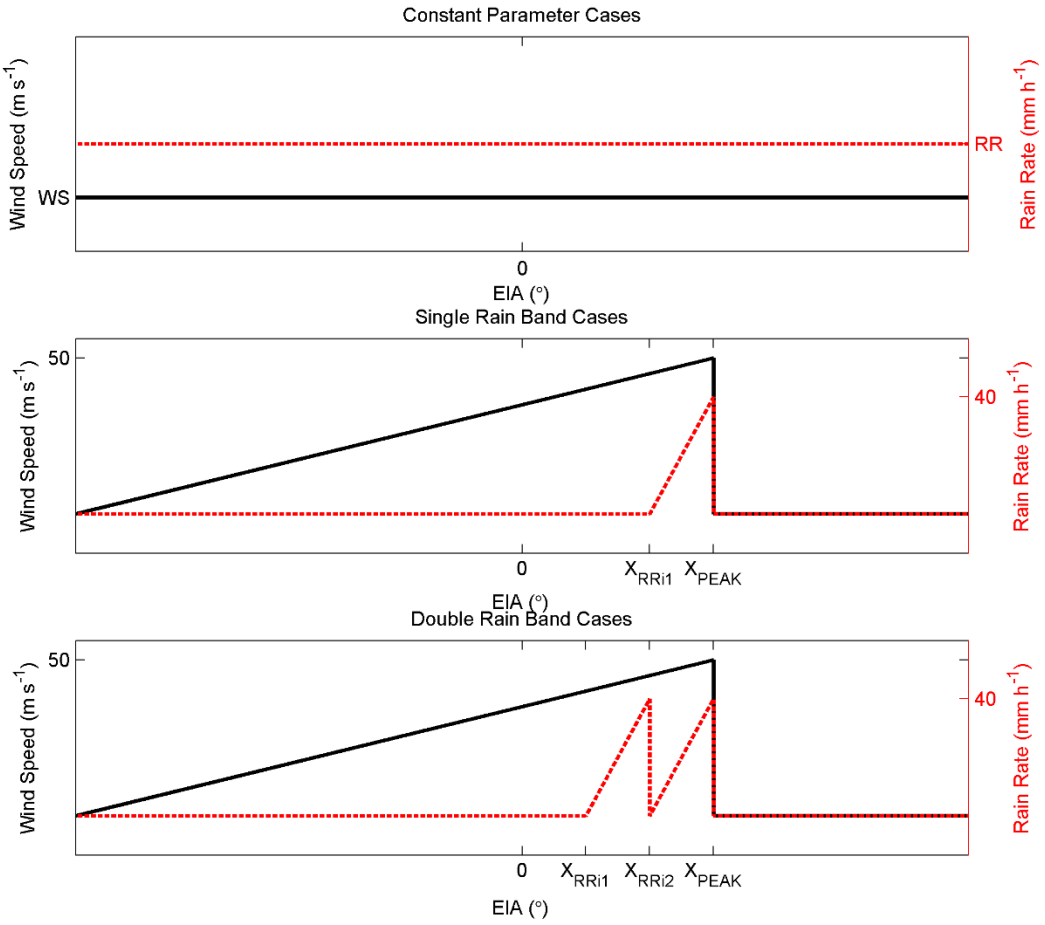

Figure 2.4 Portrayals of the true surface wind speed (m s^{-1}) and rain rate (mm h^{-1}) used to simulate observations for each case type. The X parameters are labeled on the x axis to provide reference to Table 2.1 and are quantified in Table 2.1 for each test case ID number. X_{RRi1} is the horizontal distance to the point in the cross-track swath where the first (or only) rain band begins, from 0 ° EIA. X_{RRi2} is the distance to the point in the cross-track swath, from 0 ° EIA, where the second rain band begins (double rain band cases only). X_{PEAK} is the distance to the point in the cross-track swath, from 0 ° EIA, where wind speed and the outer rain band peaks.

Table 2.1: Summary of simulated test case identification numbers, and descriptions of the true surface wind speed (m s^{-1}) and rain rate (mm h^{-1}) for each case. The parameters of WS, RR, X_{RRi1}, X_{RRi2}, and X_{PEAK} are labeled in Figure 2.4 for a visualization of the types of cases simulated. X_{RRi1} is the horizontal distance to the point in the cross-track swath where the first (or only) rain band begins, from 0° EIA. X_{RRi2} is the distance to the point in the cross-track swath, from 0° EIA, where the second rain band begins (double rain band cases only). X_{PEAK} is the distance to the point in the cross-track swath, from 0° EIA, where wind speed and the outer rain band peaks. The identification numbers provide information about the particular test case. In the constant cases, the number before the 'w' gives the true wind speed and the number before the 'r' gives the true rain rate. In the rain band cases, the number before the letter 's' or 'd' gives the EIA location of X_{PEAK}.

Constant Cases: Constant Wind Speed/Rain Rate		
Test Case ID	WS (m s^{-1})	RR (mm h^{-1})
10w10r	10	10
10w40r	10	40
50w10r	50	10
50w40r	50	40
Single Rain Band Cases: peak wind speed = 50 m s^{-1}; peak rain rate = 40 mm h^{-1}		
Test Case ID	X_{RRi1} (km)	X_{PEAK} (km)
20s	3	7
30s	7	10
40s	10	15
50s	15	21
60s	21	31

Double Rain Band Cases: peak wind speed = 50 m s^{-1}; peak rain rate = 40 mm h^{-1}			
Test Case ID	X_{RRi1} (km)	X_{RRi2} (km)	X_{PEAK} (km)
20d	0	3	7
30d	3	7	10
40d	7	10	15
50d	10	15	21
60d	15	21	31

Constant cases illustrate the performance of the CPM algorithm in different combinations of constant high and low retrieved parameters, where the retrieved parameters are surface wind speed and rain rate. The identification numbers in Table 2.1 give information about the amount of true wind speed and rain rate in that particular simulated test case. For the constant cases, the true wind speed is the number before the ‘w’, and the true rain rate is the number before the ‘r’. Figure 2.4 shows that the true wind speed and rain rate are held constant for the entire cross-track scene in the constant parameter test cases.

In addition to the constant parameter cases, idealized cases of a TC eyewall overpass—where the eyewall cuts through perpendicular to the cross-track view of the instrument—are also considered. The wind speed is assumed to linearly increase up to the location of the eyewall, followed by a drop in wind speed in the eye. Coinciding with the area of highest winds is an area of intense rainfall. Both single and double rain bands at the eyewall are considered. The cross-track location of the eyewall is also an important feature to consider because the amount of coupling in the CPM FRTM is dependent on the cross-track location. Therefore, cases with different eyewall cross-track locations are considered.

Test cases with an ‘s’ after the identification number in Table 2.1 have a single rain band and cases with a ‘d’ after the identification number have a double rain band. The identification number in these test cases corresponds to the EIA in HIRAD’s cross-track swath at which the eyewall peaks. For these cases, the wind speed peak value is always 50 m s^{-1} and the rain rate peak value is always 40 mm h^{-1}. For convenience, Table 2.1 also includes approximate horizontal cross-track distances from 0° EIA that match these EIA points in the cross-track swath, labeled in Figure 2.4.

2.5 Inversion Algorithm

2.5.1 Procedure

The FRTM is inverted using an iterative least squares estimator to retrieve surface wind speed and rain rate from HIRAD's TB observations. To start, a first guess of wind speed and rain rate is estimated. The first guess is found by considering TBs with a range of wind speed and rain rate pairs, and choosing the pair that results in the lowest difference between the observed and modeled TB. This procedure is performed for each cross-track pixel individually, using the DPM version of the FRTM. A uniform cross-track wind speed and rain rate distribution is assumed as the first guess, with their values being the average of all the initial cross-track best guesses found.

With a first guess of wind speed and rain rate, the iteration process can start. Each iteration, a jacobian matrix is populated using the FRTM for each retrieved value at each EIA as

$$J_{ij} = \frac{\partial T_{Bi}}{\partial g_j} \tag{2.5}$$

where g_j is the wind speed or rain rate, the retrieved state variables. At the edge of the swath under the CPM assumption, we need to extend the jacobian matrix to account for the extra downwelling atmosphere that extends past the surface pixel at the swath edge. This creates an [m x n] matrix where m is the number of cross-track TB observations and n is the sum of the number of wind speed and rain rate retrievals being solved for. In this CPM application, n is twice the number of pixels plus two, in order to account for the extra rain rate retrievals attempted for the outer downwelling atmosphere at the edge of the swath. After J is populated and beam averaging is accounted for, the update to the state vector is estimated as

$$\partial g = \left(J^T J + R\right)^{-1} J^T \partial T_B \tag{2.6}$$

where R is a diagonal regularization matrix given by $R = \gamma I$ where I is the identity matrix, and ∂T_B is the vector of residual differences between the observed TB and the TB estimated by the FRTM given $\vec{g}$. The amount of regularization is determined by the regularization parameter γ.

The state vector, $\vec{g}$, is updated with ∂g and this iterative process continues with the goal of minimizing the difference between the forward modeled TB and the observed TB. We define convergence when a decrease in the RMS value of from one iteration to the next is less than 0.01 K, or if the RMS value increases. We determined the threshold value of 0.01 K after repeated experimentation with the algorithm. This threshold value, specific to these retrieval performance tests, insures that the run time for a retrieval is reasonable.

2.5.2 Regularization Issues

Regularization is used to decrease noise sensitivity in the inversion process. However, over-regularization can have detrimental effects on the retrieval. We use the set of simulated test cases to determine a satisfactory value for γ. Figure 2.5 shows the average error in retrieved wind speed and rain rate, over all simulated cases, for a range of γ values. We limit our investigation of errors to the portion of the cross-track +/- 5° around the rain bands, for those cases with rain bands, in order to emphasize the performance of the retrieval near the rain bands more than the calmer portions of the scene.

The blue line in Figure 2.5 represents the component of retrieval error not due to random additive noise (the so called “intrinsic” error in the retrieval algorithm). The red line in Figure 2.5 represents error due to noise sensitivity. Errors representing both components are based on the RMS difference between the true and retrieved values. The “intrinsic” error was calculated from retrievals that used simulated TBs with no added noise. In order to estimate the component of error due to noise sensitivity, 25 realizations of noisy simulated TBs were developed by adding random Gaussian noise with a standard deviation of 1 K to

the noise-free simulated observations. One realization consists of a single set of cross-track TBs. Using those 25 realizations of noisy observations, 25 retrievals were performed. The error due to noise sensitivity is based on an average of those 25 realizations of noisy retrievals. The choice of 25 realizations was found to be adequate to produce repeatable results of overall retrieval residuals in a reasonable run time.

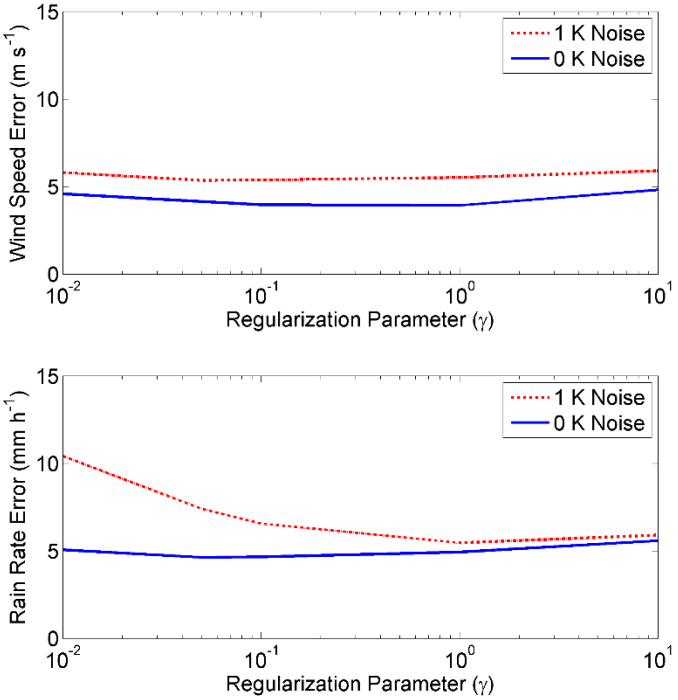

Figure 2.5: The relationship between the amount of regularization and the corresponding errors in the retrieved surface wind speed (top) and rain rate (bottom). The amount of error for each regularization amount represents an average across all simulated cases. For simulated cases with rain bands, errors were focused and averaged +/- 5° earth incidence angle around the rain bands. Errors in 1 K noise cases were averaged over 25 realizations of each simulated case for a representative idea of how random noise affects the retrieval performance at different levels of regularization.

At low values of γ, sensitivity to noise is larger and contributes a significantly greater portion of the overall error. With γ above 10^{-1}, the retrieval algorithm is over-regularized, and we lose our ability to retrieve two distinct neighboring rain bands. Figure 2.6 compares retrievals of the noise-free simulated test cases 40s and 40d, and shows why a γ of 10^{-1} was found to be the best choice for these tests. The solution that uses a γ equal to 10^{-2} has too many ringing artifacts and will be too sensitive to noise. The ringing artifacts are oscillations versus EIA

about the true value, which are caused by an under-damped inversion. The oscillations tend to increase with decreasing γ. Unfortunately, the CPM retrieval that uses a γ of 10^0 is unable to distinguish between the neighboring rain bands. A γ of 10^{-1} is a good compromise between noise sensitivity and over

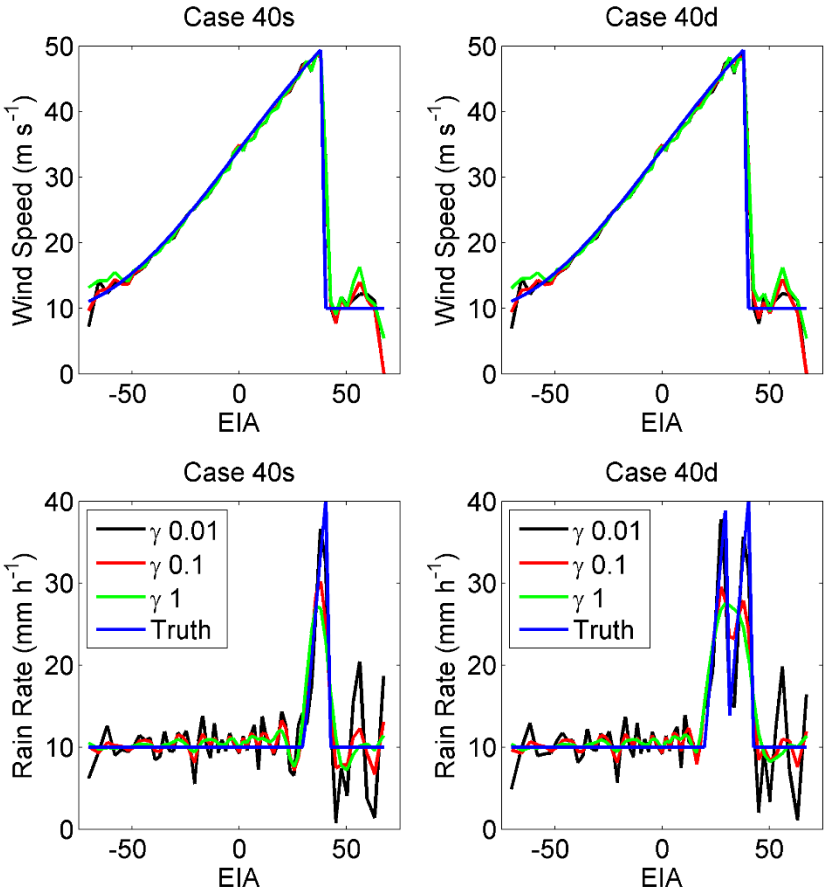

regularization, and this γ value is used for the rest of the results reported.

Figure 2.6: Comparison of noise free retrieval performance for simulated case 40s (left) and 40d (right) over a range of values. EIA is the Earth incidence angle. A γ value of 10^{-1} was chosen as a compromise value between a solution that is highly noise sensitive and a solution that cannot differentiate between two neighboring rain bands.

2.6 Results

2.6.1 Algorithm Performance for Simulated Test Cases

The CPM FRTM-based inversion algorithm with optimal regularization was applied to each of the simulated test cases to evaluate its performance. Table 2.2 gives the RMS difference (RMSD) between true and retrieved values for each retrieved parameter. For simplicity of comparison, these RMS values represent an average cross-track value for each test case. Performance was evaluated for simulated observations, with and without noise. For the observations with noise, we added random, Gaussian distributed noise with a standard deviation of 1 K. We used 25 realizations of the 1 K noise tests to estimate the errors associated with the noisy retrievals.

The performance of the constant test cases are the most sensitive to noise because we chose a regularization parameter that worked best on average for all types of HIRAD situations. Sacrificing a noise sensitive solution for the constant cases means that we are able to better resolve double rain band-type situations. The retrieval performance with the constant test cases indicates fairly poor performances in the low wind cases. This is likely due to low sensitivity of emissivity to wind speed under these conditions.

The retrieval performance in the single and double rain band cases indicates that, generally, performance degrades with a more complicated scene. Errors are generally similar between the same cross-track position cases, but performance is dependent on the position of the eyewall. This is particularly true in the double rain band case, where errors in rain rate estimates increase with increasing EIA rain band position. Performance with the more complicated scenes can be degraded by both the antenna beam averaging and the cross-track coupling.

The relationship between cross-track coupling and EIA is illustrated in Figure 2.7, which shows the correlation between errors in the wind speed and rain rate retrievals. For each test case, the correlation was calculated for each position in the swath. Figure 2.7 shows the correlation across all test cases. A negative correlation exists along the main diagonal because wind speed and rain rate

retrievals at the same EIA tend to compensate for one another in order to minimize the overall error in the retrieval. The largest negatively correlated pixels represent the pixels in the field of view that have the largest fractional contribution to the modeling of the atmosphere below the freezing level, and thus the rain rate in this field of view. Note that the negative correlation between wind speed and rain rate errors at the same EIA has the potential to introduce compensating retrieval biases (e.g. wind speed too high and rain rate too low). In practice, this possibility can be monitored by independent ground truth validation of one or the other retrieved variable – typically the wind speed. This approach motivated the refinement of the rain absorption model used by SFMR, to correct for similar negatively correlated biases found in its wind speed retrievals at high rain rates (Klotz and Uhlhorn, 2014).

Table 2.2: RMS difference (RMSD) between the true and CPM-retrieved parameters (averaged over the swath) for each test case simulation. Noise-free performance is listed under the 0 K noise columns. Noisy simulations were also tested with 25 realizations of observations with random Gaussian noise with standard deviation of 1 K added. The RMSD for 1 K noise cases is an average value from the 25 realizations.

Case ID	**RMSD**			
	Wind Speed (m s^{-1})		Rain Rate (mm h^{-1})	
	0 K Noise	1 K Noise	0 K Noise	1 K Noise
10w10r	1.7	5.3	1.3	3.8
10w40r	1.1	4.6	1.0	3.2
50w10r	0.5	1.7	0.7	3.5
50w40r	1.4	3.8	0.8	3.1
20s	2.6	4.6	2.3	5.5
30s	2.3	4.4	2.2	5.5
40s	3.2	4.7	2.5	5.5
50s	3.3	4.6	3.1	5.9
60s	2.2	3.9	2.9	6.0
20d	2.7	4.7	2.6	5.8
30d	2.4	4.1	3.0	5.7

40d	3.2	4.7	3.2	6.1
50d	3.2	4.5	4.1	6.3
60d	2.2	4.0	4.1	6.7

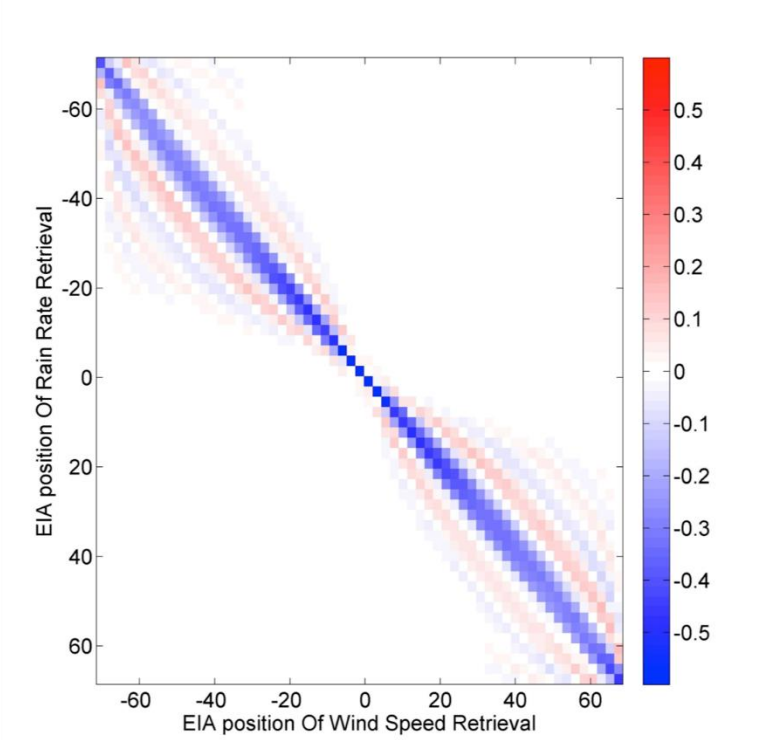

Figure 2.7: Correlation between retrieval of rain rate and surface wind speed at one cross-track position with that at all other cross-track positions, composited over all simulated cases with 1 K noise. EIA is Earth incidence angle.

Near nadir, there is much less coupling because the observing geometry at these locations is such that there is not a lot of crossover through neighboring columns of atmosphere. Farther away from nadir, there is a bit of asymmetry in the fields of view, as alluded to in Figure 2.2.b. The alternating negative and positive correlations are a consequence of the ringing artifacts that increase as the effects of cross-track coupling increase. At the edge of the swath, there is less coupling because the horizontal resolution of individual pixels increases enough to offset the larger EIAs.

2.6.2 Algorithm Performance for High Variability Wind Speed Scenes

While scenes with a double wind speed peak have not been observed with HIRAD, secondary wind maxima can occur during eyewall replacement cycles (Willoughby et al. 1982). The CPM algorithm is motivated by distinct rain bands occurring over small distances. The typical scales that motivated the development of the CPM algorithm are not typically seen for instances of secondary wind maxima. The double rain bands simulated in these performance tests were between 4 and 10 km from one another. During the eyewall replacement cycle, secondary wind maxima are seen closer to tens of km from one another (Sitkowski et al. 2011). Even though these secondary wind maxima do not occur on the spatial scales that might be a problem for HIRAD, tests were completed that show what would happen if the cross-track wind speed scene were the same as the rain rate scene simulated in the double rain band cases. An example of the double wind speed and rain band retrieval is shown in Figure 2.8. The CPM algorithm can differentiate between both the double rain bands and double wind speed peaks. RMSD values for these improbable wind speed scenes were found to be similar to the performance values of the double rain band test cases. While these scenes are improbable, the CPM model still performs well for these cases.

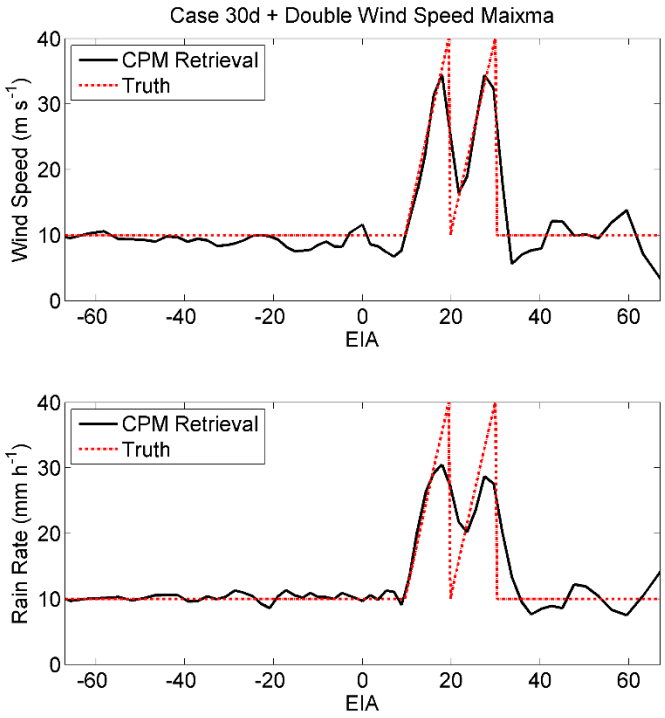

Figure 2.8: An example of wind speed (top) and rain rate (bottom) CPM retrieval performance as compared to the simulation truth for a complicated and unusual double wind speed maxima and rain band scene.

2.6.3 Hurricane Earl (2010) HIRAD Rain Rate Retrievals

The CPM FRTM-based retrieval algorithm was applied to HIRAD observations of Hurricane Earl (2010) during the GRIP airborne campaign. Figure 2.9 shows HIRAD observations (color) along with near-simultaneous measurements of 85 GHz h-pol TB by SSM/I on the F-16 satellite platform (grayscale) observed at 23:20 UTC on 01 September 2010, hereafter referred to as 85h satellite imagery. HIRAD's observations are shown in the form of excess TB (above that of a clear sky, calm ocean TB model) in order to emphasize the effects of wind speed and rain rate. The highest excess TBs are located where HIRAD passes over areas of intense rain and/or winds. Figure 2.9 shows that HIRAD tracked over the edges of the northern and western eyewalls, as well as a few of the outer rain bands.

Using the observations shown in Figure 2.9, rain rate and wind speed retrievals were performed. Figure 2.10 shows a composite of the rain rates retrieved. While there are some non-physical artifacts of calibration in this image, the CPM algorithm-retrieved rain rates match up well to the 85h satellite imagery. Both the outer and eyewall rain bands are captured at reasonable magnitudes and locations.

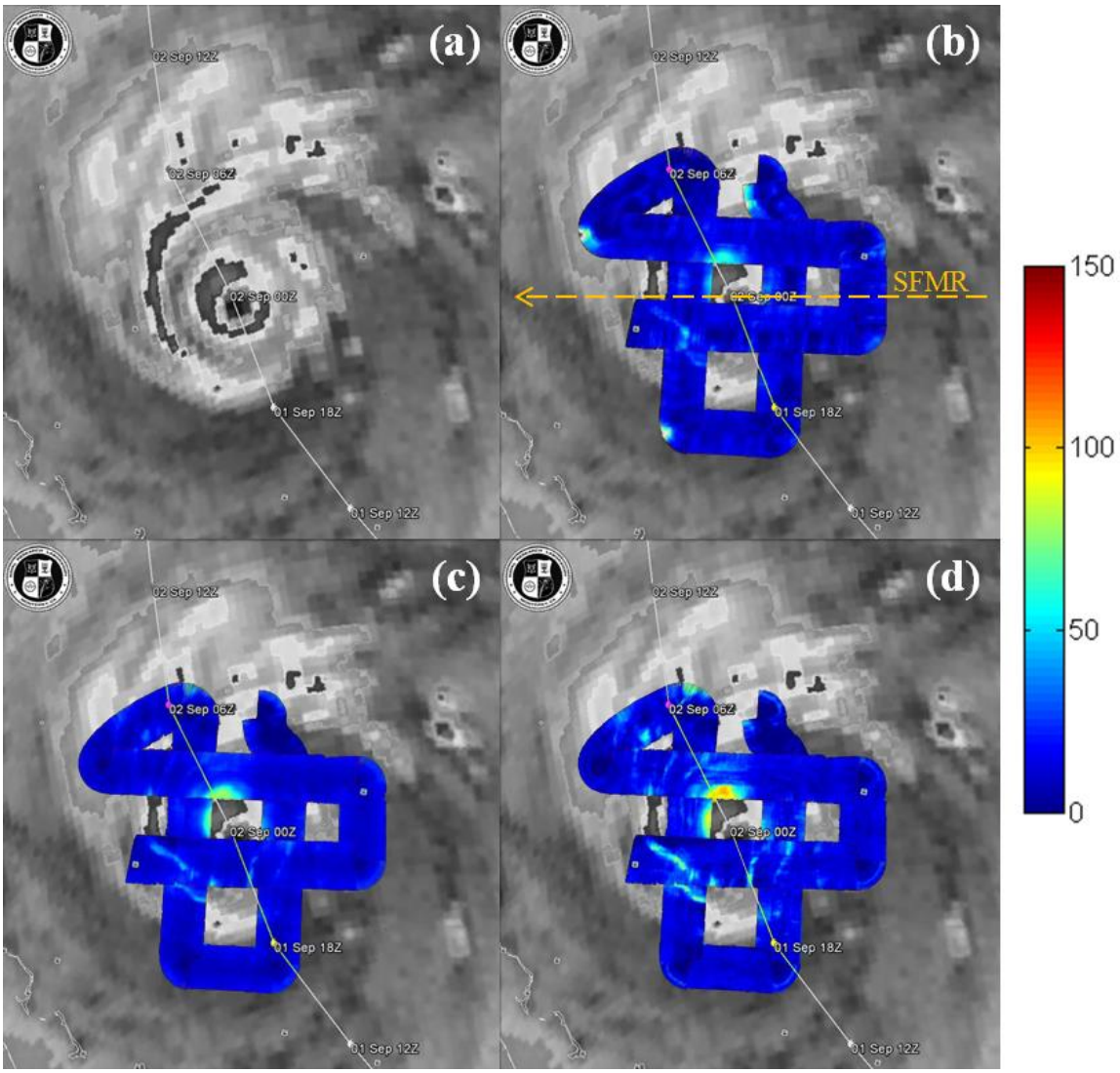

Figure 2.9: HIRAD observations of Hurricane Earl (2010) during GRIP (color) and the closest 85h satellite imagery (grayscale) from SSM/I. The satellite imagery is shown alone in Fig.2.9.a. HIRAD observations are expressed as excess TB (K), which is (HIRAD observed TB – background TB), leaving only the relationships in TB due to strong winds and rain. Figure 2.9.b shows the approximate flight track of SFMR in addition to the excess TB at 4 GHz. Figure 2.9.c shows excess TB for 5 GHz. Figure 2.9.d shows excess TB for 6.6 GHz. The satellite imagery is courtesy of the Naval Research Laboratory.

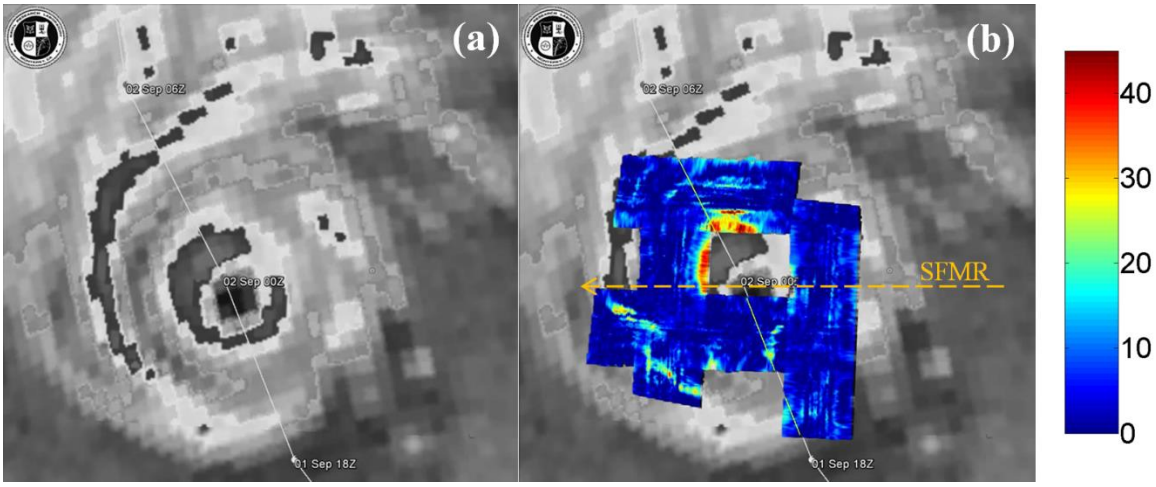

Figure 2.10: (a) 85h satellite imagery from SSM/I. This satellite imagery is courtesy of the Naval Research Laboratory. (b) A composite of HIRAD CPM rain rate retrievals (mm h^{-1}) of Hurricane Earl (2010) (color) and the closest 85h satellite imagery (grayscale) from SSM/I. The dashed arrow shows the approximate flight track of SFMR.

2.7 Discussion

2.7.1 Weighted Antenna Beam Issues

In addition to being able to differentiate between the rain and wind signatures in the observations, the CPM algorithm is also able to partially deconvolve the averaging effects of the HIRAD antenna pattern. Figure 2.3 shows why convolution is an issue in HIRAD's wide swath of observations. With increasing EIA, the antenna pattern's half power beam width (HPBW) increases. The CPM algorithm takes the beam averaging into account in the forward model, and is therefore able to retrieve a solution that is closer to the truth than the beam-weighted scene. Figure 2.11 shows this performance capability in the context of test case 30d. While beam averaging will smooth out the scene variations, the retrieved wind and rain are more representative of the true wind and rain. Most importantly, the peak wind speed is captured alongside the two neighboring rain bands. After averaging the RMSD for all noise-free, rain band cases, it was found that the CPM retrieval improves upon the beam averaged truth for rain rate by 0.3 mm h^{-1} and for wind speed by 2.3 m s^{-1}.

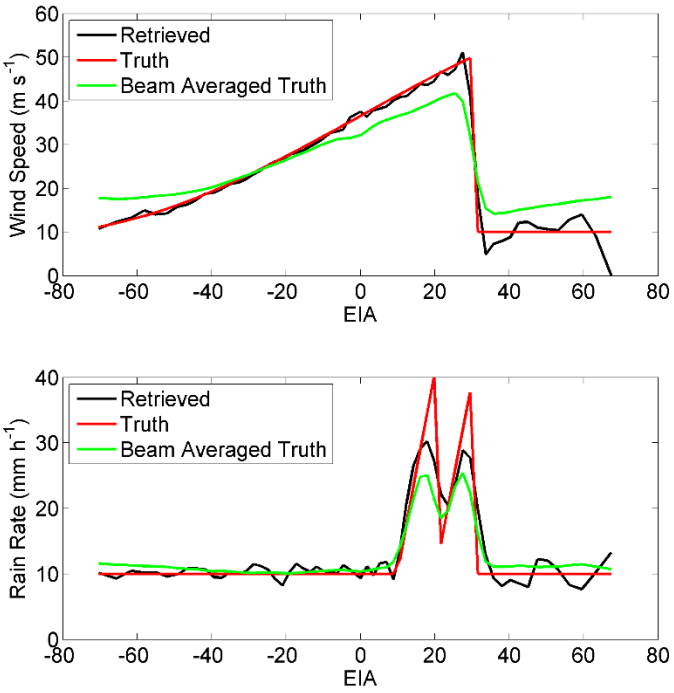

Figure 2.11: Wind speed (top) and rain rate (bottom) CPM retrieval performance as compared to the simulation truth and beam averaged truth for Case 30d.

2.7.2 Comparison of Coupled and Decoupled Performance

The advantages of the CPM algorithm become most apparent at the outer edges of HIRAD's cross-track swath. During GRIP, a similar instrument, SFMR, was flown on a NOAA P-3 at an altitude of around 3 km, with a track that allowed for nearly-co-located-with-HIRAD observations of Hurricane Earl (2010). HIRAD was flown on a WB-57 at around 20 km. Figure 2.12 shows SFMR observations from an overpass of the western eyewall that were used to compare DPM- and CPM-based HIRAD rain rate retrievals. These observations were located at nearly the same latitude and differ in time by about 15 minutes, on 02 September 2010 around 00:00 UTC.

Figure 2.12 shows that when a DPM FRTM-based retrieval algorithm is used, the algorithm is unable to resolve the two rain bands that SFMR observes in a similar location. However, the CPM retrieval is able to differentiate between these

two rain bands and successfully retrieve them. The magnitudes of CPM rain rate retrievals match up well with SFMR, and the location offset between their rain bands is likely due to slight differences in observation time and position.

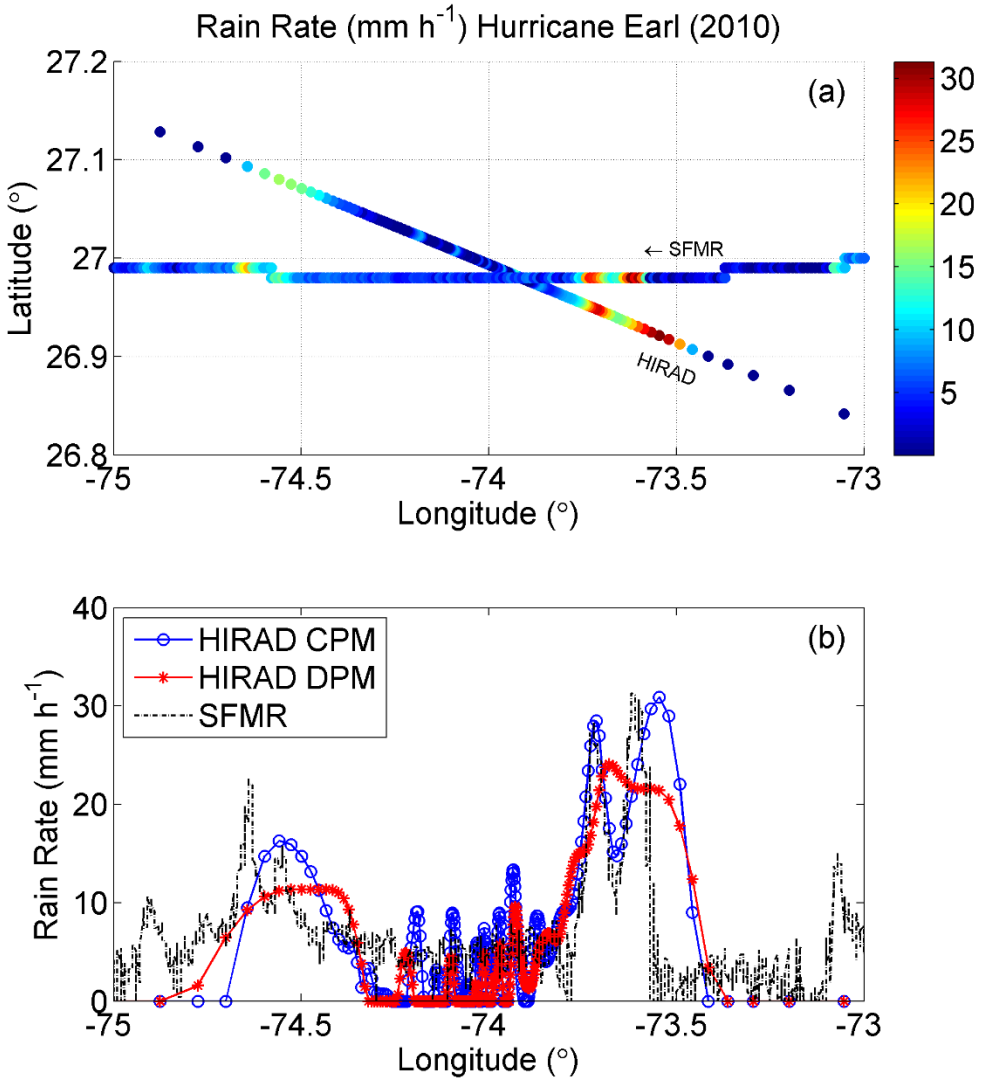

Figure 2.12: (a): SFMR and HIRAD/CPM retrieved rain rate, plotted along the latitude and longitude coordinates for reference. Flying on different aircraft, SFMR and HIRAD observations differ in time by ~15 minutes. (b): Plotted only with respect to longitude, a comparison of HIRAD rain rate retrievals (using the decoupled and coupled-pixel algorithms), as compared to nearly co-located SMFR observations of Hurricane Earl (2010).

The HIRAD absolute calibration errors are large enough that its wind speed retrievals are still problematic and are therefore not shown in Figure 2.12. Rain

rate retrievals are found to be much less sensitive to the absolute calibration issues; this results because the rain rate retrieval depends on differences between TB at different frequencies rather than on the absolute TB level. With well-calibrated observations, the wind speed can be estimated too, as has been shown by the simulations presented here.

2.7.3 Other Applications

As remote sensing technology advances, the CPM method could be valuable in spaceborne applications as well. Atmospheric phenomena exhibiting high gradients across a scene could pose retrieval challenges similar to HIRAD's challenges if the field of view cuts through a high gradient scene with high resolution. For example, narrow bands of moisture called "atmospheric rivers" (ARs) could potentially satisfy these high gradient scene requirements. ARs provide the west coast of the United States with extreme precipitation (Guan et al. 2010). High gradient scenes like this could pose challenges for advanced sensors of the future.

2.8 Conclusions

While developing a physically-based retrieval algorithm for HIRAD, we found that the simplifying assumptions commonly used in spaceborne applications and with HIRAD's heritage instrument, SFMR, were not always acceptable for HIRAD. This led to the development of a more robust method, the CPM algorithm. The CPM is different than the DPM previously used because it allows for the possibility that a single column of atmosphere can affect the observations along multiple cross-track positions. High contrast rain features, such as those that occur in an eyewall, can now be properly accounted for because there is no longer an assumption that the upwelling and downwelling atmospheric emission originate from the same atmospheric column. Using the CPM algorithm, HIRAD can differentiate between two neighboring rain bands, whereas the DPM algorithm cannot. Although the performance of this algorithm is limited by the

beamwidths at the edge of HIRAD's swath, the algorithm is also able to partially deconvolve the beam-averaged observations, getting closer to the truth.

HIRAD's observations and retrieval algorithm remain a work in progress, but strides are being made to improving its reliability. The favorable performance of the CPM has only been demonstrated thus far by the case studies presented here. Future work could include the assessment of performance in more cases as they become available with future airborne campaigns. Future work includes determining how HIRAD rain rate retrievals compare with coincident satellite observations as well as determining how sensitive the retrieval results are to freezing level height assumptions.

Appendix 2.I: Derivation of Inter-Pixel Coupling Weights in the CPM

The CPM FRTM requires individual estimates of the path-integrated optical depth along each of the upwelling and downwelling propagation paths of the measured brightness temperature at each pixel in the HIRAD wind speed image. The estimates are made using the following model for the atmosphere. Below the freezing level, a vertically uniform rain column is assumed to exist down to the surface. It is also assumed to be uniform horizontally across each surface pixel over which the wind speed is estimated. The optical depth of a rain column is assumed to scale linearly with its rain rate. The appropriate scale factor, in units of ($Np \cdot mm^{-1} \cdot h$), is given in Amarin (2010). The total, path-integrated, optical depth through the rain is found by breaking the path up into segments that pass through the rain column above each surface pixel.

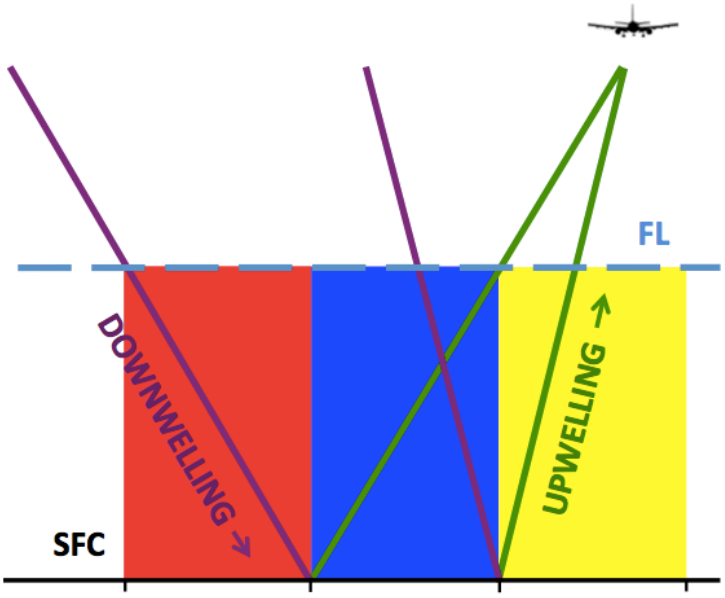

Figure 2.A1: This diagram shows a simple example, where three atmospheric columns contribute towards a single field of view, each having potentially different rain amounts, designated by the red, blue, and yellow values. The upwelling propagation path, signified by the green line, intersects through the blue and yellow columns of atmosphere. The downwelling propagation path, signified by the purple line, intersects through the red and blue columns of atmosphere. FL stands for freezing level. SFC stands for the ocean surface.

Figure 2.A1 shows an example of an observing geometry in which the propagation path passes through the rain column above three surface pixels. The number of distinct rain columns intersected will vary, depending on the subset of observations used and the EIA of the surface pixel considered, with higher EIAs crossing through more columns. Table 2.I.1 shows, as a function of EIA, the number of distinct rain columns that must be considered when computing the total path-integrated optical depth in the set up used for the simulated test cases. At nadir, it is sufficient to consider only the single rain column above the surface pixel under observation. In this case, the CPM reduces to the DPM FRTM. At high EIA values, near the swath edge, there is significant coupling between rain columns over many surface pixels on either side of the surface pixel under observation. At the outermost edge of the swath, horizontal resolution of the rain columns degrades, causing the number of pixels to decrease slightly compared to the peak amount of coupling considered in the middle-edge of the swath.

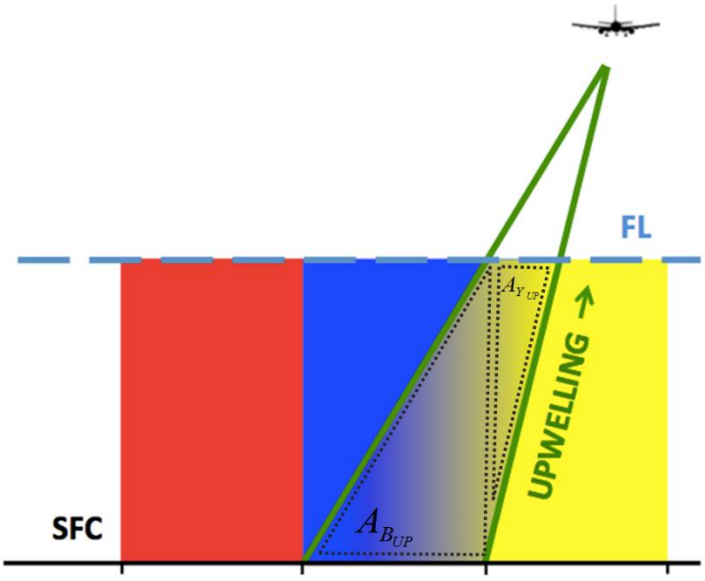

Figure 2.A2: This figure illustrates that the weighted upwelling rain rate would be a weight of the blue and yellow columns of atmosphere. $A_{Y_{UP}}$ *and* $A_{B_{UP}}$ *are labeled for reference to eqn. 2.A1.*

The total effective rain rate along a propagation path, from which the optical depth is derived, is the weighted average of the rain rates of all rain columns intersected. The appropriate weighting is found geometrically. In the example in Fig.2.A2, the rain rate integrated along the upwelling propagation path is a weighted average of the rain in the yellow and blue columns, as given by

$$R_{UP} = \frac{A_{B_{UP}} R_B + A_{Y_{UP}} R_Y}{A_{B_{UP}} + A_{Y_{UP}}} \qquad (2.A1)$$

where R_Y is the rain rate in the yellow column, R_B is the rain rate in the blue column, $A_{Y_{UP}}$ is the area of the yellow upwelling polygon below the freezing level, and $A_{B_{UP}}$ is the area of the blue upwelling polygon below the freezing level.

Similarly, the rain rate integrated along the downwelling propagation path is a weighted average of the rain in the red and blue columns shown in Fig.2.A3, or

$$R_{DN} = \frac{A_{B_{DN}} R_B + A_{R_{DN}} R_R}{A_{B_{DN}} + A_{R_{DN}}} \qquad (2.A2)$$

where R_B is the rain rate in the blue column, R_R is the rain rate in the red column, $A_{R_{DN}}$ is the area of the downwelling red polygon below the freezing level, and $A_{B_{DN}}$ is the area of the downwelling blue polygon below the freezing level.

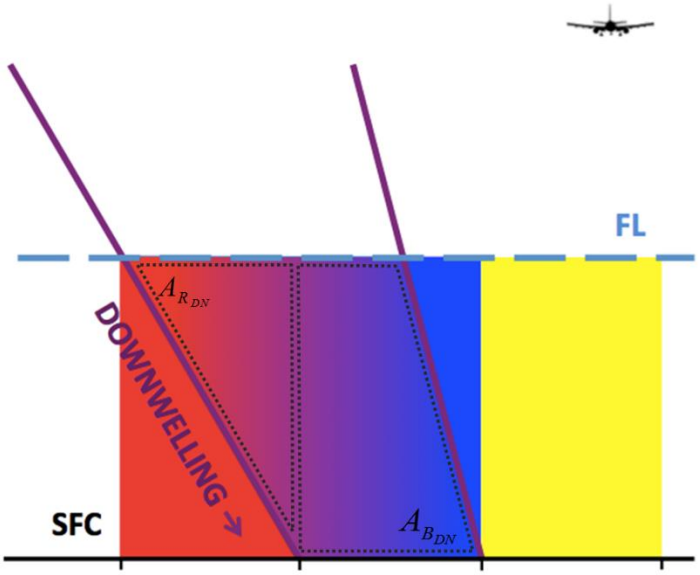

Figure 2.A3: This figure illustrates that the weighted downwelling rain rate would be a weight of the blue and red columns of atmosphere. $A_{R_{DN}}$ *and* $A_{B_{DN}}$ *are labeled for reference to eqn.2.A2.*

Once the total effective rain rate has been computed along both the upwelling and downwelling propagation paths, the corresponding optical depths can be computed. These are then used in the CPM FRTM, as explained in section 2.3.

Table 2.I.1: The number of rain pixels that are considered when calculating the effective rain rate in the field of view at Earth incidence angles (EIA) of the subset of observations used in the simulated test case set up.

EIA	Number of Rain Pixels
0	1
2	3
4	3
5	3
7	4
9	5
11	5
12	5
14	6
16	7
18	7
20	7
22	7
24	8
26	8
27	8
29	8
32	8
34	8
36	8
38	8
40	8
43	8
45	8
48	8
50	8
53	7
56	7
60	6
63	6
67	4

Chapter 3. Estimating Tropical Cyclone Integrated Kinetic Energy with the CYGNSS Satellite Constellation

3.1 Summary

The Cyclone Global Navigation Satellite System (CYGNSS) constellation is designed to provide observations of surface wind speed in and near the inner core of tropical cyclones with high temporal resolution throughout the storm's life cycle. A method is developed for estimating tropical cyclone integrated kinetic energy (IKE) using CYGNSS observations. IKE is calculated for each geographically-based quadrant out to an estimate of the 34-knot wind radius. The CYGNSS-IKE estimator is tested and its performance characterized using simulated CYGNSS observations with realistic measurement errors. CYGNSS-IKE performance improves for stronger, more organized storms and with increasing number of observations over the extent of the 34-knot radius. Known sampling information can be used for quality control. While CYGNSS-IKE is calculated for individual geographic quadrants, using a total-IKE—a sum over all quadrants—improves performance. CYGNSS-IKE should be of interest to operational and research meteorologists, insurance companies, and others interested in the destructive potential of tropical cyclones developing in data sparse regions, which will now be covered by CYGNSS.

3.2 Introduction

3.2.1 Tropical Cyclone Intensity Classifications and Complications

Tropical cyclones (TCs) are routinely categorized according to the intensity of storm winds, either as the maximum sustained one-minute or 10-minute wind speed (VMAX). Routinely used in the United States, the Saffir-Simpson Hurricane Wind Scale (SSHWS) categorizes hurricanes with the one-minute sustained VMAX (Saffir 1975; Simpson 1974). Using a single, intensity-related

input often doesn't tell the whole story of the destructive potential of a TC. Both size and intensity matter.

The deficiencies of the SSHWS as a predictor of destructive potential have been acknowledged in numerous previous studies (e.g. Mahendran 1998; Kantha 2006; Powell and Reinhold 2007; Irish et al. 2008; Maclay et al. 2008). The limitations of SSHWS are most clearly shown by a comparison between the destruction from Hurricanes Katrina (2005) and Camille (1969) (Irish et al. 2008; Powell and Reinhold 2007). Hurricane Camille, with a landfall intensity of 150 kts, maxing out the SSHWS at category 5, is now considered to be the second-most-intense hurricane in the United States' record, surpassed only by the 1953 Labor Day hurricane (Kieper et al. 2016). Hurricane Katrina made landfall in the same area, but as a category 3 storm with an intensity of 110 kts (Knabb et al. 2005). The SSHWS failed to communicate the destructive potential for Hurricane Katrina. Those that had survived the category 5 Hurricane Camille, may have thought that it would be easier to live through category 3 Hurricane Katrina. Despite being two SSHWS classifications below Hurricane Camille, Hurricane Katrina was a much larger storm than Camille at landfall, which led to a significantly more destructive storm surge (Knabb et al. 2005; Irish et al. 2008).

The comparison of hurricanes Katrina and Camille highlights the need for a TC strength scale that depends on both the intensity of the winds and the size of the storm. First proposed by Powell and Reinhold (2007), integrated kinetic energy (IKE) can be used to supplement the SSHWS. IKE is defined here as

$$IKE = \int_V \frac{1}{2} \rho U^2 dV \tag{3.1}$$

where U , the surface wind speed, is integrated over a specified volume V of the storm, taking into account the air density ρ . IKE is considered to be a better measure of the destructive potential of TCs than is SSHWS, since it quantifies both the spatial extent and the strength of the winds.

3.2.2 Previous IKE studies

Since first being introduced, several IKE-related products have been proposed. IKE is now included in the set of H*Wind products (Powell et al. 1998; 2010). H*Wind IKE can be computed from H*Wind analyses which combine all available surface wind speed observations for storms in real-time, as well as in post-storm reanalyzes. H*Wind products have been recently commercialized, and current products are no longer publically available. However, the H*Wind legacy dataset is still publically available, since it was created when these products were supported through NOAA. H*Wind products are heavily reliant on data availability—in particular, on observations collected from reconnaissance aircraft. The coverage and availability of H*Wind products is concentrated in the Atlantic and Eastern Pacific basins.

In a study by Maclay et al. (2008), low-level IKE was calculated from flight-level aircraft reconnaissance data, and an experimental, multi-satellite, IKE-based product developed from this work is now available from the NOAA/NESDIS/STAR/RAMMB real-time TC data product page (NOAA/NESDIS/STAR/RAMMB 2016). Dissimilar to the IKE product to be developed in this study, IKE is calculated over a 1 km depth and at 700 hPa using flight-level wind speed, rather than over a 1 m depth at the surface level, like all other surface wind speed-based IKE products. This difference between flight-level and surface-level IKE calculations is important to consider, if trying to compare different IKE products. Maclay et al. (2008) went to considerable lengths to then categorize the 700-hPa-IKE further by a simple 0 – 5 scale to create easier comparisons to the categorization employed by the SSHWS.

IKE-metrics like the track-IKE have been proposed as more useful analysis metrics for seasonal activity: Misra et al. (2013) followed up on this proposal. Additionally, work has been performed on the statistical predictability of IKE (Kozar and Misra, 2014; Kozar 2015; Kozar et al. 2016).

3.2.3 Existing Sensors for Surface Wind Speed Estimation

The space-borne sensors and imagery that have supported the above IKE products (Maclay et al. 2008; Powell et al. 1998; 2010) include scatterometers, infrared, visible, and water vapor imagery, and microwave sounders. Scatterometers provide surface wind speed estimates, but are limited to regions without heavy precipitation and are also known to have poor revisit time (Hennon et al. 2006). Infrared and visible imagery allow for the estimation of low-level winds by tracking cloud features (e.g., Dunion and Velden 2002; Holmlund et al. 2001; Velden et al. 1997, 2005). Generally, the feature tracking methods will not work for low-level wind estimation if the low-level features being tracked are obscured by high cloud tops, say for example, near the center of a tropical cyclone. It is also possible to estimate low-level wind parameters using infrared data, but these methods require an estimate of storm intensity (Kossin et al 2007; Knaff et al. 2015; Mueller et al. 2006). Advanced Microwave Sounding Unit (AMSU) soundings can inform estimates of the two-dimensional mid-level wind field after solving the non-linear balance equation. However, AMSU estimated winds are known to be poor near storm centers since the resolution of the product is limited, with 50 – 120 km footprints (Bessho et al. 2006). Low-level winds estimated through these methods will have to be adjusted to the surface (Knaff et al., 2011). All of these sensors have limited utility for estimating surface wind speed in the heavy-precipitation and high-cloud-shielded region of the TC eyewall. Additionally, the polar-orbiting sensors will have inadequate temporal sampling for the time-scales typical of TC rapid intensification.

3.2.4 CYGNSS

The Cyclone Global Navigation Satellite System (CYGNSS) constellation of eight small satellites, launched on 15 December 2016, will provide unique ocean surface wind speed observations in all precipitating conditions (Ruf et al. 2016). The mean and median revisit times for the constellation over the entire tropics are 7.2 h and 2.8 h, respectively. The resolution of the wind speed product will be 25 x 25 km^2 or better, with 2 m s^{-1} retrieval uncertainty for winds less than 20 m s^{-1} and 10% retrieval uncertainty for winds greater than 20 m s^{-1}. Given the ability

to penetrate through the high precipitation of a TC eyewall to observe the highest surface wind speeds of TCs, and the rapid temporal sampling, CYGNSS is well suited to estimate IKE.

There are some challenges to overcome with this new observing system. Since CYGNSS operates in a bi-static radar type set up with GNSS transmitters, the sampling patterns are not analogous to the continuous-swath observations typical of other space-borne wind sensing instruments. Instead, CYGNSS observes winds along a series of narrow tracks through the storm. Portions of the wind field between the tracks are not directly sampled and must be estimated as part of the IKE algorithm discussed in this chapter. It should be noted that there are currently no plans for near-real-time ground processing of CYGNSS data. In the future, if the CYGNSS mission successfully demonstrates the value of its data products, a transition to near-real time operations is possible and the IKE data product could be available to operational agencies.

3.2.5 Objectives and Overview

The main objectives of this study are to develop and characterize a CYGNSS-based IKE product for tropical storms and cyclones (CYGNSS-IKE). Section 3.3 describes the data sets used. Section 3.4 presents the CYGNSS-IKE algorithm concept and implementation. The subsequent sections address the characterization of the algorithm in three respects:

1) How well does CYGNSS-IKE perform?

2) How well can the confidence in CYGNSS-IKE be determined from CYGNSS data alone?

3) What are the dominant error contributors to CYGNSS-IKE?

3.3 Datasets

In order to test the CYGNSS-IKE algorithm pre-launch, a large set of simulated observations was created using the CYGNSS end-to-end-simulator (E2ES) (O'Brien, 2014). The E2ES generates simulated CYGNSS level 2 wind speed data products from a time evolving input wind field. It properly accounts for both the spatial and temporal peculiarities of the CYGNSS measurement technique by forward propagating the orbital trajectories of every satellite in the GPS and CYGNSS constellations and computing the location of the specular reflection point on the Earth surface as a function of time for every possible GPS/CYGNSS pair. The E2ES also properly accounts for the 25 km spatial resolution of the CYGNSS wind speed measurements by appropriately averaging the input wind field and for its measurement uncertainty by corrupting the input "truth" winds with noise that is statistically representative of the expected precision of the level 2 wind speed retrieval algorithm (Clarizia and Ruf, 2016).

Simulated CYGNSS observations were generated using real-time wind field analyses produced by the operational version of the Hurricane Weather Research and Forecasting (HWRF) system (Tallapragada et al., 2013) for most Atlantic and West Pacific storms during the 2010 and 2011 hurricane seasons. HWRF wind fields were generated for 25 different storms every 3 hours throughout their life cycles. Times during which the storm center, provided by the best-track database (Landsea et al. 2013), was within 200 km of a major land mass were excluded from this study. This resulted in a total of 201 3-hour intervals in which CYGNSS observations were simulated from the HWRF "truth" wind fields. An example of an HWRF input wind field for one of these 3-hour periods, together with the simulated observations by CYGNSS that would have been made over that interval of time, within 200 km of the storm center, is shown in Figure 3.1, A summary of all of the storms used in this study is given in Table 3.1.

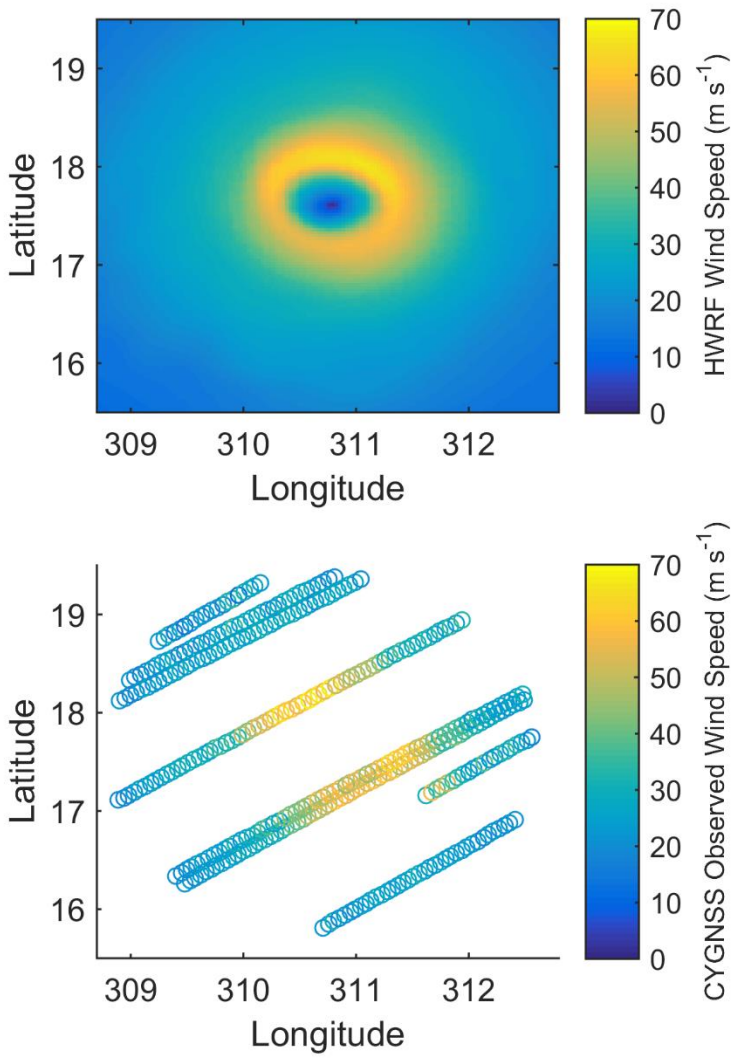

Figure 3.1: (Top) An example of an HWRF wind analysis for Hurricane Igor, 1200 UTC, 13 September 2010. (Bottom) Simulated CYGNSS observations that correspond to the HWRF wind analysis, within 200 km of the storm center, for the time period 1200 UTC – 1500 UTC, 13 September 2010.

Table 3.1: A summary of all of the storms used in this study, with the storm name, the number of cases for that particular storm, the maximum wind speed (V_{MAX}) of the cases considered, the storm center latitude and longitude of the storm at the point in time corresponding to the V_{MAX} case, and the year for each storm.

Storm Name	Number of Storm Test Cases	V_{MAX} (m s^{-1})	Storm Center Latitude (deg N)	Storm Center Longitude (deg E)	Storm Test Case Year
Colin	7	27	27.4	293.0	2010
Danielle	13	54	26.8	300.3	2010
Earl	5	23	15.0	324.8	2010
Estelle	8	27	17.3	250.8	2010
Fiona	4	29	24.3	293.8	2010
Frank	2	40	17.6	250.6	2010
Gaston	8	16	17.4	304.5	2010
Igor	18	66	17.6	310.7	2010
Julia	11	59	17.7	327.8	2010
Matthew	1	20	14.0	282.3	2010
Ten	1	24	19.8	250.4	2010
Adrian	10	63	14.5	254.7	2011
Bret	3	24	29.8	284.0	2011
Calvin	3	36	16.7	250.9	2011
Dora	2	41	19.4	250.6	2011
Eugene	18	61	15.7	245.3	2011
Fernanda	14	28	14.6	217.3	2011
Gert	5	26	32.9	297.3	2011
Greg	9	36	18.5	248.6	2011
Hilary	13	59	17.1	250.6	2011
Irwin	2	22	15.2	240.9	2011
Katia	19	55	27.0	294.1	2011
Maria	6	33	33.7	293.1	2011
Ophelia	8	50	24.0	296.9	2011
Philippe	11	25	14.9	326.4	2011

3.4 Methodology

Determination of the IKE requires that the integral expression in eqn. (3.1) be evaluated. This, in turn, requires that the wind speed be known (or estimated) at every location within the vicinity of the storm bounded by the limits of integration. In the case of CYGNSS, actual measurements of the wind occur along a series of narrow tracks through the storm, as illustrated in Figure 3.1. Values of the wind

speed in between the actual observations, which are needed to compute the IKE, are estimated by fitting a parametric model of the wind structure to the observations and then using the model to interpolate between the observations.

In order to create an operationally relevant IKE product, IKE is integrated over each geographically-based quadrant out to the 34-knot wind radius (R_{34}). The operational community uses R_{34} because this refers to the extent of the tropical storm strength winds. If a storm is weaker than 34-kts, the R_{34} threshold is not attained, and IKE is not estimated. For the case of the true IKE, R_{34} is found directly from the fully sampled HWRF wind field that is integrated to get the IKE. For the case of the IKE retrieved from CYGNSS observations, R_{34} is estimated iteratively using a parametric wind model. This parametric 34-knot wind radius is denoted as $R_{34.P}$. The CYGNSS-IKE algorithm has two inputs: 1) the CYGNSS level-2 surface wind speed observations collected over a three hour time period within a specified radius of the storm center; and 2) the storm center location.

The interpolation of the wind field to points between those measured by CYGNSS takes advantage of the approximately symmetrical nature of hurricanes by using the parametric wind model based on Emanuel and Rotunno (2011)

$$V(r) = \frac{2r\left(R_{m.p}V_{m.p} + \frac{1}{2}fR_{m.p}^{\ 2}\right)}{R_{m.p}^{\ 2} + r^2} - \frac{fr}{2} \qquad (3.2)$$

where $R_{m.p}$ is the radius of maximum winds, $V_{m.p}$ is the maximum wind speed, r is the radial distance from the storm center, and f is the Coriolis parameter. The Coriolis parameter is dependent on the storm center location coordinates. The model is illustrated in Figure 3.2.

While there are many options of parametric wind model that could be used, the one chosen has been found to be especially amenable to use when fitting in a least-squares sense to the CYGNSS samples, because it is continuous and has an analytical derivative. Our choice was informed by the study performed by Lin and Chavas (2012), where they tested four gradient wind profiles in storm

surge modeling applications (Holland 1980; Jelesnianski et al., 1992; Emanuel 2004; Emanuel and Rotunno 2011). Lin and Chavas (2012) finds that the Emanuel and Rotunno (2011) model performs better in storm surge applications compared to the other parametric wind models tested. The use of other commonly used models (i.e. Willoughby et al. 2006) is a subject for future study.

There are some limitations to using eqn. (3.2), as discussed extensively in (Chavas et al. 2015): particularly, this model is most applicable to the region inwards of around 2.5 times the radius of maximum wind speed. Outside this inner region, the level of error is storm-type dependent, as quantified in Chavas et al. (2015).The simplicity of this model far outweighs the limitations.

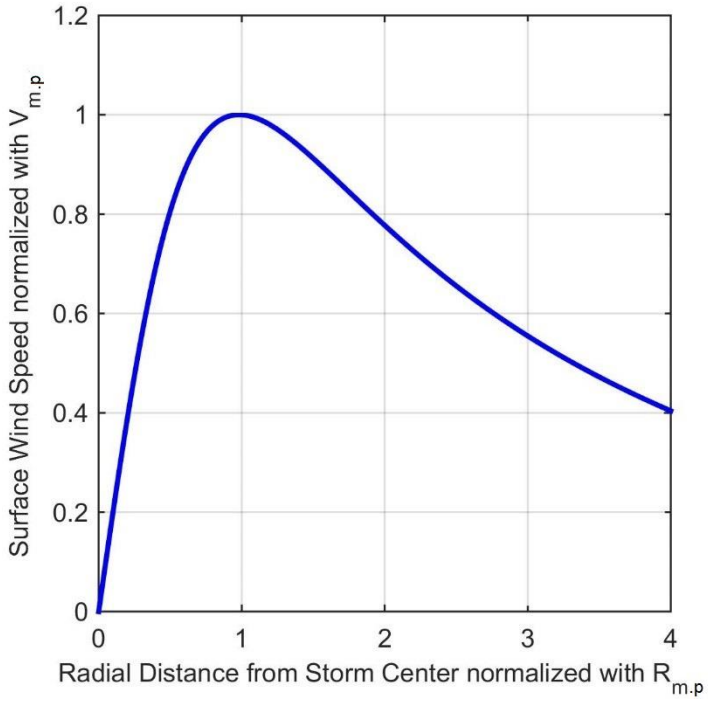

Figure 3.2: A visualization of the parametric wind profile embedded within the CYGNSS-IKE algorithm. This model is described by eqn. (3.2), based on the work of Emanuel (2011) and recommended by Lin and Chavas (2012).

The CYGNSS-IKE algorithm flow is illustrated in Figure 3.3. The two free parameters of the model, $R_{m.p}$ and $V_{m.p}$, are solved for using an iterative, least-squares fit of the model to the CYGNSS observations. An example of the cost function to be minimized is shown in Figure 3.4 as a function of $R_{m.p}$ and $V_{m.p}$. The error surface is free of inflection points and the cost function has a single

global minimum at the optimum ($R_{m.p}$,$V_{m.p}$) value. Such a well-behaved error surface makes the iterative algorithm relatively insensitive to the first guess (which only effects the number of iterations required before convergence) and means a global minimum is generally found in each case.

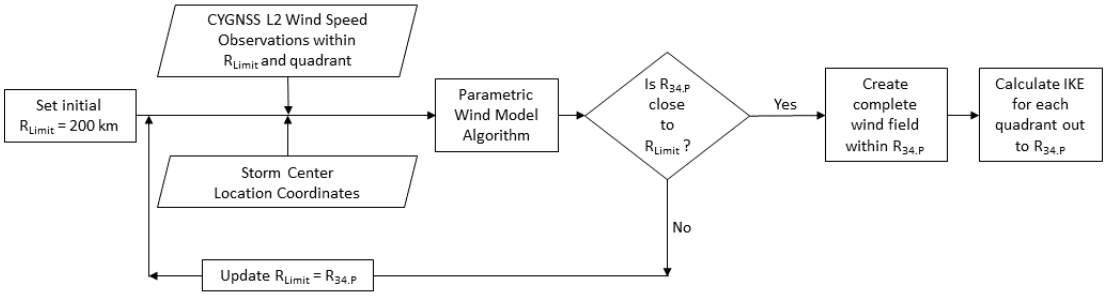

Figure 3.3: A flow chart describing the steps within the CYGNSS-IKE algorithm.

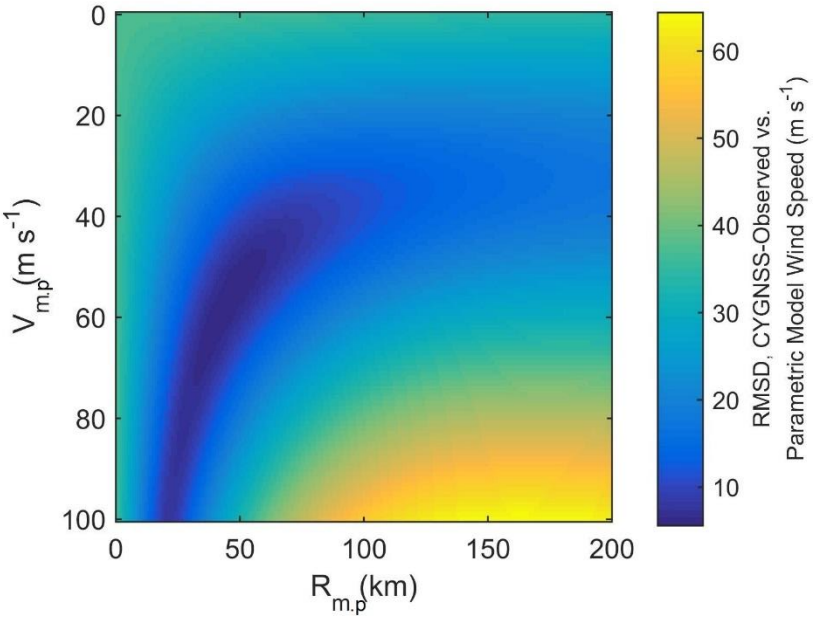

Figure 3.4: An example of the cost function to be minimized, RMSD, is shown as a function of the parametric model free-variables, $R_{m.p}$ and $V_{m.p}$ from eqn. (3.2), for Test Case: Hurricane Igor, 1200 UTC, 13 September 2010. For further reference and connection, Figure 3.1 shows the HWRF wind field and

corresponding CYGNSS observations that were input into the CYGNSS-IKE estimation process for this test case.

The population of CYGNSS observations which are used in the parametric fit is all those samples lying within a distance R_{Limit} of the storm center. R_{Limit} is initially set to 200 km. After the first iteration, the estimate of R_{34} given the parametric model, $R_{34.P}$, is compared to R_{Limit}. If they are not sufficiently close, then R_{Limit} is set equal to $R_{34.P}$, a new population of observations is selected, and the processes is repeated. Eventually (in practice within just a few iterations), the values of $R_{34.P}$ and R_{Limit} converge and the parametric model estimation is complete.

The IKE is calculated from the parametric wind model by

$$IKE = \frac{\rho_0 \Delta z}{2} \int_0^{2\pi} \int_0^{R} v(\theta, r)^2 \, r \, dr \, d\theta \qquad (3.3)$$

where v is given by eqn. (3.2) and r is the radial distance from the storm center. The integration extends out to R = $R_{34.P}$, with an assumed Δz of 1 m, and a constant density ρ_0 of 1.15 kg m^{-3}—as suggested by Holland (1980).

3.5 Results

3.5.1 CYGNSS-IKE Performance

The performance of the CYGNSS-IKE estimates is assessed by comparison to the true IKE derived by direct integration of the high resolution HWRF wind fields. All 201 cases are considered. A portion of the 201 cases serve as test cases, but do not meet the strength or observation criteria to compute IKE at the R_{34} threshold. There are two scenarios for which IKE is not estimated in a particular quadrant: 1) the quadrant was not observed by CYGNSS, or 2) CYGNSS did not observe winds which would have supported an estimate of R_{34} from the parametric model fit. For example, if the quadrant wind field is well sampled by CYGNSS, but most of the wind speed estimates are lower than 34-knots, the parametric model trained to the observations will not predict, or support, winds

over 34-knots. The performance statistics reported here are for comparisons when both HWRF and CYGNSS-based estimates of R_{34} IKE are possible. For the rest of the chapter, unless otherwise noted, IKE refers to a quadrant specific calculation of IKE.

First, as an example, Figure 3.5 demonstrates IKE estimates possible over the course of the lifetime of one storm. Figure 3.5 shows the CYGNSS-$IKE_{R34.P}$ and HWRF-IKE_{R34} values every 3 hours throughout the life cycle of Hurricane Igor (2010) for instances of available simulated CYGNSS observations for all four storm quadrants. In general, the CYGNSS-IKE agrees closely with the HWRF-IKE. However, Figure 3.5 also highlights two main limitations of the current CYGNSS-IKE estimation process. At elapsed time 50 h, CYGNSS-IKE is not estimated for the NW and NE quadrants, while it was estimated from HWRF. In this case, CYGNSS did not have sufficient observations to support an estimate of R_{34} strength in the parametric model. Weaker case points sometimes miss the $R_{34.P}$ threshold—a requirement for IKE to be calculated in these methods—if they are not sampled sufficiently. A sufficient number of observations is required in a quadrant in order to accurately represent the wind field and support the parametric model estimator. An example of the effects of sample size on performance can be seen in Figure 3.5 in the SE quadrant at 253 h, where CYGNSS-IKE is much less than HWRF-IKE. Outliers like this will be flagged based on CYGNSS coverage over a particular storm.

Figure 3.6 shows the overall performance of the CYGNSS-IKE estimate compared with HWRF-IKE. CYGNSS-IKE is estimated 412 times out of all 201 storm test cases. The two colors signify the quality control (QC) applied. Red dots indicate that the QC flag, developed in the following section, has been flagged for that estimate.

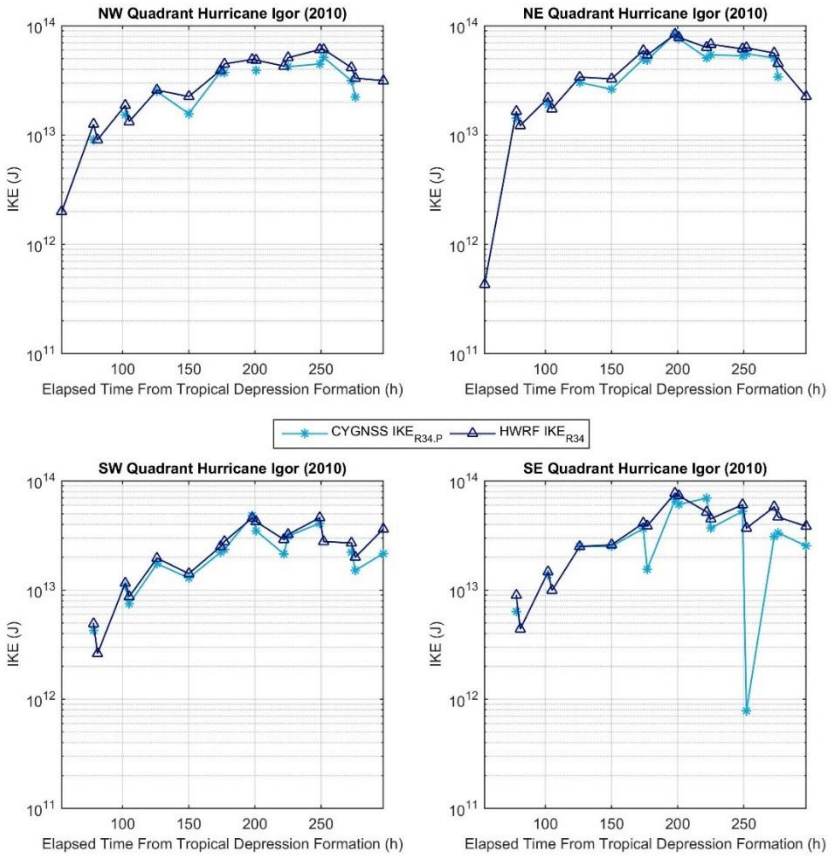

Figure 3.5: A comparison of the IKE estimated from HWRF wind fields (truth) and simulated CYGNSS observations (retrieved) over the life cycle of Hurricane Igor (2010) as a function of the elapsed time since tropical depression formation at 0600 UTC 8 September 2010 (Pasch and Kimberlain 2011). For further reference and connection, Figure 3.1 shows the HWRF wind field and corresponding CYGNSS observations that were initially input into the CYGNSS-IKE estimation process at elapsed time 126 hours.

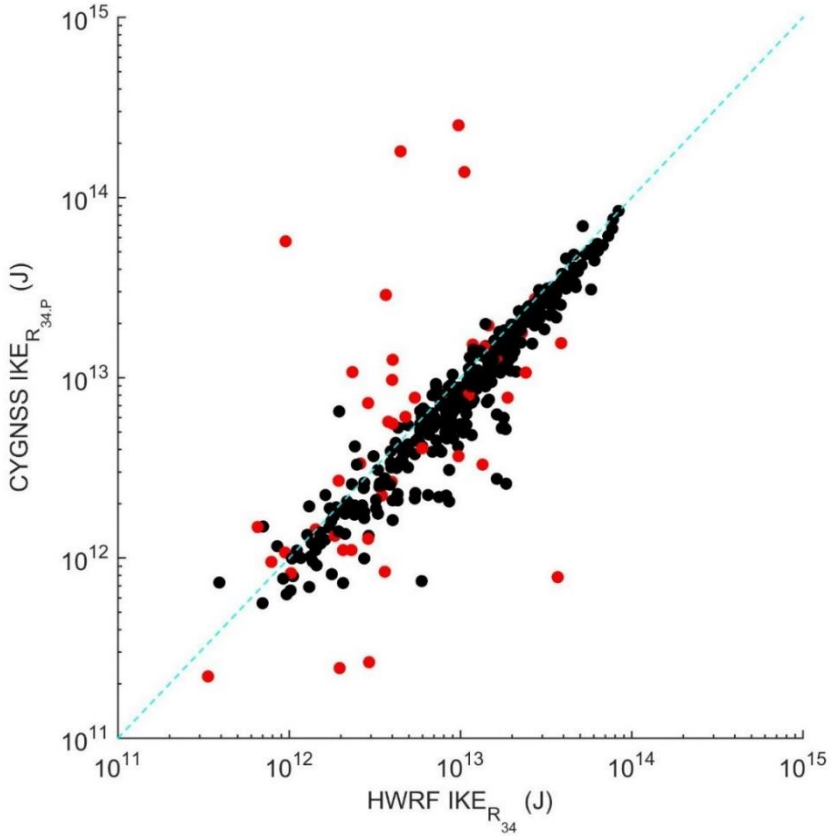

Figure 3.6: A comparison of CYGNSS-IKE with the IKE estimated from HWRF for test cases defined from a set of simulated CYGNSS observations of Atlantic and Pacific-basin storms occurring during 2010 – 2011. Out of 201 storm test cases, IKE is estimated for a particular quadrant 412 times. Red dots denote cases where Q/C is flagged.

3.5.2 Quality Control Threshold Determination

In order to create estimates of IKE product trustworthiness, additional analysis was performed to create a QC flag for the CYGNSS-IKE estimate. Ideally, a QC flag would throw out as many outliers as possible, while still retaining the cases with good performance. Instinctively, one would expect sampling coverage by CYGNSS to control the quality of the IKE estimate. A number of sampling thresholds were tested in combination to determine a practical CYGNSS-IKE QC flag. Figure 3.7 supports the decision making process for the ultimate QC flag choice. In the top subplot of Figure 3.7, the IKE error is plotted with respect to two types of QC flags which are used in combination. IKE error is here defined as the normalized RMS difference, with normalization of the difference between

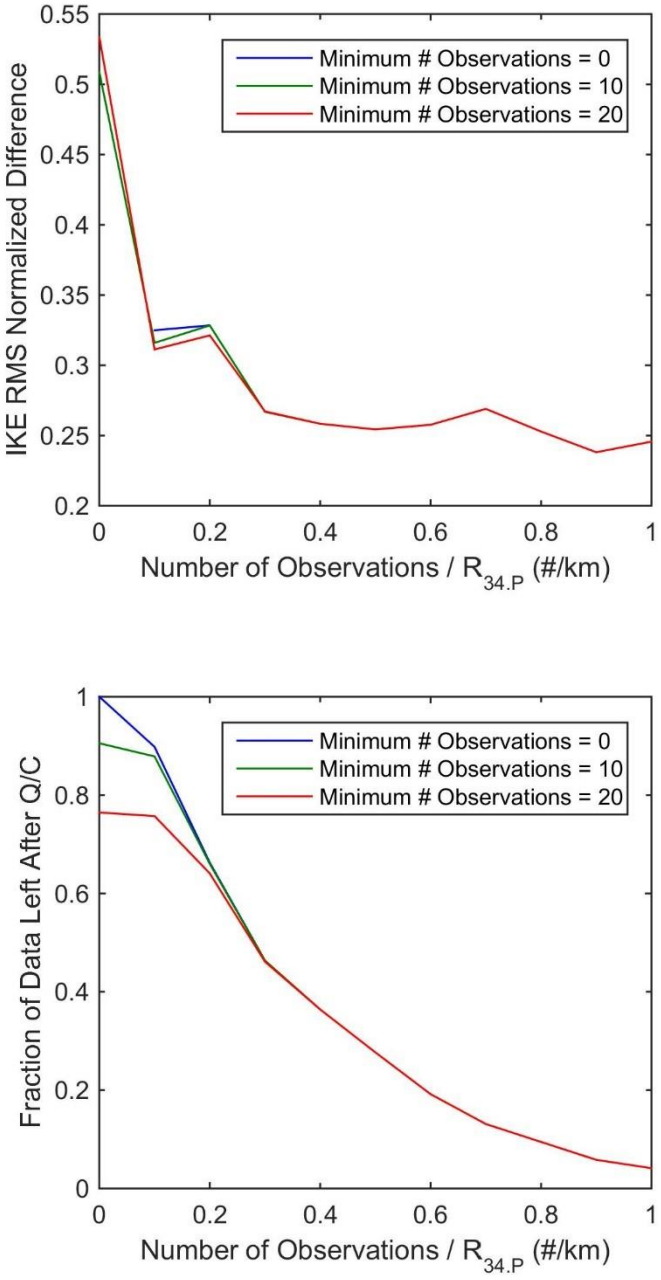

Figure 3.7: Top: IKE RMS normalized difference between HWRF-IKE and CYGNSS-IKE with respect to two Q/C flags operated in combination. Each line represents the minimum number of observations allowed for a test case. Each line is plotted against a second Q/C flag, which controls for the ratio of the number of observations per the 34-kt wind radius in the parametric model ($R_{34.P}$). Bottom: Fraction of data left for all combinations of Q/C applied. The Q/C choice of more than 10 samples and more than 0.1 samples/km leaves 88% of the test cases.

HWRF and CYGNSS-IKE by the HWRF-IKE being performed before the root mean square calculation.

To pass the QC test requires that

$$num_{obs} > N \tag{3.4}$$

where num_{obs} is the number of observations over a storm quadrant and N is the minimum number of observations allowed, and that

$$ratio_s > S \tag{3.5}$$

where $ratio_s$ is the sampling ratio defined as

$$ratio_s = \frac{num_{obs}}{R_{34.P}} \tag{3.6}$$

in units of number per km. S is the minimum sampling ratio required. On the Figure 3.7 x-axis, is $ratio_s$: larger $ratio_s$ correlates with better sampling over the extent of 34-kt winds. Each line in Figure 3.7 shows the QC defined by eqn.(3.4), which only controls for the minimum number of observations needed for IKE estimation. Operated in combination, eqn.s (3.4)-(3.5) allow us to discard cases with poor sampling by CYGNSS. In general, the higher the threshold, the lower the error in the CYGNSS estimate. However, as noted in the bottom subplot of Figure 3.7, the threshold also affects data coverage (i.e. fraction of remaining storm quadrant overpasses for which an IKE estimate is produced). The choice for the threshold should be an appropriate balance between data coverage and performance. We propose a QC flag that requires N = 10 observations and S = 0.1 observations per km; this threshold operates just above the “knee in the curve” with respect to performance and provides 88% data coverage.

The results of applying the chosen QC can be seen in Figure 3.6, where red dots denote cases where the flag is applied. Black dots show the cases which

would remain post-QC. The chosen QC flag gets rid of most of the outliers without a large loss of good cases.

3.5.3 Error Decomposition

There are four main sources of error in the CYGNSS-IKE estimation. The first source results from the use of a parametric wind model which is not representative of the true wind speed distribution. Second, CYGNSS sampling varies between 3-hour intervals, with poorer coverage generally leading to worse estimates of IKE. Third, the CYGNSS wind speed measurements are not noise-free, and the retrieval uncertainty will contribute to errors in the CYGNSS-IKE estimate. Fourth, imperfect knowledge of R_{34} will impact the performance of the algorithm, since $R_{34.P}$ determines the population of observations used and defines the outer limit of integration of the IKE.

In order to compare the impact of these sources of errors, four experiments were run, each with a different type of wind speed input to the algorithm. The first experiment assumes gap-free sampling of the wind field at the high resolution HWRF reporting intervals. The samples are also assumed to be exact, with no CYGNSS measurement error. The parametric wind model is fit to these observations and then used to estimate IKE. Errors in the estimated IKE in this case will be due only to deviations of the true wind field from the parametric wind model.

The second experiment also assumes observations of the wind field without any CYGNSS measurement error, but now only at the locations at which CYGNSS would have sampled. In this case, errors in the estimated IKE will be due to both deviations from the ideal wind model and gaps in the wind observations. The third experiment is most realistic and assumes CYGNSS observations with realistic noise levels and at their appropriate sample locations. The fourth experiment is similar to experiment three, but we assume perfect knowledge of R_{34}, which is calculated from HWRF for this analysis. Differences between the IKE calculated from these experiments and the HWRF-IKE allows

for comparisons of the dominant error contributors to the CYGNSS-IKE estimation process.

Table 3.2 reports the results of these experiments. Overall, the CYGNSS-IKE performance is quite good, with 6.5% total unexplained variance due to all causes. The table also compares the percent unexplained variance that can be attributed to the individual sources of error. There is an increase in unexplained variance as the experiments include sparser and noisier wind fields. However, imperfect knowledge of R_{34} also impacts the performance of this estimation process. With perfect knowledge of R_{34}, the unexplained variance using true CYGNSS observations decreases from 6.5% to 3.9%, which is closest to the performance from the first, perfectly sampled, and noise-free experiment.

Table 3.2: Percent unexplained variance for experiments which used different input wind fields into the CYGNSS-IKE algorithm, where percent unexplained variance is $(1 - R^2) \times 100\%$.

Experiment Input Winds	Percent Unexplained Variance
HWRF Wind Field	4.3%
Noise-free CYGNSS Wind Speed Observations	4.8%
Noisy CYGNSS Wind Speed Observations	6.5%
Noisy CYGNSS Wind Speed Observations with perfect $R_{Limit} = R_{34}$	3.9%

3.5.4 Storm Center Sensitivity

Since one of the inputs to the IKE algorithm is an estimate of the storm center location—which, for this study, is provided by the best-track database (Landsea et al. 2013)—additional tests were performed to determine the sensitivity of the CYGNSS-IKE estimate to the accuracy of the storm center location. It is well known that the storm center is challenging to define for poorly organized storms. To test storm center location sensitivity, the coordinates were varied from the HWRF best estimate to locations +/- 0.5 degrees in latitude. The CYGNSS observations were then re-assembled according to the new (erroneous) storm

center location. The results, averaged over north and south perturbations, from the storm center position experiments are shown in Figure 3.8. CYGNSS-IKE was found to be essentially insensitive to errors in storm center latitude within about 15 km north and south of the best estimate of storm center location. Outside of this range, the estimated IKE begins to degrade in accuracy. Center position uncertainty estimates vary widely depending on the strength of the storm, as well as the data available for position estimation (Torn and Snyder 2012; Landsea and Franklin 2013). For example, Torn and Synder (2012) estimated position uncertainty to be around 37-65 km. While position uncertainty estimates from these studies are usually larger than 15-km, the authors hypothesize that the availability of CYGNSS data could be used to improve position estimates.

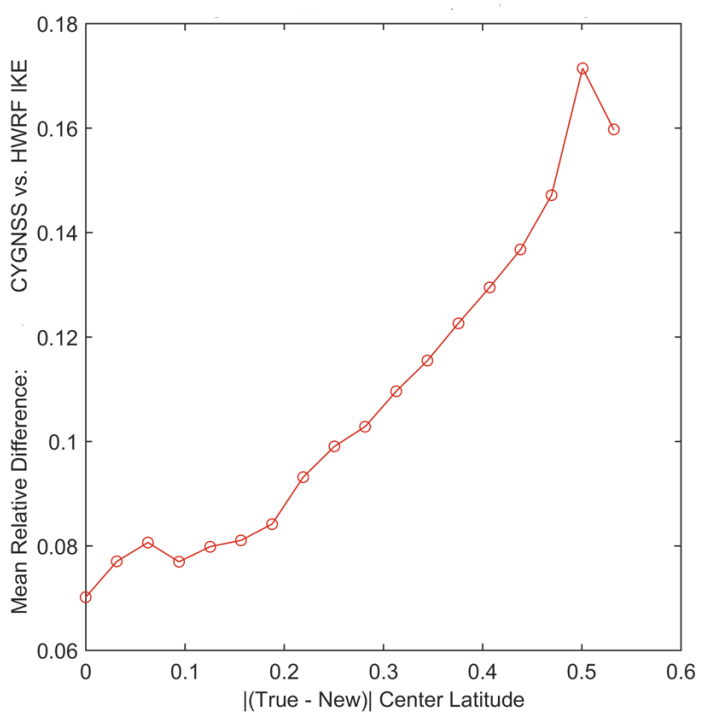

Figure 3.8: The average relative difference in CYGNSS and HWRF derived IKE estimates for experiments where the given storm center location was perturbed degrees north and south of its original location, shown along the x-axis.

3.6 Discussion

Generally, the CYGNSS-IKE estimate is skillful. Performance depends most on the number of CYGNSS observations available for a given IKE estimate, which led to the formulation of a useful quality control flag. A CYGNSS-IKE estimate is generally more reliable as the number of samples increases. If a quality control flag is applied which limits estimates to cases with a minimum of 10 CYGNSS observations and a 0.1 sampling ratio, 88% of the coverage remains, the performance metrics improve, and the dominant source of IKE retrieval error is no longer the number of CYGNSS observations.

Other parameters were considered for use as a quality control parameter, but nothing else gave as much skill as the sample number flag. One potential parameter considered was the RMSD between the retrieved parametric wind model and the CYGNSS observations. However, the RMSD was found to be well correlated with the number of CYGNSS samples. With fewer samples, the RMSD of the parametric wind model fit tends to go down since it is generally easier to fit a model to fewer points. Thus, a low RMSD in this case does not mean the parametric wind model explains the wind field better, and so does not predict a better IKE estimate. An accurate IKE estimate requires the wind field to be well sampled, not that the RSMD in the parametric model be low.

Generally, the CYGNSS-IKE estimate performs better in intense storms because the parametric wind model is more applicable in these cases—stronger storms tend to be better organized and hence correspond more closely to the parametric model. Figure 3.9 and Figure 3.10 summarize the relationship between relative IKE error and maximum wind speed (V_{MAX}). Figure 3.9 compares data for quadrant IKE, while Figure 3.10 shows the results from total (sum over all quadrants) IKE. In Figure 3.10, only cases where estimates of IKE were available for all four quadrants are considered. Figure 3.9 shows that the large outliers in quadrant-IKE performance occur more often in cases with low V_{MAX}; many of the low intensity outliers result from large overestimates of the IKE. Aside from the outliers at low V_{MAX}, CYGNSS-IKE performs relatively

consistently across the range of intensity. Figure 3.10 shows the results if considering total IKE over the entire storm. Performance improves for these cases compared to the results in Figure 3.9. Improvements from quadrant-IKE to total-IKE are likely due to two main things. First, comparisons of total-IKE are only made for cases where all four quadrants have IKE estimates; these cases are strong and are well sampled, the latter likely playing a larger role. Second, quadrant-IKE errors will partially cancel out after summation.

Overall, Figure 3.9Figure 3.10 show there is a low bias in the CYGNSS-IKE, whether or not it is a total or quadrant specific value. The bias in CYGNSS-IKE is likely due to the fact that we are training the parametric model to the CYGNSS observations in a best-fit sense in order to estimate the full wind field. CYGNSS-IKE is calculated out to the radial extent of the 34-kt winds in the parametric model, rather than the true extent. Since the model is fit to all of the wind speed data, and not just the highest magnitude data, a bias is introduced. It is also possible that the parametric model used is not always representative of the distribution of wind speed. Future work will include analyzing this bias further on a wider range of cases, as well as determining solutions to correct it.

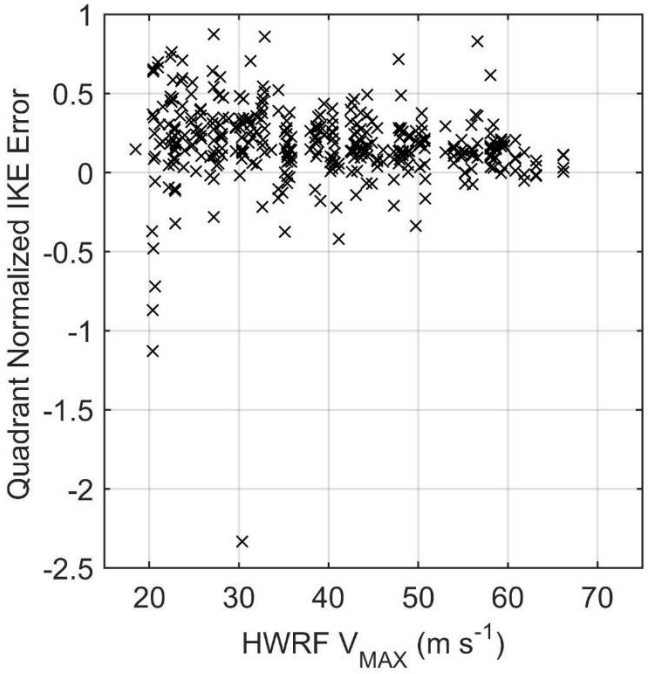

Figure 3.9: The relative, quadrant specific, IKE error of cases post-QC, with respect to the maximum wind speed found in the HWRF wind field. Quadrant Normalized IKE Error = (truth – estimated)/truth where the truth here is derived from HWRF.

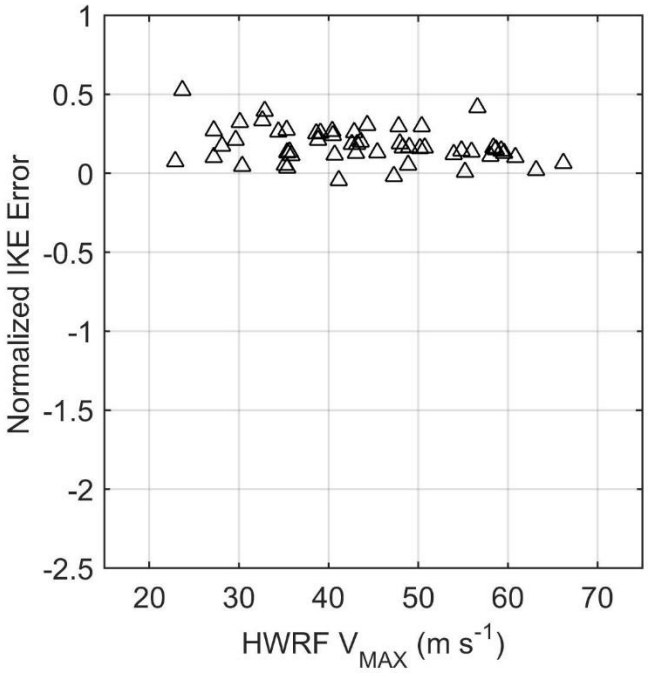

Figure 3.10: The relative IKE error of cases post-QC, with respect to the maximum wind speed found in the HWRF wind field. Normalized IKE Error = (truth – estimated)/truth where the truth here is derived from HWRF. IKE is summed over all quadrants for cases where there were estimates of IKE for all quadrants available.

3.7 Conclusions

CYGNSS will provide the opportunity to observe tropical cyclones (TCs) with unprecedented temporal and spatial sampling. With this new observing system comes challenges and questions to be explored. In this chapter we consider how well IKE can be estimated from its observations.

With applications ranging from storm surge prediction to situational awareness, users of the CYGNSS-IKE product could include operational and research meteorologists, insurance companies, and anyone interested in TCs generated in data-sparse, but CYGNSS covered, regions. IKE is particularly useful considering it is often more correlated with storm surge at TC landfall than is the V_{MAX} or intensity of the storm.

There are a number of areas of future work. First, the way in which CYGNSS observations and the parametric model are combined to produce a complete wind field has to be optimized. As IKE is not yet widely used, another area of future work includes determining the accuracy requirements needed for science applications. Additional sensitivity analysis using a larger variety of test cases, as well as on-orbit data, is ongoing. Finally, determining the applicability and usefulness of a CYGNSS-based storm center position corrector to this product and others is another area of future work.

Chapter 4. Determining Tropical Cyclone Surface Wind Speed Structure and Intensity with the CYGNSS Satellite Constellation

4.1 Summary

The Cyclone Global Navigation Satellite System—CYGNSS—consists of a constellation of eight microsatellites which will provide observations of surface wind speed in all precipitating conditions. A method for estimating tropical cyclone (TC) metrics—maximum surface wind speed (V_{MAX}), radius of maximum surface wind speed (R_{MAX}), and wind radii (R_{64}, R_{50}, R_{34})—from CYGNSS observations is developed and tested based on simulated CYGNSS observations with realistic measurement errors. Using two inputs, 1) CYGNSS observations and 2) the storm center location, estimates of TC metrics are possible through the use of a parametric wind model algorithm which effectively interpolates between the available observations as a constraint on the assumed wind speed distribution. This methodology has promising performance based on the simulations presented. Future work will include calibration and validation of the algorithm once real CYGNSS data are available. In particular, after quality control filters based on sampling properties are applied to our population of test cases, the standard deviation of retrieval error for V_{MAX} is 4.3 m s^{-1}, for R_{MAX} is 17.4 km, for R_{64} is 16.8 km, for R_{50} is 21.6 km, and for R_{34} is 41.3 km.

4.2. Introduction

4.2.1 Motivation

Tropical cyclones (TCs) and their precursor storms spend most—if not all—of their lifetime over the ocean, which makes them harder to observe in situ. Since the advent of remote sensing, fewer TCs go unobserved, and our increased observation of these storms has led to improved understanding of TC processes.

Additionally, the observations that are collected through remote sensing support the TC situational awareness and forecasting efforts at warning centers like the National Hurricane Center (NHC) (Rappaport et al. 2009).

Forecasters are required to estimate the present and predict the future intensity of TCs, typically defined as the maximum 1- or 10-minute sustained wind speed at the 10-m observing level associated with the system (Harper et al. 2010; Office of the Federal Coordinator for Meteorological Services and Supporting Research 2012). Only 30% of the 6-hourly intensity estimates in the North Atlantic (Rappaport et al. 2009) are guided by aircraft reconnaissance, and next to no aircraft reconnaissance is performed elsewhere. Unfortunately, intensity estimation is challenging without aircraft reconnaissance. Intensity estimates in the post-season reanalysis records have uncertainties of approximately 5 m s^{-1} (Landsea and Franklin 2013; Torn and Synder 2012). Often, the observational guidance that TC forecasters use is based entirely on remote sensing observations.

Observations of surface wind speed can inform estimates of the intensity of a system. In addition to intensity estimation, surface wind speed observations can also guide forecasters who are analyzing the extent of 34-, 50-, and 64- kt surface winds out from the center of a storm—commonly collectively referred to as wind radii. Wind radii give insight into the surface wind structure and therefore are useful for a variety of applications (Knaff 2016).

4.2.2 Examples of Previous Efforts

Satellite remote sensing-based methods have been developed to estimate intensity in situations where aircraft reconnaissance is not available. One of these methods is the Dvorak technique: a method of estimating TC intensity through subjective image pattern recognition. The Dvorak technique was first developed based on visible-sensors onboard geostationary meteorological satellites (Dvorak 1975). Since the initial method was published, refinements and advancements have been made to the Dvorak technique (Velden et al. 1998;

Velden et al. 2006). Infrared imagery is now included in the guidance (Dvorak 1984) and an automated version, called the Advanced Dvorak Technique (ADT) is a part of the suite of satellite-based guidance available to TC forecasters (Olander and Velden 2007). One disadvantage of the Dvorak technique is that it is an indirect and sometimes a subjective approach. However, since the Dvorak technique relies on geostationary satellites, it is not plagued by data gaps typically seen if relying on polar-orbiting satellites or aircraft reconnaissance alone.

Due to the usefulness of geostationary data availability, a variety of other methods for TC characterization—both intensity and wind structure estimation—have been developed for geostationary infrared imagery and data (e.g. Mueller et al. 2006; Kossin et al 2007; Piñeros et al. 2008, 2011; Fetanat et al. 2013; Knaff et al. 2015; Dolling et al. 2016). A number of studies have developed methods which need an estimate of storm intensity in order to estimate wind structure from infrared data (Mueller et al. 2006; Kossin et al 2007; Knaff et al. 2011, 2015). The deviation angle variance (DAV) technique developed by Piñeros et al. (2008, 2011) correlates intensity and structure with the gradient in infrared brightness temperature; the DAV-based wind radii methods presented in Dolling et al. (2016) use a multiple linear regression technique. Fetanat et al. (2013) take advantage of historical hurricane satellite data (HURSAT) to estimate intensity from feature analogs—or brightness temperature patterns—in satellite imagery and analogous storms. In addition to infrared data inputs, the methods developed in Knaff et al. (2011, 2015) take advantage of multiple satellite inputs to estimate the TC wind field, from which wind radii are estimated.

TC intensity estimation is also possible using passive microwave sounders, like AMSU. This method takes advantage of the correlation between a TC's warm core structure and its intensity. Warm-core anomalies are greatest during peak intensity. Using the retrieved vertical temperature structure from AMSU, estimates of the minimum surface level pressure and maximum sustained wind speed are possible through the hydrostatic approximation and assumptions of

gradient wind balance (Kidder et al. 2000). Care has to be taken to account for the effect of clouds and precipitation on the AMSU radiances. While AMSU does not have adequate horizontal resolution to estimate realistic wind structure alone, estimates of the 34-, 50-, and 64-kt wind radii and maximum wind speed can be made using statistically-based algorithms (Bessho et al. 2006; Demuth et al. 2006). The performance from this microwave-sounder-type method is comparable to the Dvorak technique, but since this method relies on polar-orbiting sounders, sampling of the TC inner core is limited.

Knaff et al. (2016) developed methods for estimating wind radii using routinely available estimates of TC intensity, motion, and location. These inputs, together with estimates of TC size from IR imagery or model analyses, are used to create a modified Rankine vortex from which wind radii are estimated.

Observations from the Soil Moisture Active Passive mission (SMAP) (Fore et al. 2016) are useful for TC applications because the low frequency observations are uncontaminated by rain. However, the spatial resolution, 65-km, requires additional scaling if intensity is to be estimated from SMAP ocean vector winds. Yueh et al. (2016) developed SMAP-based TC intensity estimation methods after relating the V_{MAX} observed by the SMAP platform to the true V_{MAX}. Unfortunately, as a polar-orbiting satellite, the revisit time for SMAP is poor.

4.2.3 CYGNSS

The Cyclone Global Navigation Satellite System (CYGNSS) constellation of eight small satellites will provide unique ocean surface wind speed observations in all precipitating conditions (Ruf et al. 2016). The retrieval uncertainty is anticipated to be 2 m s^{-1} for winds less than 20 m s^{-1} and 10% for winds greater than 20 m s^{-1}. Like SMAP, CYGNSS operates at a sufficiently low frequency to see through the high precipitation of a TC eyewall and observe the highest surface wind speeds of TCs. Unlike SMAP, CYGNSS observations will be 25 x 25 km^2. Its temporal sampling is also significantly more frequent. Using a constellation of

eight satellites in low-inclination circular orbit allows for mean and median revisit times over the tropics of 7.2 h and 2.8 h, respectively.

While CYGNSS observations will be useful for estimating TC intensity and wind structure, there are some challenges to overcome with this new observing system. The sampling patterns are not analogous to the continuous-swath observations typical of other space-borne wind sensing instruments (e.g. SMAP). CYGNSS observes winds along a series of narrow tracks through the storm; portions of the wind field between observations tracks are not directly sampled. If for example, a CYGNSS-based intensity estimation method involved simply finding the highest wind speed observed by CYGNSS through a storm, the intensity estimate might not have good performance if the gaps in sampling happened to coincide with the location of maximum winds.

If the CYGNSS mission successfully demonstrates the value of its data products, a transition to near-real time operations is possible in the future, and the data products developed here could be available to operational agencies. However, it should be noted that there are currently no plans for real-time data processing.

4.2.4 Outline

The capabilities of CYGNSS have wide applicability to TC science and forecasting activities. In this chapter, CYGNSS-based methods are developed for the estimation of a variety of metrics commonly used to describe TCs: V_{MAX} (intensity), R_{MAX} (the radius of maximum winds), and wind radii (R_{34} or 34-kt wind radius; R_{50} or 50-kt wind radius; R_{64} or 64-kt wind radius). Section 4.3 describes the datasets used to develop and evaluate the method. Section 4.4 describes the algorithm. Sections 4.5 and 4.6 characterize the performance of the CYGNSS-based estimates of intensity and wind structure and develop quality control measures of its reliability. Section 4.7 discusses these results. Section 4.8 offers some conclusions and opportunities for future investigations.

4.3 Datasets

A large set of realistic simulated observations was created using the CYGNSS end-to-end-simulator (E2ES) (O'Brien, 2014) in order to develop and test the CYGNSS-IKE algorithm prior to launch. The E2ES generates simulated CYGNSS level-2 wind speed data products from a time evolving input wind field. It properly accounts for both the spatial and temporal peculiarities of the CYGNSS measurement technique by forward propagating the orbital trajectories of every satellite in the GPS and CYGNSS constellations and computing the location of the specular reflection point on the Earth surface as a function of time for every possible GPS/CYGNSS pair. Additionally, the E2ES properly accounts for the 25 km spatial resolution of the CYGNSS wind speed measurements by appropriately averaging the input wind field and it accounts for its measurement uncertainty by corrupting the input "truth" winds with noise that is statistically representative of the expected precision of the level-2 wind speed retrieval algorithm (Clarizia and Ruf, 2016).

Simulated CYGNSS observations were generated using real-time wind field analyses produced by the operational version of the Hurricane Weather Research and Forecasting (HWRF) system (Tallapragada et al., 2013) for Atlantic and Pacific storms during 2010, 2011, 2013, and 2014. HWRF wind fields were generated for storms every 3 hours throughout their life cycles; from each 3-hour snapshot from HWRF, CYGNSS observations were simulated.

After the simulation data were created, a number of quality control (QC) metrics were applied in order to get the best population of test cases to effectively test the methods presented in this paper. For each test case, there had to be no land in the smallest HWRF domain, a maximum wind speed of at least 17.49 m s^{-1} was required, and the center position—provided by the best-track databases (Chu et al. 2002; Landsea et al. 2013)—had to be within 1 degree latitude and longitude of the center of the smallest HWRF domain. These thresholds were applied to make sure the storms would be strong enough to test

for the 34-kt radius, as well as to make sure reasonably well behaved test cases were used for development.

Performance of the algorithm is characterized using comparisons with ground truth values derived from the HWRF data. True V_{MAX} is defined as the maximum surface wind speed in the smallest HWRF domain. True R_{MAX} is determined from the average location of the winds falling above the 95 percentile in the smallest HWRF domain. The true wind radii are determined from the extent of certain strengths (34-, 50-, and 64-kt) of wind speed within the smallest HWRF domain. In addition to the previously mentioned QC, cases for which the true R_{34} was located at the edge of the smallest HWRF domain were also excluded. After all QC filters are applied, a total of 302 test cases remain for developing and testing the algorithm in this study; details of each case are given in Table 4.I.1. A wide variety of storms are included. There are 113 cases from the Atlantic and Eastern Pacific. There are 189 cases from the Western Pacific. The mean R_{34} across all cases is 248 km, with a standard deviation of 99 km. The highest intensity (74 m s-1) test cases are found in the Lekima (2013) and Vongfong (2014) storms.

4.4 Methodology

4.4.1 Parametric Wind Model

CYGNSS wind speed observation tracks often have large gaps between them—gaps which may be in areas of interest (e.g. the location of the maximum wind speed). In order to account for the areas that have been missed by CYGNSS, a method is developed which effectively interpolates between the available observations using a parametric model as a constraint on the assumed wind speed distribution.

The parametric wind model used has roots in the method developed in Emanuel and Rotunno (2011) and was used in a previous study by Morris and Ruf (2016a). In Emanuel and Rotunno (2011), the parametric wind profile most

applicable to the region inside of approximately 2.5 times the radius of maximum winds is given by

$$V(r) = \frac{2r\left(R_{m.p}V_{m.p} + \frac{1}{2}fR_{m.p}^{\ 2}\right)}{R_{m.p}^{\ 2} + r^2} - \frac{fr}{2} \qquad (4.1)$$

where $R_{m.p}$ is the radius of maximum winds, $V_{m.p}$ is the maximum wind speed, r is the radial distance from the storm center, and f is the Coriolis parameter. The Coriolis parameter is determined by the storm center location coordinates and is not an independent parameter to be estimated from the CYGNSS observations.

As discussed in Chavas et al. (2015) the outer wind radii tend to be underestimated by eqn. (4.1). In order to address this tendency, two additional parameters have been added to the model to regulate the rate of decay of the wind speed at large radii. The model is given by

$$V(r) = \frac{2r\left(R_{m.p}V_{m.p} + \frac{1}{2}fR_{m.p}^{\ 2}\right)}{R_{m.p}^{\ 2} + ar^b} - \frac{fr}{2} \qquad (4.2)$$

where the two additional parameters are a and b Examples of the wind speed radial dependence specified by eqn.(4.2) are shown in Figure 4.1.

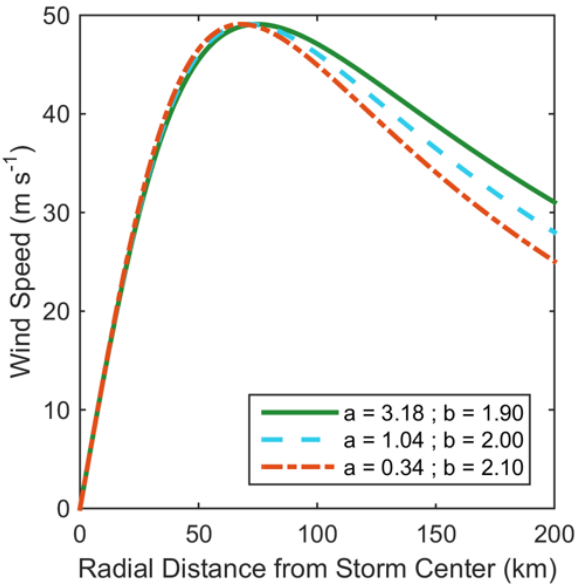

Figure 4.1: An example of the wind speed relationship from the parametric model in eqn.(4.2) with three different 'b' parameters used. $V_{m.p}$ = 50 m s^{-1}. $R_{m.p}$ = 75 km, and the center position latitude is 15° .

Of the four model parameters— $R_{m.p}$, $V_{m.p}$, a , and b —a can be solved for from the other three by requiring that the maximum value of $V(r)$ equals the parameter $V_{m.p}$. This effectively reduces eqn.(4.2) to a three parameter model. As shown in Figure 4.1, the b parameter allows for adjustment of the radial decay rate of the wind speed in the outer storm region speed. Larger values of b correspond to a faster radial roll-off. The model is fit to the CYGNSS wind speed data by adjusting the three parameters, $R_{m.p}$, $V_{m.p}$, and b , to minimize the sum squared difference between the model and all CYGNSS observations within a specified region near the storm center.

4.4.2 Parametric Retrieval Algorithm

A flow diagram of the parametric model retrieval algorithm is shown in Figure 4.2. First, depending on the basin in question, an initial R_{Limit}—the maximum radial distance from the storm center over which to draw an initial set of CYGNSS observations from—is set. For the Atlantic and Eastern Pacific storms, the initial R_{Limit} = 200 km. For the Western Pacific storms, the initial R_{Limit} = 300 km, as these storms are generally larger. The algorithm requires two sets of inputs: 1) CYGNSS observations; and 2) the center position of the storm. For the wind radii estimates, which are quadrant dependent, only observations within a particular quadrant are used; if no observations are available in that quadrant, wind radii are not estimated there. The estimates of V_{MAX} and R_{MAX} are not quadrant dependent so all available observations are used.

Once the initial set of CYGNSS wind speed data is gathered, it is input into the parametric wind model algorithm. In this algorithm, the free-parameters $R_{m.p}$, $V_{m.p}$, and b are solved using an iterative least-squares estimator. These

estimates are used to create a best-fit parametric wind model to the available observations. An example of this process is shown in Figure 4.3. In Figure 4.3a, the HWRF wind field from which the CYGNSS observations are derived is shown. In Figure 4.3b, the simulated CYGNSS observations are shown for this test case. In Figure 4.3c, an example of the final best-fit parametric wind model over all quadrants is shown. The model effectively interpolates between the gaps in the track which are shown in Figure 4.3b. The parametric model is used to derive V_{MAX} and R_{MAX}.

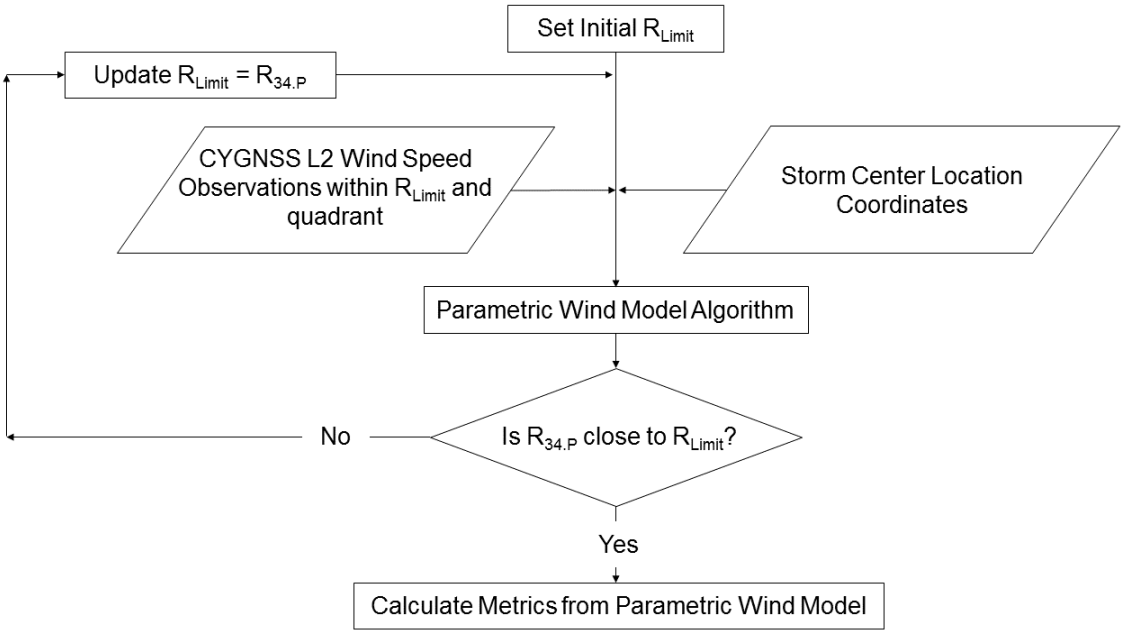

Figure 4.2: A flow diagram which outlines the steps of the CYGNSS tropical cyclone surface wind speed structure and intensity product algorithms.

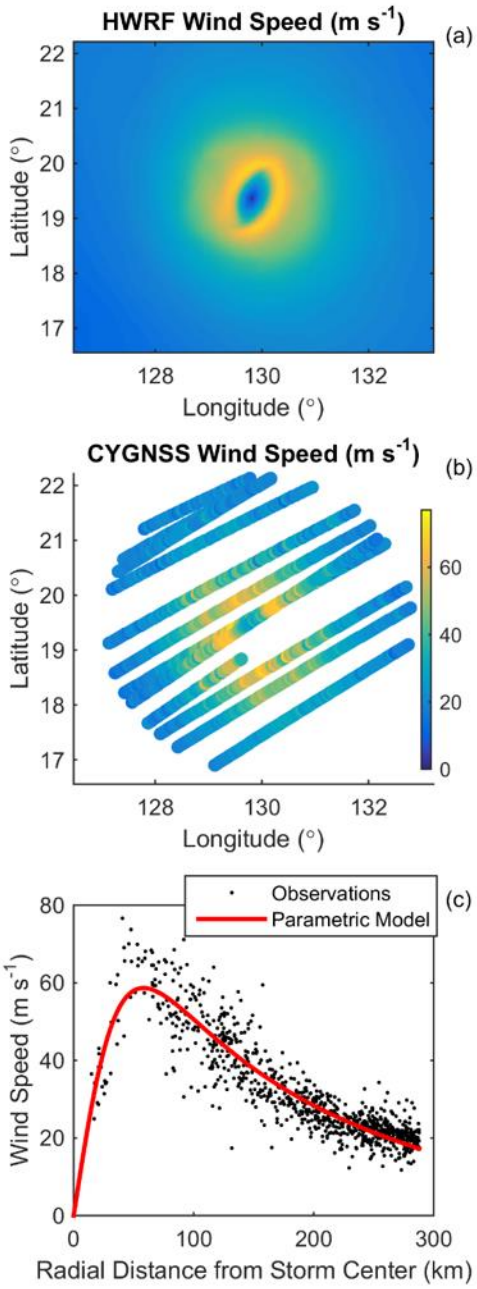

Figure 4.3: (a) HWRF wind speed field for Vongfong on 09 October 2014, 03:00 UTC; (b) Simulated CYGNSS wind speed observations for (a); and (c) the parametric model algorithm fit for this test case.

Figure 4.3c also highlights another aspect of the algorithm flow shown in Figure 4.2. Initially, observations within 300 km of the storm center are used. However, after the initial run of the algorithm, if the estimate of $R_{34,P}$ (the parametric model

estimate of R_{34}) is different than 300 km, then the algorithm is repeated until R_{Limit} and $R_{34.P}$ converge. In the test case shown in Figure 4.3, fewer observations are used in the final iteration of the algorithm because the final value of R_{Limit} after convergence is less than 300 km.

Once the best fit parametric model solution is attained, the metrics of interest can be derived from it. The parametric V_{MAX} is defined as the maximum of v(r) and the parametric R_{MAX} is defined as that r where the parametric V_{MAX} occurs. The parametric wind radii are defined by the radius at the wind strength in question in the parametric model.

4.4.3 Three- versus Two-parameter Model Impacts

In Figure 4.4 the parametric model algorithm process is examined for a particular NE quadrant test case. In this example, however, the results from using the two-parameter model given by eqn. (4.1) are shown in addition to those from using the three-parameter model (eqn.(4.2)). In this test case, the simulated CYGNSS observations suggest that the roll-off in wind speed is slower than the original two-parameter model would fit. The estimates of the outer wind radii are improved by use of a model with a more flexible roll off rate.

4.4.4 Parametric Scaling

Estimates of the intensity, radius of maximum wind, and wind radii derived directly from the parametric model function, V(r), are found to have characteristic scale and bias difference from the actual values. This is true whether the parametric model is derived only from CYGNSS observations or is fit to the complete grid of HWRF wind samples. Since the model is fit to all of the wind speed data, and not just the highest magnitude data, a bias is introduced. These scale and bias differences are compensated for by scaling the values derived directly from the parametric model using a simple power series correction. Scaling factors also help alleviate parametric model inaccuracies, as the model is

not always able to capture the inner and outer wind fields accurately. The coefficients in the power series are determined as follows: Best fit parametric models are determined for all storm cases using the complete grid of HWRF wind samples. In each case, estimates of the intensity ($V_{\max.p}$), radius of maximum wind ($R_{\max.p}$), and wind radii ($R_{34.p}$, $R_{50.p}$, $R_{64.p}$) are derived directly from the parametric model and compared to the true values determined from the actual HWRF winds. A power series is fit to the comparison which translates the direct parametric values to scaled values that are closest, in a least squares sense, to the true values. A simple linear scaling was found to be sufficient for the intensity and all three wind radii, and a third order power series was found to be necessary for the radius of maximum wind. The scaling relationships have the form

$$V_{\max.scaled-p} = a_0 + a_1 V_{\max.p} \qquad (4.3.a)$$

$$R_{\max.scaled-p} = a_0 + a_1 R_{\max.p} + a_2 R_{\max.p}^{\ 2} + a_3 R_{\max.p}^{\ 3} \qquad (4.3.b)$$

$$R_{34.\max.scaled-p} = a_0 + a_1 R_{34.p} \qquad (4.3.c)$$

$$R_{50.\max.scaled-p} = a_0 + a_1 R_{50.p} \qquad (4.3.d)$$

$$R_{64.\max.scaled-p} = a_0 + a_1 R_{64.p} \qquad (4.3.e)$$

The coefficients used in this study are given in Table 4.1. In summary, TC metrics are first derived directly from the best fit parametric model. Those metrics are then corrected using eqns. (4.3.a-e) and the coefficients in Table 4.1 to estimate the TC metrics. These final metrics will henceforth be referred to as the scaled-parametric metrics.

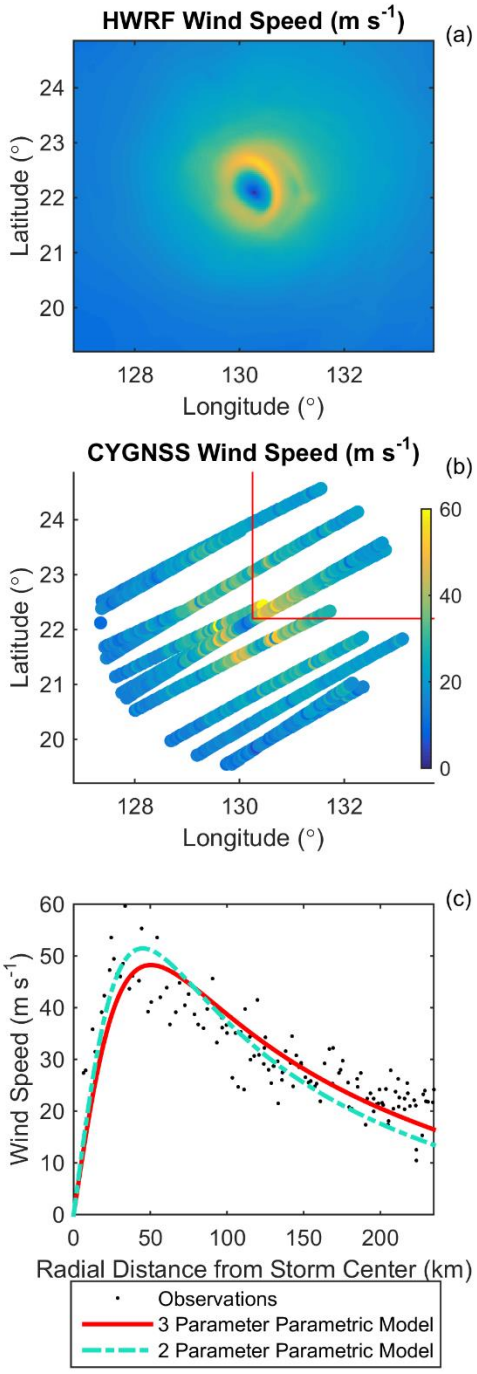

Figure 4.4: (a) HWRF wind speed field for Soulik on 11 July 2013, 03:00 UTC; (b) Simulated CYGNSS wind speed observations for (a) with the NE quadrant (cornered off by red lines) currently being considered; and (c) the parametric model algorithm fit for this NE quadrant test case, from which the NE quadrant wind radii are solved for.

Table 4.1: Coefficients used for translation from the parametric metrics to the scaled-parametric metrics, assuming the form of eqn.3.

Metric	a_0	a_1	a_2	a_3
V_{MAX} (m s^{-1})	5.605266	1.131274	0	0
R_{MAX} (km)	51.951488	0.228911	0.003682	-0.000006
R_{34} (km)	42.564232	1.098006	0	0
R_{50} (km)	11.904758	1.006752	0	0
R_{64} (km)	9.444089	0.975245	0	0

4.5 Initial Results

4.5.1 Performance without Quality Control

To illustrate the effect of applying the scaling factors described above, histograms of error are plotted in Figure 4.5 for each of the TC metrics. These histograms include all storm cases, with no QC filters related to algorithm performance applied. Both the parametric and scaled-parametric metrics are plotted to show that the scaling alleviates some of the larger biases in the parametric estimates. For example, there is a clear overall bias in the parametric V_{MAX} but, after the scaling correction is applied, the mean error is close to zero. The mean and standard deviation of each population of errors are reported in Table 4.2. For some metrics, the scaling factor improves performance much more than for others. The inner wind radii R_{50} and R_{64} have very small scaling factors; their performance improves by a small amount. The standard deviations reported in Table 4.2 show that R_{MAX} is the only metric where the scaling factors affect the root mean square (RMS) error by a significant amount. The RMS error can be further improved by applying QC filters, which will also improve some of the mean error values as well. These filters are developed below.

Table 4.2: Mean and standard deviation of the error plotted in Figure 4.5 for each parametric and scaled-parametric metric.

Metric	Mean		Standard Deviation	
	Parametric	Scaled-Parametric	Parametric	Scaled-Parametric
V_{MAX} (m s^{-1})	10.4	0.8	6.9	7.2
R_{MAX} (km)	1.7	-6.4	54.0	41.7
R_{34} (km)	57.4	-5.9	55.6	57.3
R_{50} (km)	11.9	-1.1	33.4	33.5
R_{64} (km)	5.7	-0.6	27.7	27.2

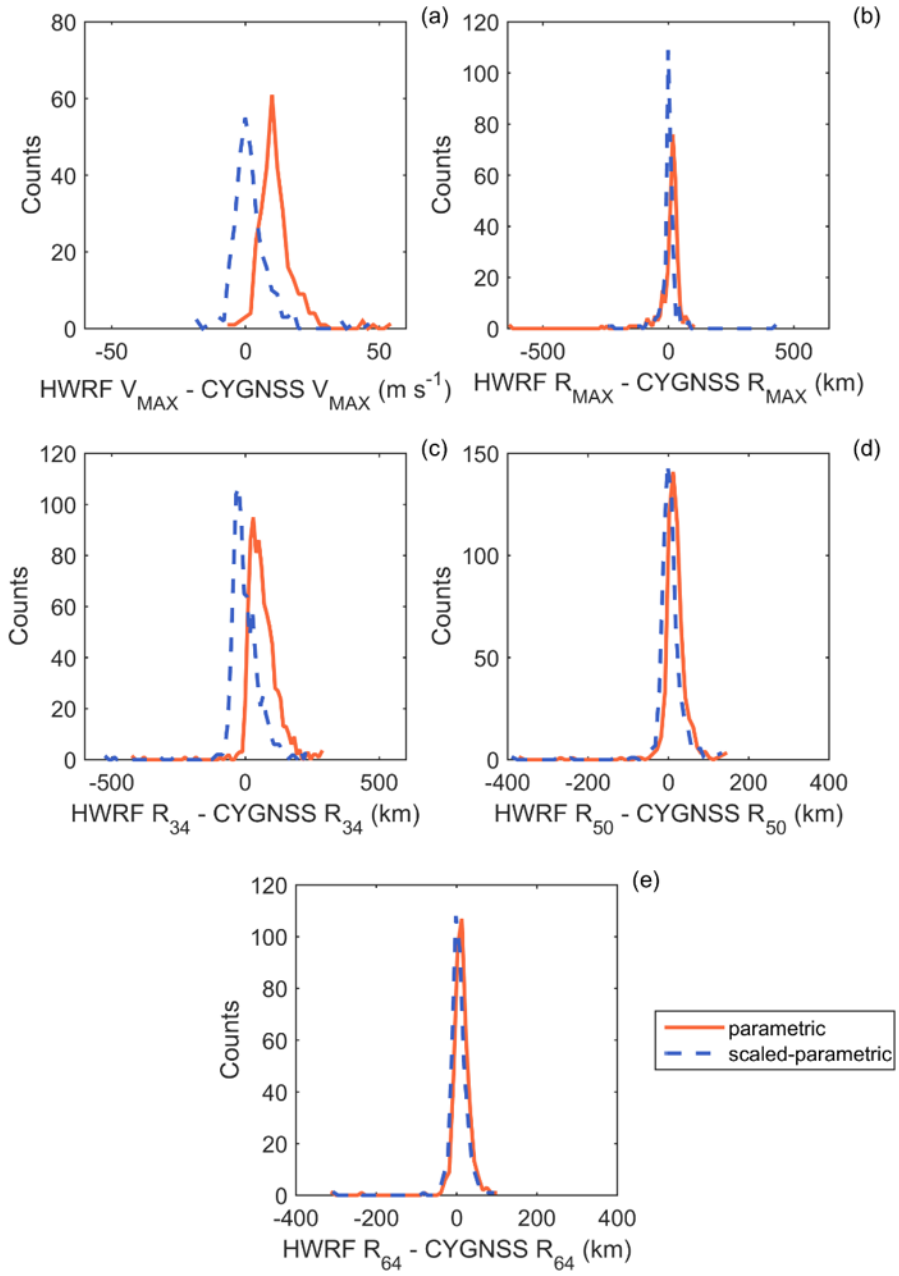

Figure 4.5: Histograms of error before quality control is applied in all parametric and scaled-parametric metrics. Error is defined here as true – estimated.

4.5.2 Sensitivity to Storm Center Location Error

One of the required inputs to the TC metric estimator algorithm is the location of the storm center. Center position uncertainty estimates vary widely depending on

the strength of the storm, as well as the data available for position estimation (Torn and Snyder 2012; Landsea and Franklin 2013). Torn and Synder (2012) estimated position uncertainty to be around 37-65 km.

Sensitivity experiments were performed to assess the impact of center location error on the metrics. In these experiments, the algorithm was executed multiple times using all available test cases, each time perturbing the center position latitude by an increasing amount. After performing some quality control (described in the following section) the error due to latitude offset was calculated by decomposing it from the overall error in the TC metric estimate. Specifically, the root mean square error (RMSE) due to center location offset is given by

$$RMSE_{off}(x) = \sqrt{RMSE_{total}(x)^2 - RMSE_{off_{x=0}}{}^2} \qquad (4.4)$$

where $RMSE_{total}$ is the total RMSE for a certain offset x and $RMSE_{off_{x=0}}$ is the RMSE with no latitude offset. The results are shown in Figure 4.6 for V_{MAX} and R_{MAX}, the metrics that are derived using observations from all four quadrants and in Figure 4.7 for wind radii, the metrics derived in individual quadrants. For the wind radii, the NE quadrant was used.

The results are similar in other quadrants. The results show a consistent, monotonic increase in error with increasing uncertainty in the storm center location for all TC metrics. For example, a storm center offset of 55 km introduces an RMS error in V_{MAX} of 4.7 m s^{-1}, in R_{MAX} of 12 km and in R_{64}, R_{50} and R_{34} of 39 km, 43 km, and 48 km, respectively. In terms of relative error (relative to the mean value of each TC metric), these errors correspond to 12% for V_{MAX}, 13% for R_{MAX}, and 32%, 28% and 19% for R_{64}, R_{50} and R_{34}.

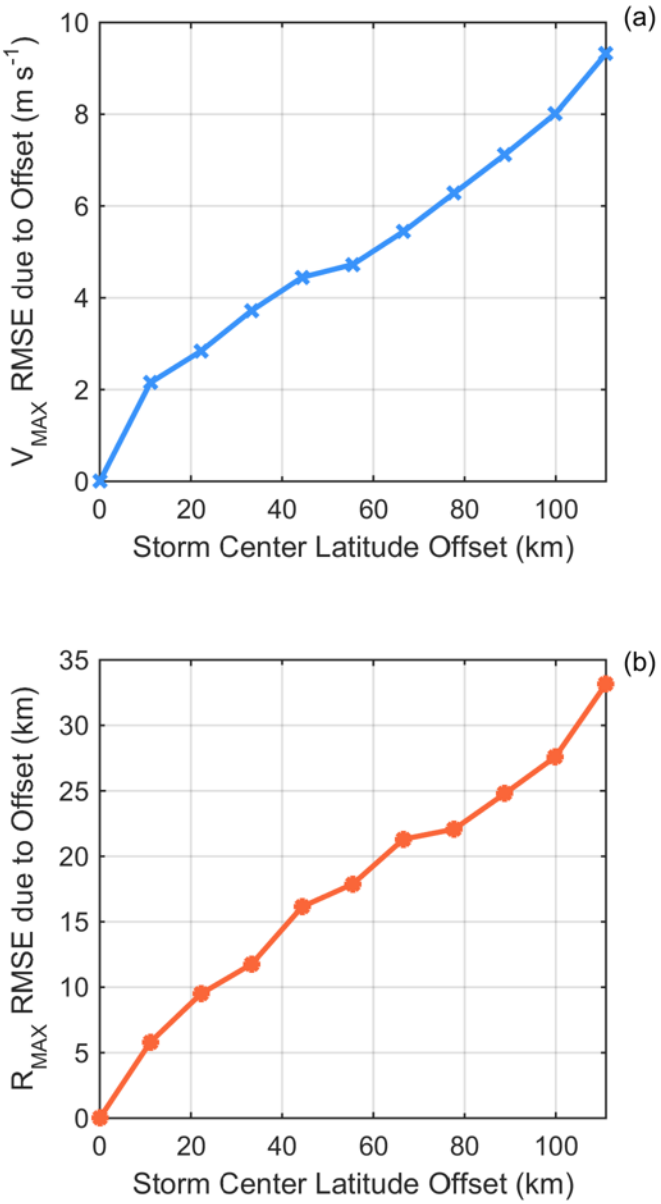

Figure 4.6: The additional error on average to expect from storm center offsets (here, only in latitude) for (a) V_{MAX} and (b) R_{MAX}.

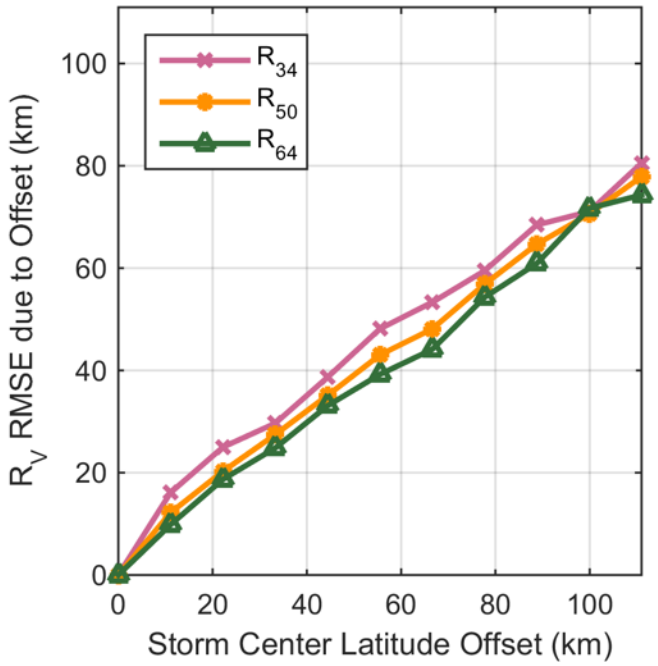

Figure 4.7: The additional error on average to expect from storm center offsets (here, only in latitude) for wind radii. This analysis is based on the cases available in the NE quadrant.

4.5.3 Sensitivity to CYGNSS Coverage

The spatial distribution of observations, or coverage, by CYGNSS of the TC wind field will affect the quality of its retrieval of the TC metrics. The sensitivity of the retrievals to coverage is illustrated in Figure 4.8 - 4.9. Different sampling characteristics are considered for different TC metrics. Figure 4.8 shows the sensitivity of (a) V_{MAX} and (b) R_{MAX} estimates to the number of CYGNSS samples within 100-km of the storm center. The RMSD between the HWRF and CYGNSS values is shown for different populations of storm cases, with the population selected based on the number of samples. The x-axis in the figure is the threshold (minimum) number of samples required. For example, an x-axis value of 10 means that only storm cases are considered for which at least 10 CYGNSS samples are within 100 km of the storm center. As the threshold is increased, more under sampled cases are thrown out and the performance improves. An adequate number of CYGNSS observations are needed within the inner core in order to make an accurate estimate of inner core metrics like V_{MAX} and R_{MAX}.

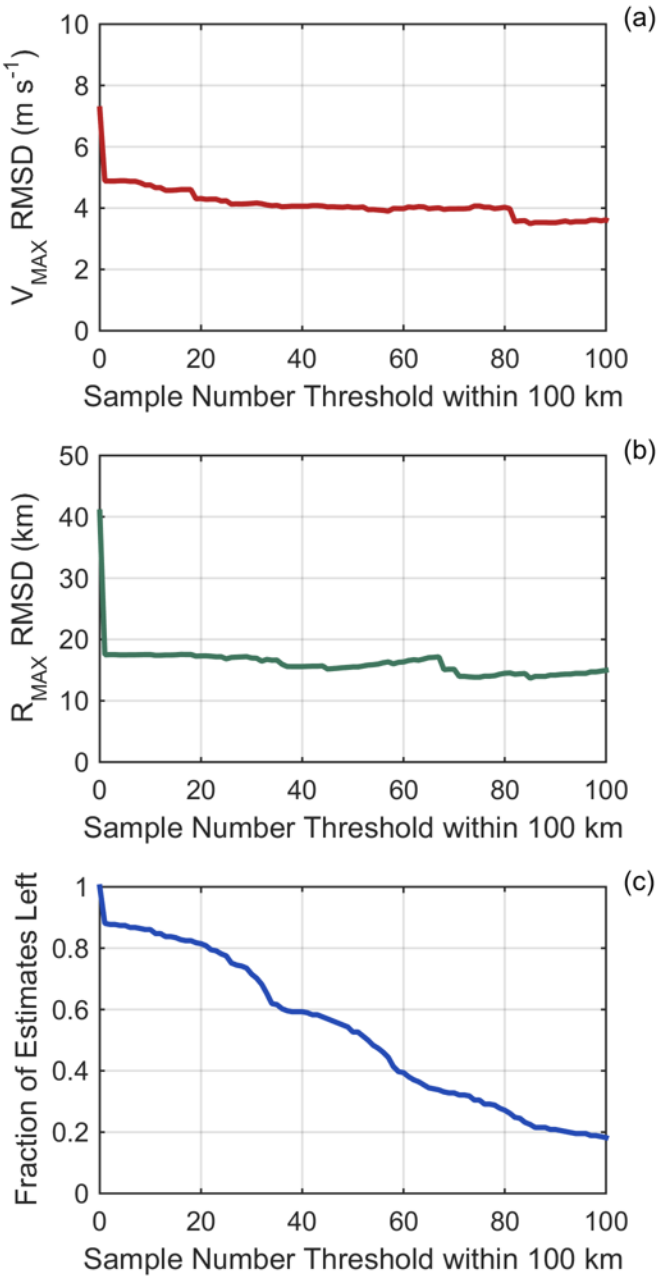

Figure 4.8: (a) The RMSD between the HWRF and CYGNSS derived V_{MAX} depending on the quality control filter threshold used. The quality control keeps test cases that have a number of observations within 100-km from the storm center above the sample number threshold plotted on the x-axis. (b) The same as (a), but for R_{MAX}. (c) The fraction of the original test case estimates left that are used to derive the RMSD in (a) and (b).

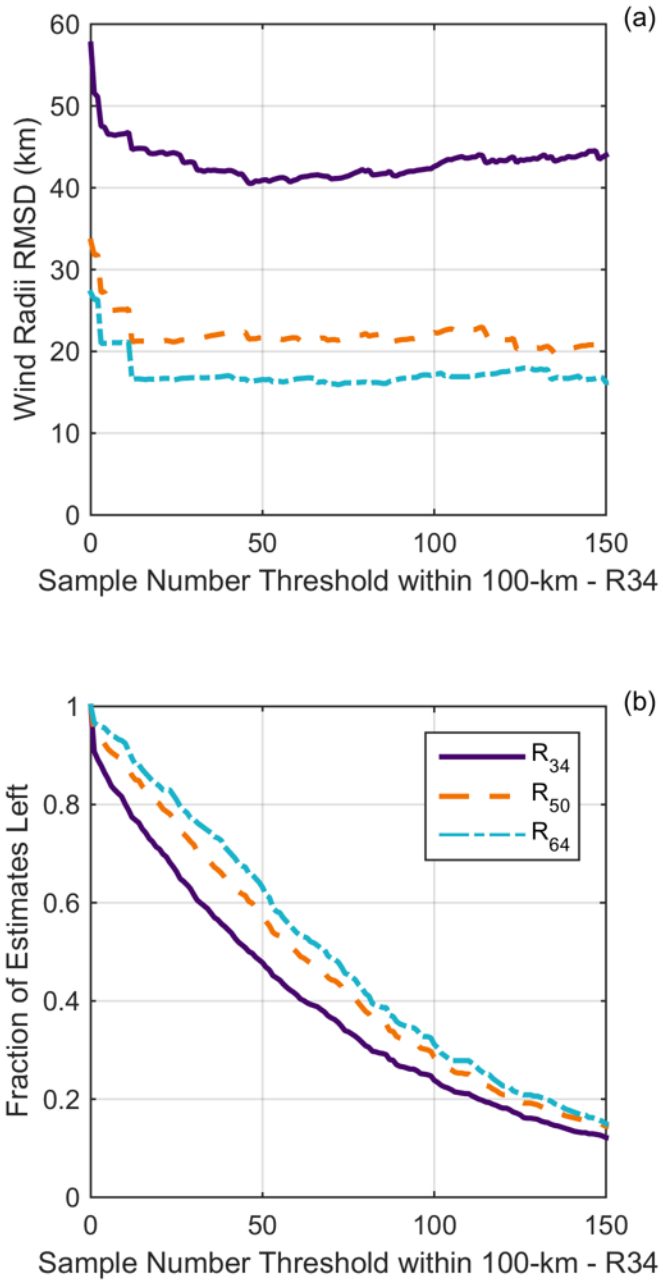

Figure 4.9: (a) The RMSD between the HWRF and CYGNSS derived wind radii depending on the quality control applied. The quality control keeps test cases that have a number of observations outside 100-km from the storm center (but within the estimate of R_{34}) above the sample number threshold plotted on the x-axis. (b) The fraction of the original test case estimates left that are used to derive the RMSD in (a).

Figure 4.9 shows the results of a similar sensitivity experiment for the wind radii. Here, a different sampling characteristic was found to be more indicative of the performance. The number of CYGNSS samples between 100 km and R34 was used for quality control. As above with V_{MAX} and R_{MAX}, as the minimum threshold for the number of samples increases, the performance of the wind radii estimates improves (see Figure 4.9a). Of course, the more stringent the threshold is, the fewer cases remain (see Figure 4.9b).

4.5.4 Quality Control Test Procedures

QC filters are derived using the results of the sensitivity experiments. The filters are intended to identify CYGNSS sampling conditions under which the TC metric estimates are of acceptable quality. However, the filters should not be so stringent that they eliminate too large a fraction of the possible storm cases. For estimates of V_{MAX} and R_{MAX}, a sampling threshold test is used given by

$$num_{obs_{100}} \geq N \tag{4.5}$$

where $num_{obs_{100}}$ is the number of observations within 100-km of the storm center for a particular storm case and N is the filter threshold. For this study, we choose N = 20 as a good balance between high algorithm performance and not filtering out too many storm cases. For estimates of wind radii, a different sampling test is used given by

$$num_{obs_{100-R34}} \geq M \tag{4.6}$$

where $num_{obs_{100-R34}}$ is the number of observations between 100-km of the storm center and R_{34} for a particular quadrant and M is the filter threshold. For this study, we choose M = 30. Higher values produce only marginal improvement in performance while eliminating a significant fraction of the storm cases.

4.6 Final Results

Figure 4.10 shows the histograms of error for all TC metrics after the QC filters described above have been applied. The original histogram data shown in Figure 4.5 are included for convenience. The means and standard deviations derived from the Figure 4.10 cases are listed in Table 4.3. Overall, the QC filters remove the egregious outliers while retaining most of the higher quality estimates. As a result, the RMSE in the metrics is improved. Additionally, the bias in the estimates remains small after QC filters are applied. Our results are comparable or better than results from other methods. For example, the errors in wind radii reported in Knaff et al. (2016) range from 19 – 85 km in mean absolute error, while our current estimates for wind radii range from around 20 – 45 km in RMS error.

Table 4.3: Mean and standard deviation of the error plotted in Figure 4.10 for each parametric and scaled-parametric metric, as well as the quality controlled scaled-parametric metrics.

Metric	**Mean**			**Standard Deviation**		
	Parametric	Scaled-Parametric	Post-QC	Parametric	Scaled-Parametric	Post-QC
V_{MAX} (m s^{-1})	10.4	0.8	-0.4	6.9	7.2	4.3
R_{MAX} (km)	1.7	-6.4	-0.04	54.0	41.7	17.4
R_{34} (km)	57.4	-5.9	-4.6	55.6	57.3	41.3
R_{50} (km)	11.9	-1.1	2.1	33.4	33.5	21.6
R_{64} (km)	5.7	-0.6	1.6	27.7	27.2	16.8

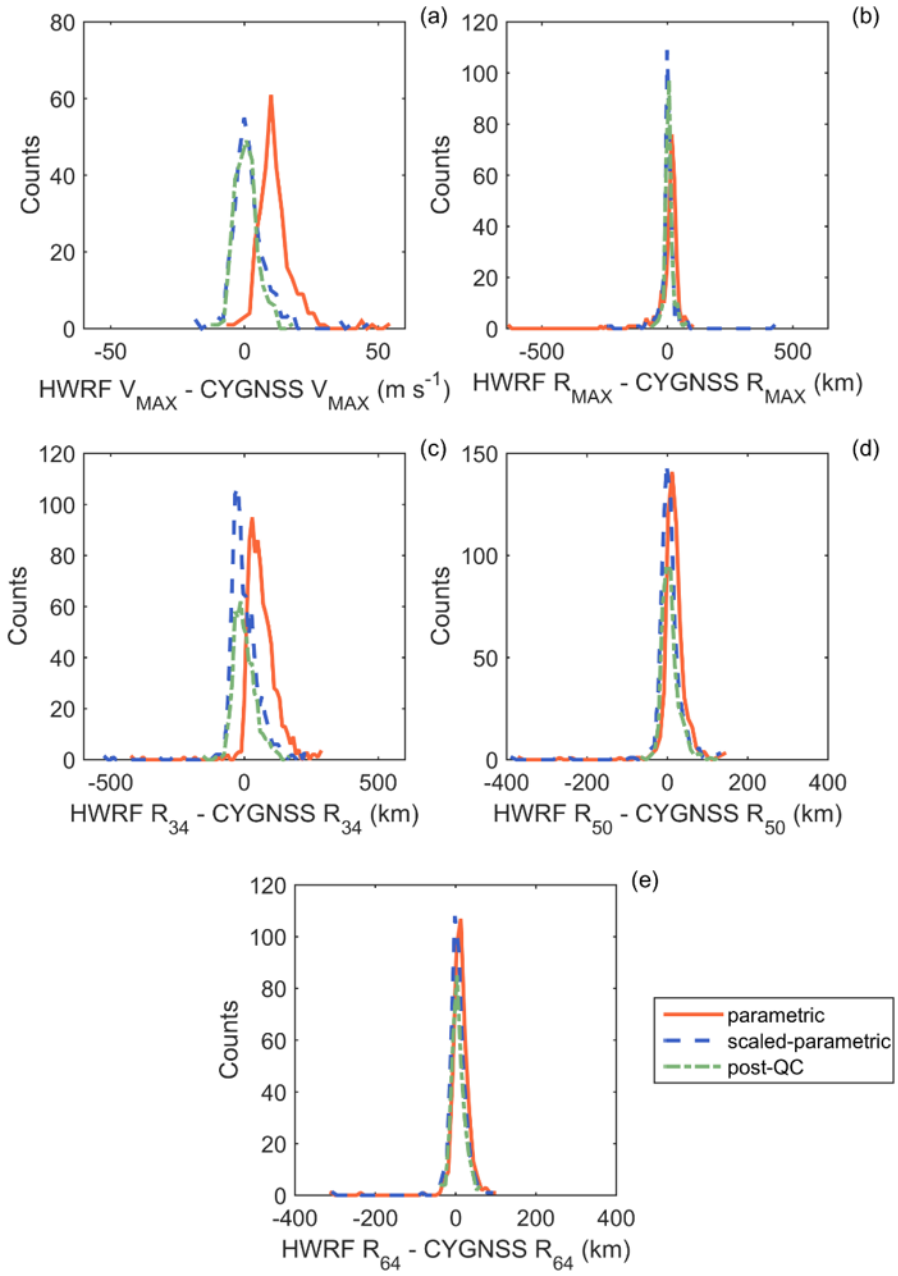

Figure 4.10: Histograms of error in all parametric, scaled-parametric, and quality controlled scaled-parametric metrics. Error is defined here as true – estimated.

4.7 Discussion

The methods presented here enable CYGNSS-based estimates of V_{MAX}, R_{MAX}, and wind radii. The estimates require a sufficient number of observations in the appropriate regions of the storm; this requirement is met using appropriate quality control filters. For example, data availability within the inner core best predicts the quality of the inner core metrics, namely V_{MAX} and R_{MAX}. Wind radii estimates require sufficient sampling in an annular region outside of the inner core of the storm, between 100-km and R_{34}, and the sampling is quadrant-dependent.

Another potential factor in performance is the type and location of the storm. Figure 4.11 examines the impact that intensity has on the performance of the V_{MAX} and R_{MAX} estimates. Here the test cases are separated into those that, according to HWRF, have an intensity estimate either below or above 33 m s^{-1}—differentiating between tropical storm and hurricane strength. Figure 4.11a shows that the spread in error is slightly larger in the stronger storms. Figure 4.11b shows that the spread in R_{MAX} error is larger for tropical storms. Both of these performance distinctions make sense considering that, in both instances, the spread is larger for the population with larger values of the metric in question.

Figure 4.12 compares the performance of all TC metrics depending on the basin location of the storm. The error plotted is with QC filtering. Notably, the spread in V_{MAX} error is larger in the Western Pacific test cases, which makes sense as these cases tend to have higher intensity. Another interesting take-away from Figure 4.12 is shown in Figure 4.12c; here, the bias in Atlantic and Eastern Pacific R_{MAX} error is more pronounced than that in the Western Pacific. Basin-specific R_{MAX} performance will be examined further post-launch with CYGNSS data in order to determine whether different scaling factors are required for different basins. In summary, Figure 4.11-4.12 illustrate situations where one might expect better or worse performance.

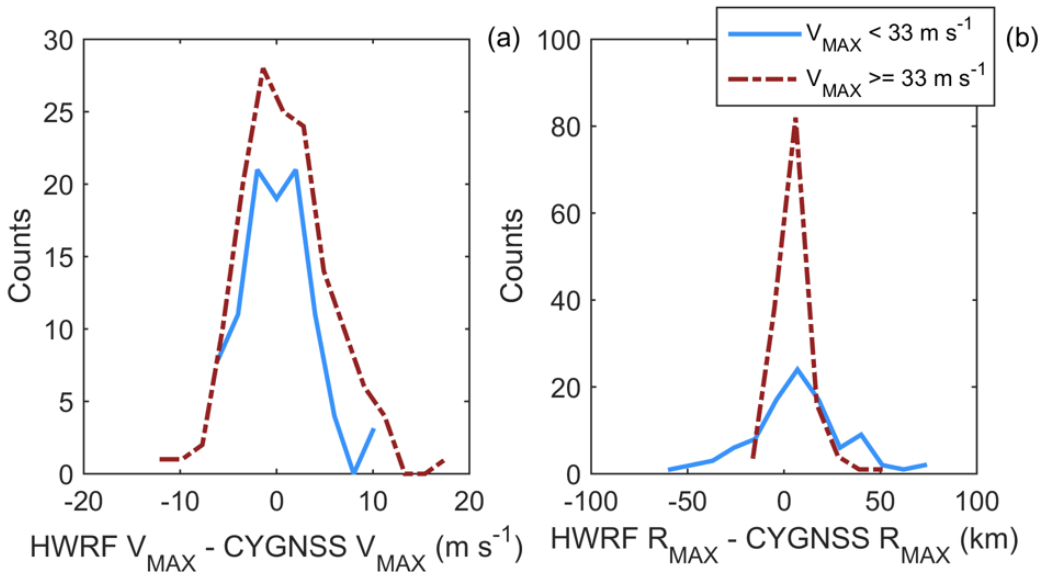

Figure 4.11: Histograms of the quality controlled scaled-parametric V_{MAX} and R_{MAX} depending on the HWRF V_{MAX} threshold attained. Weaker storms (V_{MAX} < 33 m s^{-1}) are plotted in solid light blue. Stronger storms (V_{MAX} >= 33 m s^{-1}) are plotted in dashed dark red.

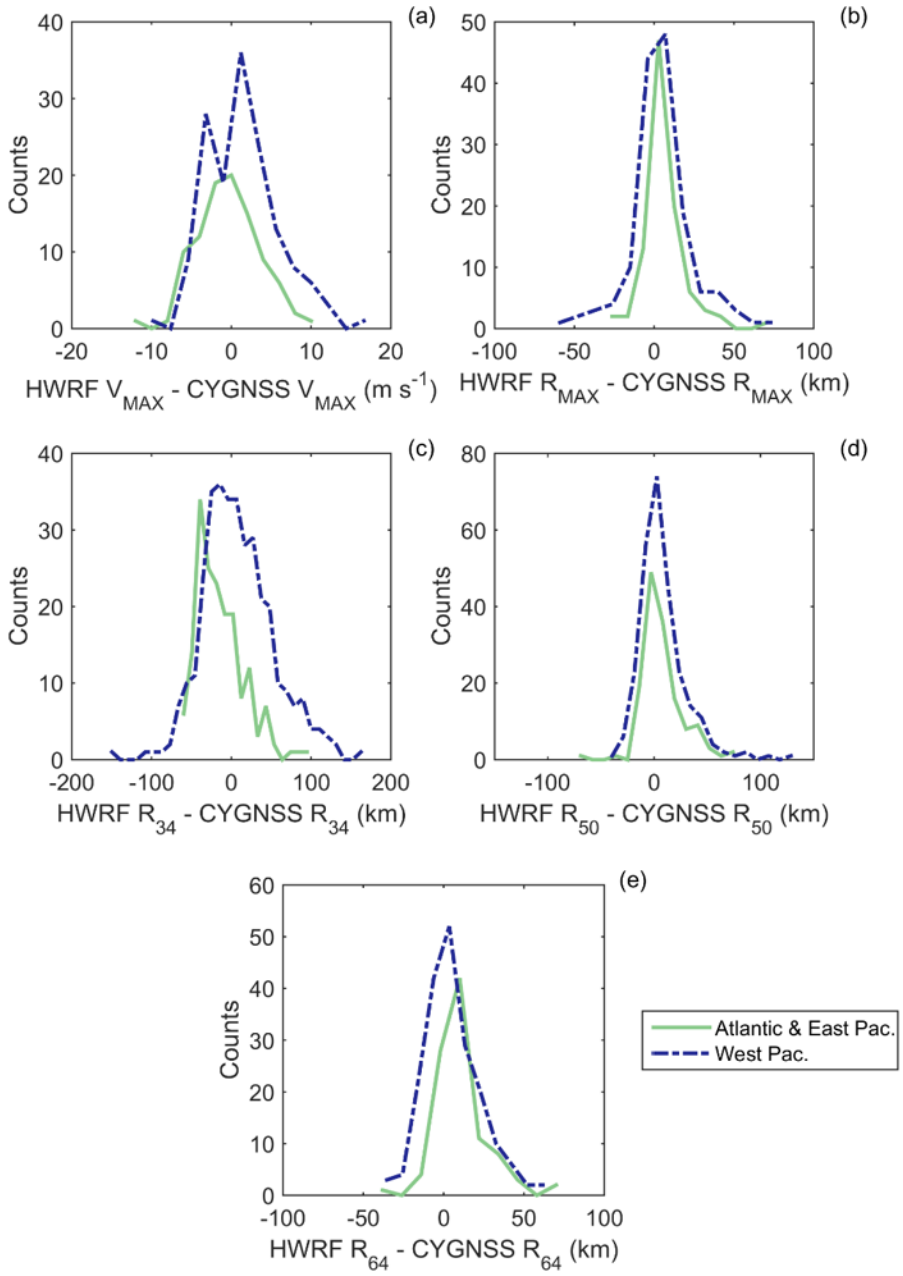

Figure 4.12: Histograms of the quality controlled scaled-parametric metrics depending on the test case basin. Storms from the Atlantic and East Pacific basins are plotted in solid light green. Storms from the Western Pacific basin are plotted in dashed dark blue.

4.8 Conclusions

CYGNSS will allow for a unique opportunity to estimate certain metrics of tropical cyclones that are typically quite challenging to estimate with other platforms. Since CYGNSS observations consist of collections of tracks rather than complete swaths, new estimation methods have been developed which effectively interpolate between observations in order to produce the TC metric estimates.

This study uses a mission simulator which reproduces realistic sampling patterns to be expected with CYGNSS. Sampling patterns are important to consider, as the quality of the TC metric estimates can depend strongly on them. Given good coverage, the methodology presented here enables V_{MAX}, R_{MAX}, and wind radii estimates to be made from two inputs: 1) CYGNSS observations and 2) the storm center location.

Future work includes calibration and validation of the TC metric estimates made from actual on-orbit CYGNSS data. Calibration might, for example, include re-tuning of the scaled parametric relationships described in Section 4.4.4, or revision of the QC filter thresholds. Validation will follow from comparisons with coincident ground truth sources such as HWRF wind fields or airborne reconnaissance underflights. Future work also includes testing other types of parametric models in this methodology, developing a CYGNSS-based storm center position corrector, and determining the utility of a CYGNSS-based storm center position corrector to this application and others. Finally, while these methods were developed with CYGNSS in mind, it is possible that this methodology could also be applied to other types of observations, in particular those for which gaps in spatial sampling also exist.

Appendix 4.I

Table 4.I.1: A summary of all of the storms used in this study, with the storm name, the number of cases for that particular storm, the maximum wind speed (V_{MAX}), the storm center latitude and longitude at the point in time corresponding to the V_{MAX} case, and the year for each storm.

Storm Name	# of Storm Test Cases	V_{MAX} (m s^{-1})	Storm Center Latitude (˚N)	Storm Center Longitude (˚E)	Storm Test Case Year
Danielle	11	54	26.8	300.3	2010
Estelle	4	27	17.3	250.8	2010
Frank	2	40	17.7	250.6	2010
Igor	13	66	17.6	310.7	2010
Julia	7	59	17.7	327.8	2010
Adrian	6	63	14.5	254.7	2011
Bret	1	24	29.8	284	2011
Calvin	3	36	16.7	250.9	2011
Dora	2	41	19.4	250.6	2011
Eugene	14	61	15.7	245.3	2011
Fernanda	5	28	14.7	217.3	2011
Gert	2	24	37.9	303	2011
Greg	4	36	18.5	248.6	2011
Hilary	12	59	17.1	250.6	2011
Katia	15	55	27	294.1	2011
Maria	4	33	33.7	293.1	2011
Ophelia	4	50	24	296.9	2011
Philippe	4	25	22.9	314.8	2011
Yagi	3	26	28.6	136.5	2013
Leepi	1	21	19.6	126.1	2013
Soulik	14	66	21.3	135.3	2013
Eleven	2	72	15.7	132.7	2013
Trami	2	28	19.9	128.3	2013
Man-yi	1	24	25.8	136	2013
Usagi	5	57	17.9	127.6	2013
Pabuk	12	46	29.4	139	2013
Wutip	1	27	16.4	114.1	2013
Fitow	13	47	24.5	127.3	2013
Danas	8	47	22.8	133.4	2013
Nari	1	50	15.3	114.2	2013
Francisco	20	71	17.8	137.8	2013
Lekima	12	74	19	150.9	2013
Krosa	3	31	17	127.6	2013
Tapah	3	39	14.5	147.5	2014
Eight	8	62	18.1	132.1	2014
Nine	3	47	16.6	115.4	2014
Matmo	10	45	13.5	129.3	2014
Eleven	28	72	15.7	132.7	2014
Fengshen	5	28	29.5	136.6	2014
Fifteen	2	24	13.6	130.8	2014
Kammuri	7	28	23	145.7	2014
Phanfone	11	59	20.2	137.6	2014

Vongfong	14	74	18	131.9	2014

Chapter 5. Summary and Future Work

5.1 Summary of Original Contributions

5.1.1 Brief Review of Thesis

TCs are important to observe, especially over the course of their lifetimes, most of which is spent over the ocean. Very few in situ observations are available. Remote sensing has afforded researchers and forecasters the ability to observe and understand TCs better. Every remote sensing platform used to observe TCs has benefits and disadvantages. Some remote sensing instruments are more sensitive to clouds, precipitation, and other atmospheric constituents. Some remote sensing instruments are insensitive to the atmosphere, which allows for unobstructed observations of the ocean surface. Observations of the ocean surface, either of surface roughness or emission can be used to estimate ocean surface wind speed. Estimates of ocean surface wind speed can help determine the intensity and destructive potential of TCs, as well as the radial extent of specified strengths of wind. While there are many methods by which TCs are observed, this thesis focuses on two main types of remote sensing techniques: passive microwave radiometry and GNSS-R.

Chapter 2 discusses work that was done as a part of the HIRAD mission. HIRAD, an airborne passive microwave radiometer, operates at C-band frequencies, and is sensitive to rain absorption and emission, as well as ocean surface emission. A more robust retrieval algorithm was developed to estimate rain rate and surface wind speed from HIRAD observations. The development of this algorithm was motivated by the unique observing geometry and high gradient rain scenes that HIRAD observes. HIRAD's observing geometry must be accounted for in the forward model and retrieval algorithm, if high rain gradients

are to be estimated from HIRAD's observations, with the ultimate goal of improving surface wind speed estimation.

Chapters 3 and 4 develop higher level TC science data products from simple inputs of CYGNSS level-2 surface wind speed and the assumed known storm center location. From these simple inputs, a variety of products have scientific and forecasting applications: IKE, wind radii, R_{MAX}, and V_{MAX}. These higher level TC products provide information about the wind structure and intensity of storms, which is valuable for situation awareness, as well as science applications.

A full outline of all original work, including publications with work not included in this thesis, but related to the CYGNSS and HIRAD missions is discussed in the following section.

5.1.2 Original Work

5.1.2.1 Peer-reviewed Journal Publications

- Developed a method to estimate TC maximum wind speed, radius of maximum wind speed, and wind radii from CYGNSS level-2 surface wind speed observations (Morris and Ruf 2016b)
- Developed a method to estimate TC integrated kinetic energy from CYGNSS level-2 surface wind speed observations (Morris and Ruf 2016a)
- Developed a more robust level-2 retrieval algorithm for HIRAD that gets rid of assumptions previously used—invalid for the observing geometry of HIRAD and high-rain-gradient TC scenes. With this algorithm, we can partially deconvolve the beam-averaged observations, getting closer to the truth. (Morris and Ruf 2015a)

5.1.2.2 Peer-reviewed Conference Proceedings Publications

- Determined antenna temperature valid at the CYGNSS operating frequency, a parameter which will be used in the level-1A CYGNSS calibration over open-ocean. (Morris et al. 2016)

- Quantified the limit to the amount of deconvolution possible at different portions of the cross-track swath using the CPM algorithm. (Morris and Ruf 2015b)

5.1.2.3 Other Publications

- Provided support for the CYGNSS level-1A calibration and level-2 MSS algorithms. Provided a description of the radiative transfer model that is used in the CYGNSS level-1A calibration algorithm, and figures that show the Fresnel reflection coefficients to be used in the level-2 MSS algorithm. (Ruf et al. 2016)

5.2 Future Work

5.2.1 General Applicability of the Parametric Wind Model Algorithm

The parametric wind model algorithm which forms the basis for several higher level CYGNSS TC data products may be applicable to other observing systems. The objective of the work discussed in chapters 3 and 4 is to determine how to take advantage of the information content in the CYGNSS level-2 wind speed observations in order to estimate TC parameters of interest. Creating CYGNSS-based products allows for examination of the potential utility of a new and unique dataset. The products developed in chapters 3 and 4 are based on CYGNSS data, but other available surface wind speed products could also be used. The parametric wind model algorithm methods were developed because CYGNSS level-2 wind speed data has gaps. Other wind speed data products also have gaps in coverage over a storm. A number of questions remain for future work, but in particular it would be interesting to explore the following questions:

1. Could the parametric wind model algorithm methodology be applicable to other observing systems?

2. Could other wind speed observations be used in conjunction with CYGNSS observations to improve the performance of the TC parameter products discussed in chapters 3 and 4?

For example, scatterometer observations are plagued by rain contamination and loss of sensitivity at higher wind speeds. Experiments could be performed to see if the parametric wind model algorithm methodology would work if scatterometer observations, after rain contamination flags are applied, were input into the parametric wind model algorithm, and the same TC parameters were estimated. Since scatterometer observations lose sensitivity at high wind speeds, this methodology might be especially attractive if CYGNSS and scatterometer winds are used in combination; CYGNSS would provide valuable inner core data, and scatterometers more complete outer core data.

This experiment could be extended to look at the applicability of CYGNSS with other types of ocean surface wind speed data. Each dataset would have its own strengths and weaknesses, but if data are used in conjunction, the weaknesses of one instrument would be complimented by the strengths of another instrument. For example, CYGNSS performance is expected to be superior at low wind speed. Passive microwave radiometers, due to the onset of ocean surface foaming, perform better at higher wind speeds. Combining passive observations from SMAP and active observations from CYGNSS, both at L-band, could provide complementary information and improve the estimates of TC parameters. These data could be combined in a complementary way to get accurate surface wind speed over the entire storm.

It should also be noted that the overall methodology presented in chapter 4 requires that scaling factors, which scale the parametric model values to estimates of true parameters of interest, be produced. If this methodology were to be applied to other types of wind speed data, it is unlikely that the scaling factors used for the CYGNSS-based methods would be appropriate for the other data. In fact, the scaling factors developed in chapter 4 will be re-examined and tuned according to the performance of on-orbit data.

5.2.2 Science Applications from CYGNSS L4 Products

There are numerous potential applications of CYGNSS TC data products. This section discusses just one opportunity for the applicability of CYGNSS data products in TC research.

5.2.2.1 Investigation of Environmental Humidity Controls on TC Intensity and Structure

The processes that underlie TC intensification are not fully understood (Rogers et al. 2006). In particular, the control of environmental moisture on TC intensification is not clear (Kaplan and DeMaria 2003; Kimball 2006; Hill and Lackmann 2009; Shu and Wu 2009; Braun et al. 2012; Wu et al. 2012; Wu et al. 2015). Dry or humid environments surrounding TCs have the potential to cause significant changes in the convective structure of TCs, which consequently change TC wind structure and intensity. CYGNSS TC data products could be used to investigate the impact of environmental humidity on TCs. In particular, CYGNSS data could be used to characterize of the relationship between surface wind structure and intensity with environmental humidity and precipitation. Previous studies do not agree on the relationship between environmental moisture and TC intensification. Increased understanding of these processes will help to improve TC forecasting efforts.

In order to investigate the relationship between the TC characteristics and environmental humidity, satellite observations of environmental humidity, precipitation, and surface wind speed would be needed. Environmental humidity data are available twice daily from the AIRS mission. CYGNSS TC data products would give the necessary wind structure and intensity information. The GPM mission provides estimates of precipitation. These data, used in combination, will allow for case studies and composite statistical analyses of the relationship between environmental humidity and TC characteristics.

5.2.3 Orbit Configuration Optimization for CYGNSS TC Product Performance

The CYGNSS TC data products were developed and tested with the sampling properties expected of the upcoming mission. The CYGNSS constellation consists of eight satellites in a 35-degree inclination circular orbit. This design maximizes the coverage over the tropics under the cost constraints of the mission. While this setup gives good coverage over the tropics, there are times when CYGNSS will miss storms. In addition to occasional misses of TCs in the current tropical coverage, TCs which exist north and south of the current CYGNSS tropics sampling extent will also be missed. Without data, TC products cannot be produced. Data gaps in coverage over the lifetime for any storm are not ideal if these data are used in TC process studies. Therefore, it would be useful to know how to efficiently and effectively observe the entire planet with a larger constellation. A number of specific questions are posed here for future investigation:

1. If TC science data products are needed from CYGNSS every three hours on a consistent and uniform basis, what type of constellation (how many satellites, how many orbit planes, and how best to distribute the satellites between them) would need to be flown?

2. How much impact would additional polar orbiting CYGNSS microsatellites have on improving TC data product performance and coverage?

3. What types of coverage would be needed to maximize the performance of the CYGNSS TC data products?

If CYGNSS TC data products could be provided with more consistent temporal resolution, their applicability to TC process studies would improve. More study is needed to determine how to optimize constellation-type missions like CYGNSS.

References

Amarin, R. A., 2010: Hurricane wind speed and rain rate measurements using the airborne Hurricane Imaging Radiometer (HIRAD), University of Central Florida, 171 pp.

Amarin, R. A., W. L. Jones, S. F. El-Nimri, J. W. Johnson, C. S. Ruf, T. L. Miller, and E. Uhlhorn, 2012: Hurricane Wind Speed Measurements in Rainy Conditions Using the Airborne Hurricane Imaging Radiometer (HIRAD). *IEEE Trans. Geosci. Remote Sens*., **50**, 180-192.

Bessho, K., M. DeMaria, and J. A. Knaff, 2006: Tropical cyclone wind retrievals from the Advanced Microwave Sounder Unit (AMSU): Application to surface wind analysis. *J. Appl. Meteor. Climatol*., **45**, 399–415.

Braun, S. A., J. A. Sippel, and D. S. Nolan, 2012: The Impact of Dry Midlevel Air on Hurricane Intensity in Idealized Simulations with No Mean Flow. *J. Atmos. Sci*., **69**, 236-257.

Braun, S. A., and Coauthors, 2013: NASA'S GENESIS AND RAPID INTENSIFICATION PROCESSES (GRIP) FIELD EXPERIMENT. *Bull. Amer. Meteor. Soc*., **94**, 345-363.

Brennan, M. J., C. C. Hennon, and R. D. Knabb, 2009: The operational use of QuikSCAT ocean vector winds at the National Hurricane Center, *Weather Forecast.*, **24**, 621–645.

Brown, D. P., 2010: Tropical Cyclone Report: Tropical Storm Colin. 11 pp, http://www.nhc.noaa.gov/data/tcr/AL042010_Colin.pdf

Brown, D. P., and J. L. Franklin, 2004: Dvorak TC wind speed biases determined from reconnaissance-based best track data (1997–2003). Preprints, 26th Conf. on Hurricanes and Tropical Meteorology, Miami, FL, Amer. Meteor. Soc., 86–87.

Burpee, R. W., 1972: The Origin and Structure of Easterly Waves in the Lower Troposphere of North Africa. *J. Atmos. Sci.*, **29**, 77-90.

Cangialosi, J. P.: 2011, Tropical Cyclone Report: Hurricane Earl. 29 pp, http://www.nhc.noaa.gov/data/tcr/AL072010_Earl.pdf

Cahalan, R. F., W. Ridgway, W. J. Wiscombe, T. L. Bell, and J. B. Snider, 1994: The albedo of fractal stratocumulus clouds, *J. Atmos. Sci*., **51**, 2434-2455.

Cahalan, R., and Coauthors, 2005: THE I3RC: Bringing Together the Most Advanced Radiative Transfer Tools for Cloudy Atmospheres. *Bull. Amer. Meteor. Soc.*, **86**, 1275–1293.

Chavas, D. R., N. Lin, and K. Emanuel, 2015: A model for the complete radial structure of the tropical cyclone wind field. Part I: Comparison with observed structure. *J. Atmos. Sci*, **72**, 3647–3662.

Chen, F. W., and D. H. Staelin, 2003: AIRS/AMSU/HSB precipitation estimates. *IEEE Trans. Geosci. Remote Sens*., **41**, 410-417.

Chu, J.-H., C. R. Sampson, A. S. Levin, and E. Fukada, 2002: The Joint Typhoon

Warning Center tropical cyclone best tracks 1945-2000. Joint Typhoon Warning Center Rep., Pearl Harbor, HI, 22 pp.
Clarizia, M. P., and C. S. Ruf, 2016: Wind Speed Retrieval Algorithm for the Cyclone Global Navigation Satellite System (CYGNSS) Mission. *IEEE Trans. Geosci. Remote Sens.,* 10.1109/TGRS.2016.2541343
Demuth, J. L., M. DeMaria, and J. A. Knaff, 2006: Improvement of advanced microwave sounding unit tropical cyclone intensity and size estimation algorithms. *J. Appl. Meteor. Climatol.*, **45**, 1573-1581.
Dolling, K., E. Ritchie, and J. Tyo, 2016: The Use of the Deviation Angle Variance Technique on Geostationary Satellite Imagery to Estimate Tropical Cyclone Size Parameters. *Wea. Forecasting*, **31**, 1625–1642, doi: 10.1175/WAF-D-16-0056.1.
Droppleman, J. D., 1970: APPARENT MICROWAVE EMISSIVITY OF SEA FOAM. *J. Geophys. Res*., **75**, 696-+.
Dunion, J. P., and C. S. Velden, 2002: Application of surface-adjusted GOES low-level cloud-drift winds in the environment of Atlantic tropical cyclones. Part I: Methodology and validation. *Mon. Wea. Rev*., **130**, 1333–1346.
Dvorak, V. F., 1975: TROPICAL CYCLONE INTENSITY ANALYSIS AND FORECASTING FROM SATELLITE IMAGERY. *Mon. Wea. Rev*., **103**, 420-430.
Dvorak, V. F., 1984: Tropical cyclone intensity analysis using satellite data. NOAA Tech. Rep. 11, 45 pp.
Ebuchi, N., H. C. Graber, and M. J. Caruso, 2002: Evaluation of wind vectors observed by QuikSCAT/SeaWinds using ocean buoy data. *J. Atmos. Oceanic Technol.*, **19**, 2049-2062.
El-Nimri, S. F., W. L. Jones, E. Uhlhorn, C. Ruf, J. Johnson, and P. Black, 2010: An Improved C-Band Ocean Surface Emissivity Model at Hurricane-Force Wind Speeds Over a Wide Range of Earth Incidence Angles. IEEE Geoscience and Remote Sensing Letters, 7, 641-645.
Emanuel, K. A., 1986: AN AIR SEA INTERACTION THEORY FOR TROPICAL CYCLONES .1. STEADY-STATE MAINTENANCE. *J. Atmos. Sci*., **43**, 585-604.
——, 1988a: THE MAXIMUM INTENSITY OF HURRICANES. *J. Atmos. Sci*., **45**, 1143-1155.
——, 1988b: TOWARD A GENERAL-THEORY OF HURRICANES. American Scientist, 76, 371-379.
Emanuel, K. 2004: Tropical cyclone energetics and structure, in Atmospheric Turbulence and Mesoscale Meteorology, edited by E. Fedorovich, R. Rotunno, and B. Stevens, pp. 165–192, Cambridge Univ. Press, Cambridge, U. K., doi:10.1017/CBO9780511735035.010.
Emanuel, K., and R. Rotunno, 2011: Self-stratification of tropical cyclone outflow. Part I: Implications for storm structure. *J. Atmos. Sci*., **68**, 2236–2249.
Fetanat, G., and A. Homaifar, 2013: Objective tropical cyclone intensity estimation using analogs of spatial features in satellite data. *Wea. Forecasting*, **28**, 1446–1459, doi:10.1175/WAF-D-13-00006.1
Figa-Saldana, J., J. J. W. Wilson, E. Attema, R. Gelsthorpe, M. R. Drinkwater,

and A. Stoffelen, 2002: The advanced scatterometer (ASCAT) on the meteorological operational (MetOp) platform: A follow on for European wind scatterometers. Canadian Journal of Remote Sensing, **28**, 404-412.
Fore, A. G., S. H. Yueh, W. Tang, B. Stiles, A. K. Hayashi, 2016: Combined Active/Passive Retrievals of Ocean Vector Wind and Sea Surface Salinity With SMAP. IEEE Trans. Geosci. Remote Sens., **54**, 7396-7404.
Foti, G., C. Gommenginger, P. Jales, M. Unwin, A. Shaw, C. Robertson, and J. Rosello, 2015: Spaceborne GNSS reflectometry for ocean winds: First results from the UK TechDemoSat-1 mission. *Geophys. Res. Lett*., **42**, 5435-5441.
Frank, W. M., 1977a: STRUCTURE AND ENERGETICS OF TROPICAL CYCLONE .1. STORM STRUCTURE. *Mon. Wea. Rev*., **105**, 1119-1135.
——, 1977b: STRUCTURE AND ENERGETICS OF TROPICAL CYCLONE .2. DYNAMICS AND ENERGETICS. *Mon. Wea. Rev*., **105**, 1136-1150.
Gaiser, P. W., and Coauthors, 2004: The WindSat spaceborne polarimetric microwave radiometer: Sensor description and early orbit performance. *IEEE Trans. Geosci. Remote Sens*., **42**, 2347-2361.
Garrison, J. L., S. J. Katzberg, and M. I. Hill, 1998: Effect of sea roughness on bistatically scattered range coded signals from the Global Positioning System. *Geophys. Res. Lett.*, **25**, 2257-2260.
Garrison, J. L., A. Komjathy, V. U. Zavorotny, and S. J. Katzberg, 2002: Wind speed measurement using forward scattered GPS signals. *IEEE Trans. Geosci. Remote Sens*., **40**, 50-65.
Gasiewski, A. J., and D. B. Kunkee, 1993: CALIBRATION AND APPLICATIONS OF POLARIZATION-CORRELATING RADIOMETERS. *IEEE Transactions on Microwave Theory and Techniques*, **41**, 767-773.
Germain, O., G. Ruffini, F. Soulat, M. Caparrini, B. Chapron, and P. Silvestrin, 2004: The Eddy Experiment: GNSS-R speculometry for directional sea-roughness retrieval from low altitude aircraft. *Geophys. Res. Lett.*, **31**.
Graf, J. E., W. Y. Tsai, L. Jones, 1998: Overview of QuikSCAT mission - a quick deployment of a high resolution, wide swath scanning scatterometer for ocean wind measurement. IEEE SOUTHEASTCON 98 - Engineering for a New Era, Orlando, Fl, 314-317.
Gray, W. M., 1979: TROPICAL CYCLONE INTENSITY DETERMINATION THROUGH UPPER-TROPOSPHERIC AIRCRAFT RECONNAISSANCE. Bull. Amer. Meteor. Soc., **60**, 1069-1074.
——, 1991: GRADIENT BALANCE IN TROPICAL CYCLONES - COMMENTS. *J. Atmos. Sci.*, 48, 1201-1208.
——, 1998: The formation of tropical cyclones. *Meteorology and Atmospheric Physics*, **67**, 37-69.
Gray, W. M., and D. J. Shea, 1973: HURRICANES INNER CORE REGION .2. THERMAL-STABILITY AND DYNAMIC CHARACTERISTICS. *J. Atmos. Sci.*, **30**, 1565-1576.
Guan, B., N. P. Molotch, D. E. Waliser, E. J. Fetzer, and P. J. Neiman, 2010:

Extreme snowfall events linked to atmospheric rivers and surface air temperature via satellite measurements. *Geophys. Res. Lett.*, **37**.
Harper, B. A., J. D. Kepert, and J. D. Ginger, 2010: Guidelines for converting between various wind averaging periods in tropical cyclone conditions. World Meteorological Organization, TCP Sub-Project Rep., WMO/TD-1555, 54 pp.
Hennon, C. C., D. Long, and F. Wentz, 2006: Validation of QuikSCAT wind retrievals in tropical cyclone environments. Preprints, *14th Conf. on Satellite Meteorology and Oceanography*, Atlanta, GA, Amer. Meteor. Soc., JP1.1. [Available online at http://ams.confex.com/ams/pdfpapers/99478.pdf.]
Hill, K. A., and G. M. Lackmann, 2009: Influence of Environmental Humidity on Tropical Cyclone Size. *Mon. Wea. Rev*., **137**, 3294-3315.
Holland, G. J., 1980: An analytic model of the wind and pressure profiles in hurricanes. *Mon. Wea. Rev*., **108**, 1212–1218.
Hollinger, J., J. L. Peirce, and G. Poe, "SSM/I instrument description," *IEEE Trans. Geosci. Remote Sens.*, vol. 28, no. 5, pp. 781–790, Sep. 1990.
Holmlund, K., C. Velden, and M. Rohn, 2001: Enhanced automated quality control applied to high-density satellite-derived winds. *Mon. Wea. Rev*., **129**, 517–529.
Holton, J. R., 2004: An Introduction to Dynamic Meteorology. Elsevier Academic Press.
Hou, A. H., R. K. Kakar, S. Neeck, A. A. Azarbarzin, C. D. Kummerow, M. Kojima, R. Oki, K. Nakamura, and T. Iguchi, 2014: The Global Precipitation Measurement Mission. *Bull. Amer. Meteor. Soc.*, **95**, 701–722.
Imaoka, K., and Coauthors, 2010: Global Change Observation Mission (GCOM) for Monitoring Carbon, Water Cycles, and Climate Change. Proceedings of the IEEE, 98, 717-734.
Irish, J. L., D. T. Resio, and J. J. Ratcliffe, 2008: The influence of storm size on hurricane surge. *J. Phys. Oceanogr*., **38**, 2003–2013.
Jelesnianski, C. P. 1966: Numerical computations of storm surges without bottom stress, *Mon. Weather Rev.*, **94**, 379–394,
Jones, W. L., P. G. Black, V. E. Delnore, and C. T. Swift, 1981: AIRBORNE MICROWAVE REMOTE-SENSING MEASUREMENTS OF HURRICANE ALLEN. Science, 214, 274-280.
Kantha, L., 2006: Time to replace the Saffir-Simpson Hurricane Scale? *Eos. Trans. Amer. Geophys. Union*, **87**, 3–6.
Kaplan, J., and M. DeMaria, 2003: Large-scale characteristics of rapidly intensifying tropical cyclones in the North Atlantic basin. *Weather and Forecasting*, **18**, 1093-1108.
Katsaros, K. B., P. W. Vachon, W. T. Liu, and P. G. Black, 2002: Microwave remote sensing of tropical cyclones from space. *Journal of Oceanography*, **58**, 137-151.
Katzberg, S. J., O. Torres, and G. Ganoe, 2006: Calibration of reflected GPS for tropical storm wind speed retrievals. *Geophys. Res. Lett.*, **33**.
Katzberg, S. J., J. Dunion, and G. G. Ganoe, 2013: The use of reflected GPS signals to retrieve ocean surface wind speeds in tropical cyclones. *Radio Science*, **48**, 371-387.

Katzberg, S. J., R. A. Walker, J. H. Roles, T. Lynch, and P. G. Black, 2001: First GPS signals reflected from the interior of a tropical storm: Preliminary results from Hurricane Michael. *Geophys. Res. Lett.*, **28**, 1981-1984.

Kawanishi, T., and Coauthors, 2003: The Advanced Microwave Scanning Radiometer for the Earth Observing System (AMSR-E), NASDA's contribution to the EOS for global energy and water cycle studies. *IEEE Trans. Geosci. Remote Sens*., **41**, 184-194.

Kidd, C., V. Levizzani, and S. Laviola, 2010: Quantitative Precipitation Estimation From Earth Observation Satellites. Rainfall: State of the Science, 191, 127-158.

Kidder, S. Q., and Coauthors, 2000: Satellite analysis of tropical cyclones using the Advanced Microwave Sounding Unit (AMSU). *Bull. Amer. Meteor. Soc.*, **81**, 1241-1259.

Kieper, M.E., C.W. Landsea, J.L. Beven, 2016: *A Reanalysis of Hurricane Camille. Bull. Amer. Meteor. Soc*. doi: 10.1175/BAMS-D-14-00137.1

Kimball, S. K., 2006: A modeling study of hurricane landfall in a dry environment. *Mon. Wea. Rev*., **134**, 1901-1918.

Klotz, B. W., and E. W. Uhlhorn, 2014: Improved Stepped Frequency Microwave Radiometer Tropical Cyclone Surface Winds in Heavy Precipitation. *J. Atmos. Oceanic Technol.*, **31**, 2392-2408.

Knabb, R. D., J. R Rhome, D.P.. Brown: 2005, Tropical Cyclone Report: Hurricane Katrina. 43 pp, http://www.nhc.noaa.gov/data/tcr/AL122005_Katrina.pdf

Knaff, J. A., M. DeMaria, D. A. Molenar, C. R. Sampson, and M. G. Seybold, 2011: An automated, objective, multisatellite platform tropical cyclone surface wind analysis. *J. Appl. Meteor. Climatol.*, **50**, 2149–2166, doi:10.1175/2011JAMC2673.1.

Knaff, J. A., M. DeMaria, D. A. Molenar, C. R. Sampson, and M. G. Seybold, 2011: An automated, objective, multisatellite platform tropical cyclone surface wind analysis. *J. Appl. Meteor. Climatol.*, **50**, 2149–2166, doi:10.1175/2011JAMC2673.1.

Knaff, J.A., S.P. Longmore, R.T. DeMaria, and D.A. Molenar, 2015: Improved Tropical-Cyclone Flight-Level Wind Estimates Using Routine Infrared Satellite Reconnaissance. *J. Appl. Meteor. Climatol.*, **54**, 463-478.

Knaff, J.A., C. J. Slocum, K. D. Musgrave, C. R. Sampson, and B. R. Strahl, 2016: Using routinely available information to estimate tropical cyclone wind structure. *Mon. Wea. Rev.*, **144**, 1233–1247, doi:10.1175/MWR-D-15-0267.1.

Komjathy, A., M. Armatys, D. Masters, P. Axelrad, V. Zavorotny, and S. Katzberg, 2004: Retrieval of ocean surface wind speed and wind direction using reflected GPS signals. *J. Atmos. Oceanic Technol.*, **21**, 515-526.

Kossin, J.P., J.A. Knaff, H.I. Berger, D.C. Herndon, T.A. Cram, C.S. Velden, R.J. Murnane, and J.D. Hawkins, 2007: Estimating hurricane wind structure in the absence of aircraft reconnaissance. *Wea. Forecasting*, **22**, 89–101.

Kozar M.E., and V.Misra, 2014: Statistical Prediction of Integrated Kinetic Energy in North Atlantic Tropical Cyclones. *Mon. Wea. Rev*., **142**, 4646–4657. doi: 10.1175/MWR-D-14-00117.1.

Kozar, M.E., 2015: Analysis and Prediction of Integrated Kinetic Energy in Atlantic Tropical Cyclones. Ph.D. Dissertation, Florida State University, 197 pp. http://purl.flvc.org/fsu/fd/FSU_migr_etd-9376.

Kozar, M. E., V. Misra, and M. D. Powell, 2016: Hindcasts of Integrated Kinetic Energy in Atlantic Tropical Cyclones: A Neural Network Prediction Scheme. *Mon. Wea. Rev*., **144**, 4591-4603.

Kummerow, C., W. S. Olson, and L. Giglio, 1996: A simplified scheme for obtaining precipitation and vertical hydrometeor profiles from passive microwave sensors. *IEEE Trans. Geosci. Remote Sens*., **34**, 1213-1232.

Kummerow, C., W. Barnes, T. Kozu, J. Shiue, and J. Simpson, 1998: The Tropical Rainfall Measuring Mission (TRMM) sensor package, *J. Atmos. Ocean. Technol*., vol. 15, no.3, pp. 809-817.

Kummerow, C., and Coauthors, 2001: The evolution of the Goddard profiling algorithm (GPROF) for rainfall estimation from passive microwave sensors. *J. Appl. Meteor*., **40**, 1801-1820.

Landsea, C. W., and J. L. Franklin, 2013: Atlantic Hurricane Database Uncertainty and Presentation of a New Database Format. *J. Appl. Meteor.*, **141**, 3576-3592.

Leung, T., J. Kong, E. Njoku, D. Staelin, and J. Waters, 1977: Theory for microwave thermal emission from a layer of cloud or rain. *IEEE Transactions on Antennas and Propagation*, **25**, 650-657.

Lin, N., and D. Chavas, 2012: On hurricane parametric wind and applications in storm surge modeling. *J. Geophys. Res*., **117**, D09120, doi:10.1029/2011JD017126.

Luo, Z., G. L. Stephens, K. A. Emanuel, D. G. Vane, N. D. Tourville, and J. M. Haynes, 2008: On the use of CloudSat and MODIS data for estimating hurricane intensity. *IEEE Geoscience and Remote Sensing Letters*, **5**, 13-16.

Maclay K.S., M. DeMaria, and T.H. Vonder Haar, 2008: Tropical Cyclone Inner-Core Kinetic Energy Evolution. *Mon. Wea. Rev*., **136**, 4882-4898.

Madsen, N. M., and D. G. Long, 2016: Calibration and Validation of the RapidScat Scatterometer Using Tropical Rainforests. *IEEE Trans. Geosci. Remote Sens*., **54**, 2846-2854.

Mahendran, M., 1998: Cyclone intensity categories. *Wea. Forecasting*, **13**, 878–883.

Marshak, A., A. Davis, W. Wiscombe, and G. Titov, 1995: The verisimilitude of the independent pixel approximation used in cloud remote sensing," *Remote Sens. Environ.*, **52**, 71–78.

Meissner, T., and F. J. Wentz, 2009: Wind-Vector Retrievals Under Rain With Passive Satellite Microwave Radiometers. *IEEE Trans. Geosci. Remote Sens*., **47**, 3065-3083.

——, 2012: The emissivity of the ocean surface between 6 - 90 GHz over a large range of wind speeds and Earth incidence angles, *IEEE Trans. Geosci. Remote Sens*., **50**, 3004-3026.

Misra V., S. DiNapoli, and M. Powell, 2013: The Track Integrated Kinetic Energy of Atlantic Tropical Cyclones. *Mon. Wea. Rev*., **141**, 2383-2389.

Morena, L. C., K. V. James, and J. Beck, 2004: An introduction to the

RADARSAT-2 mission. *Canadian Journal of Remote Sensing*, **30**, 221-234.
Morris, M., and C. S. Ruf, 2015a: A Coupled-Pixel Model (CPM) Atmospheric Retrieval Algorithm for High-Resolution Imagers. *J. Atmos. Oceanic Technol.*, **32**, 1866-1879.
——, 2015b: Examination of a Coupled-Pixel Model (CPM) atmospheric retrieval algorithm. 2015 IEEE International Geoscience and Remote Sensing Symposium (IGARSS), 925-928.
Morris, M., D. D. Chen, and C. S. Ruf, 2016: Earth antenna temperature variability for CYGNSS. 2016 IEEE International Geoscience and Remote Sensing Symposium (IGARSS), 846-849.
Morris, M., and C. S. Ruf, 2016a: Estimating Tropical Cyclone Integrated Kinetic Energy with the CYGNSS Satellite Constellation. Journal of Applied Meteorology and Climatology, doi: 10.1175/JAMC-D-16-0176.1, in press.
——, 2016b: Determining Tropical Cyclone Surface Wind Speed Structure and Intensity with the CYGNSS Satellite Constellation, *J. Appl. Meteor. Climatol.*, in review.
Mueller, K. J., M. DeMaria, J. A. Knaff, J. P. Kossin, and T. H. Vonder Haar, 2006: Objective estimation of tropical cyclone wind structure from infrared satellite data. *Wea. Forecasting*, **21**, 990–1005, doi:10.1175/WAF955.1.
Njoku, E. G., J. M. Stacey, and F. T. Barath, 1980: The Seasat scanning multichannel microwave radiometer (SMMR): Instrument description and performance," *IEEE J. Ocean. Engin.*, **5**, 100-115.
NOAA/NESDIS/STAR/RAMMB, 2016: Real-Time Tropical Cyclone Products – Description of Products. Accessed 09 May. [Available online at http://rammb.cira.colostate.edu/products/tc_realtime/about.asp].
Nolan, D. S., J. A. Zhang, and E. W. Uhlhorn, 2014: On the Limits of Estimating the Maximum Wind Speeds in Hurricanes. *Mon. Wea. Rev.*, **142**, 2814-2837.
Nordberg, W., J. Conaway, D. B. Ross, and T. Wilheit, 1971: Measurements of Microwave Emission from a Foam-Covered, Wind-Driven Sea. *J. Atmos. Sci.*, **28**, 429-435.
O'Brien, A., 2014: CYGNSS End-to-End Simulator, CYGNSS Project Document 148-0123. [Available online at http://clasp-research.engin.umich.edu/missions/cygnss/reference/148-0123_CYGNSS_E2ES_EM.pdf].
Olander, T. L., and C. S. Velden, 2007: The advanced Dvorak technique: Continued development of an objective scheme to estimate tropical cyclone intensity using geostationary infrared satellite imagery. *Wea. Forecasting*, **22**, 287-298.
Pasch, R. J., T. B. Kimberlain: 2011: Tropical Cyclone Report: Hurricane Igor, 20 pp, http://www.nhc.noaa.gov/data/tcr/AL112010_Igor.pdf
Piñeros, M. F., E. A. Ritchie, and J. S. Tyo, 2008: Objective measures of tropical cyclone structure and intensity change from remotely sensed infrared image data. *IEEE Trans. Geosci. Remote Sens.*, 46, 3574–3580.
Piñeros, M. F., E. A. Ritchie, and J. S. Tyo, 2011: Estimating tropical cyclone intensity from infrared image data. *Wea. Forecasting*, **26**, 690–698.
Powell, M. D., and T. A. Reinhold, 2007: Tropical cyclone destructive potential by

integrated kinetic energy. *Bull. Amer. Meteor. Soc*., **88**, 513–526.
Powell, M. D., and Coauthors, 2010: Reconstruction of Hurricane Katrina's wind fields for storm surge and wave hindcasting. *Ocean Engineering*, **37**, 26-36.
Powell, M. D., S. H. Houston, L. R. Amat, and N Morisseau-Leroy, 1998: The HRD real-time hurricane wind analysis system. *J. Wind Engineer*. and *Indust. Aerodyn.* **77&78**, 53-64.
Prabhakara, C., G. Dalu, G. L. Liberti, J. J. Nucciarone, and R. Suhasini, 1992: Rainfall Estimation over Oceans from SMMR and SSM/I Microwave Data. *J. Appl. Meteor.*, **31**, 532-552.
Rappaport, E. N., 2014: Fatalities in the United States from Atlantic Tropical Cyclones. *Bull. Amer. Meteor. Soc*., **95**, 341-346.
Rappaport, E. N., and Coauthors, 2009: Advances and Challenges at the National Hurricane Center. *Wea. and Forecasting*, **24**, 395-419.
Rogers, R.R., M. K. Yau, 1989: A Short Course in Cloud Physics. 3rd ed. Butterworth-Heinemann.
Rodriguez-Alvarez, N., D. M. Akos, V. U. Zavorotny, J. A. Smith, A. Camps, and C. W. Fairall, 2013: Airborne GNSS-R Wind Retrievals Using Delay-Doppler Maps. *IEEE Trans. Geosci. Remote Sens*., **51**, 626-641.
Rogers, R., and Coauthors, 2006: The intensity forecasting experiment. *Bull. Amer. Meteor. Soc.*, **87**, 1523-+.
Rosenkranz, P. W., and D. H. Staelin, 1972: Microwave emissivity of ocean foam and its effect on nadiral radiometric measurements. *J. Geophys. Res.*, **77**, 6528-6538.
Rotunno, R., and K. A. Emanuel, 1987: AN AIR-SEA INTERACTION THEORY FOR TROPICAL CYCLONES .2. EVOLUTIONARY STUDY USING A NONHYDROSTATIC AXISYMMETRICAL NUMERICAL-MODEL. *J. Atmos. Sci.*, **44**, 542-561.
Ruf, C., P. Chang, M.P. Clarizia, S. Gleason, Z. Jelenak, J. Murray, M. Morris, S. Musko, D. Posselt, D. Provost, D. Starkenburg, V. Zavorotny, 2016: CYGNSS Handbook. Michigan Pub., 154 pp.
Ruf, C. S., and Coauthors, 2016: New Ocean Winds Satellite Mission to Probe Hurricanes and Tropical Convection. *Bull. Amer. Meteor. Soc.*, **97**.
Saffir, H., 1975: Low cost construction resistant to earthquakes and hurricanes. ST/ESA/23, United Nations, 216 pp.
Schroeder, L. C., W. L. Grantham, J. Mitchell, and J. Sweet, 1982: SASS measurements of the Ku-band radar signature of the ocean. *IEEE Journal of Oceanic Engineering*, **7**, 3–14.
Schroeder, L. C., W. L. Grantham, E. M. Bracalente, C. L. Britt, K. S. Shanmugam, F. J. Wentz, B. B. Hinton, 1985: Removal of Ambiguous Wind Directions for a Ku-Band Wind Scatterometer Using Three Different Azimuth Angles. *IEEE Trans. Geosci. Remote Sens*., **23**, 91–100.
Shea, D. J., and W. M. Gray, 1973: HURRICANES INNER CORE REGION .1. SYMMETRIC AND ASYMMETRIC STRUCTURE. J. Atmos. Sci., **30**, 1544-1564.
Simpson, R. H., 1974: The hurricane disaster potential scale. *Weatherwise*, **27**, 169–186.

Shu, S. J., and L. G. Wu, 2009: Analysis of the influence of Saharan air layer on tropical cyclone intensity using AIRS/Aqua data. Geophys. Res. Lett., **36**, 5.
Sitkowski, M., J. P. Kossin, and C. M. Rozoff, 2011: Intensity and Structure Changes during Hurricane Eyewall Replacement Cycles. *Mon. Wea. Rev.*, **139**, 3829-3847.
Spencer, R. W., H. M. Goodman, and R. E. Hood, 1989: Precipitation Retrieval over Land and Ocean with the SSM/I: Identification and Characteristics of the Scattering Signal. *J. Atmos. Oceanic Technol*., **6**, 254-273.
Staelin, D. H., and F. W. Chen, 2000: Precipitation observations near 54 and 183 GHz using the NOAA-15 satellite. *IEEE Trans. Geosci. Remote Sens*., **38**, 2322-2332.
Stephens, G. L., and C. D. Kummerow, 2007: The Remote Sensing of Clouds and Precipitation from Space: A Review. *J. Atmos. Sci.*, **64**, 3742-3765.
Stogryn, A., 1967: The apparent temperature of the sea at microwave frequencies. *IEEE Transactions on Antennas and Propagation*, **15**, 278-286.
Stull, R., 2015: "Practical Meteorology: An Algebra-based Survey of Atmospheric Science." Univ. of British Columbia. 938 pages. ISBN 978-0-88865-176-1
Surussavadee, C., and D. H. Staelin, 2008: Global millimeter-wave precipitation retrievals trained with a cloud-resolving numerical weather prediction model, Part II: Performance valuation. *IEEE Trans. Geosci. Remote Sens*., 46, 109-118.
Tallapragada, V. and Coauthors, 2013: Hurricane Weather Research and Forecasting (HWRF) Model: 2013, pp 99, http://www.dtcenter.org/HurrWRF/users/docs/users_guide/HWRF_v3.5a_Users_Guide.pdf
Thompson, D. R., T. M. Elfouhaily, and J. L. Garrison, 2005: An improved geometrical optics model for bistatic GPS scattering from the ocean surface. *IEEE Trans. Geosci. Remote Sens*., **43**, 2810-2821.
Torn, R. D., and C. Snyder, 2012: Uncertainty of Tropical Cyclone Best-Track Information. *Wea. Forecasting*, **27**, 715-729.
Tourville, N., G. Stephens, M. DeMaria, and D. Vane, 2015: Remote Sensing of Tropical Cyclones: Observations from CloudSat and A-Train Profilers. *Bull. Amer. Meteor. Soc.*, **96**, 609-622.
Uhlhorn, E. W., and P. G. Black, 2003: Verification of Remotely Sensed Sea Surface Winds in Hurricanes. *J. Atmos. Oceanic Technol.*, **20**, 99-116.
Uhlhorn, E. W., P. G. Black, J. L. Franklin, M. Goodberlet, J. Carswell, and A. S. Goldstein, 2007: Hurricane Surface Wind Measurements from an Operational Stepped Frequency Microwave Radiometer. *Mon. Wea. Rev.*, **135**, 3070-3085.
Ulaby, F. T., D. G. Long, W. J. Blackwell, C. Elachi, and K. Sarabandi, 2014: Microwave Radar and Radiometric Remote Sensing. University of Michigan Press.
Varnai, T., R. Davies, 1999: Effects of cloud heterogeneities on shortwave radiation: comparison of cloud-top variability and internal heterogeneity, *J. Atmos. Sci.*, **56**, 4206–4224.
Vaze, P., and Coauthors, 2010: THE JASON-3 MISSION: COMPLETING THE

TRANSITION OF OCEAN ALTIMETRY FROM RESEARCH TO OPERATIONS. Conference on Sensors, Systems, and Next-Generation Satellites XIV, Toulouse, FRANCE.
Velden, C. S. and Coauthors, 2005: Recent innovations in deriving tropospheric winds from meteorological satellites. *Bull. Amer. Meteor. Soc*., **86**, 205–223.
Velden, C., and Coauthors, 2006: The Dvorak tropical cyclone intensity estimation technique. *Bull. Amer. Meteor. Soc*., **87**, 1195-1210.
Velden, C. S., C. M. Hayden, S. J. Nieman, W. P. Menzel, S. Wanzong, and J. S. Goerss, 1997: Upper-tropospheric winds derived from geostationary satellite water vapor observations. *Bull. Amer. Meteor. Soc*., **78**, 173–195.
Velden, C. S., T. L. Olander, and R. M. Zehr, 1998: Development of an objective scheme to estimate tropical cyclone intensity from digital geostationary satellite infrared imagery. *Wea. Forecasting*, **13**, 172-186.
Weinman, J. A., and P. J. Guetter, 1977: Determination of Rainfall Distributions from Microwave Radiation Measured by the Nimbus 6 ESMR. *J. Appl. Meteor.*, **16**, 437-442.
Weng, F. Z., B. H. Yan, and N. C. Grody, 2001: A microwave land emissivity model. *Journal of Geophysical Research-Atmospheres*, **106**, 20115-20123.
Wentz, F. J., 1975: A two-scale scattering model for foam-free sea microwave brightness temperatures, *J. Geophys. Res.*, **80**(24), 3441–3446.
Werninghaus, R., and S. Buckreuss, 2010: The TerraSAR-X Mission and System Design. *IEEE Trans. Geosci. Remote Sens*., **48**, 606-614.
Wilheit, T., and Coauthors, 1994: Algorithms for the retrieval of rainfall from passive microwave measurements. *Remote Sensing Reviews*, **11**, 163-194.
Wilheit, T. T., 1986: Some Comments on Passive Microwave Measurement of Rain. *Bull. Amer. Meteor. Soc.*, **67**, 1226-1232.
Wilheit, T. T., J. S. Theon, W. E. Shenk, L. J. Allison, and E. B. Rodgers, 1976: Meteorological Interpretations of the Images from the Nimbus 5 Electrically Scanned Microwave Radiometer. *J. Appl. Meteor.*, **15**, 166-172.
Wilheit, T. “The electrically scanning microwave radiometer (ESMR) experiment,” in The Nimbus-5 User’s Guide, NASA/Goddard Space Flight Center, Greenbelt, MD, pp. 59-105, 1971.
——. “The electrically scanning microwave radiometer (ESMR) experiment,” in The Nimbus-6 User’s Guide, NASA/Goddard Space Flight Center, Greenbelt, MD, pp. 87-108, 1975.
Williams, G. F., 1969: Microwave radiometry of the ocean and the possibility of marine wind velocity determination from satellite observations. *J. Geophys. Res.*, **74**, 4591-4594.
Willoughby, H. E., 1988: The dynamics of the tropical cyclone core. *Aust. Meteor. Mag.*, **36**, 183–191.
——, 1990: GRADIENT BALANCE IN TROPICAL CYCLONES. *J. Atmos. Sci*., **47**, 265-274.
——, 1991: GRADIENT BALANCE IN TROPICAL CYCLONES - REPLY. *J. Atmos. Sci.*, **48**, 1209-1212.
Willoughby, H. E., J. A. Clos, and M. G. Shoreibah, 1982: Concentric Eye Walls, Secondary Wind Maxima, and The Evolution of the Hurricane vortex. *J.*

Atmos. Sci., **39**, 395-411.
Willoughby, H. E., R. W. R. Darling, and M. E. Rahn, 2006: Parametric representation of the primary hurricane vortex. Part II: A new family of sectionally continuous profiles. *Mon. Wea. Rev.*, **134**, 1102–1120.
Wu, L., H. Su, R. G. Fovell, T. J. Dunkerton, Z. Wang, and B. H. Kahn, 2015: Impact of environmental moisture on tropical cyclone intensification. Atmospheric Chemistry and Physics, **15**, 14041-14053.
Wu, L., and Coauthors, 2012: Relationship of environmental relative humidity with North Atlantic tropical cyclone intensity and intensification rate. *Geophys. Res. Lett.*, **39**.
Yueh, S. H. and J. Chaubell, 2012: Sea Surface Salinity and Wind Retrieval Using Combined Passive and Active L-Band Microwave Observations. *IEEE Trans. Geosci. Remote Sens.*, **50**, 1022–1032.
Yueh, S. H., A. G. Fore, W. Tang, A. Hayashi, B. Stiles, N. Reul, Y. Weng, F. Zhang, 2016: SMAP L-Band Passive Microwave Observations of Ocean Surface Wind During Severe Storms. *IEEE Trans. Geosci. Remote Sens.*, **54**, 7339-7350.
Zuidema, P., and K. F. Evans, 1998: On the validity of the independent pixel approximation for the boundary layer clouds observed during ASTEX, *J. Geophys. Res.*, **103**, 6059–6074.